



VNIVERSITAT
DE VALÈNCIA

1

2 **Search for associated production of a Higgs**
3 **boson and a single top quark in $2\ell + \tau_{had}$**
4 **final state using proton-proton collisions**
5 **at $\sqrt{s} = 13$ TeV with the ATLAS detector**

6

PhD Thesis

7

Pablo Martínez Agulló

8

Instituto de Física Corpuscular (IFIC)
Departament de Física Atòmica, Molecular i Nuclear
Programa de Doctorat en Física

9

10

Under the supervision of

11

Carlos Escobar Ibáñez
and
Susana Cabrera Urbán

12

13

14

15

València, 22nd April 2022

¹⁶ **Carlos Escobar Ibáñez,**
¹⁷ investigador científico del Consejo Superior de Investigaciones Científicas, y
¹⁸

¹⁹ **Susana Cabrera Urbán,**
²⁰ científica titular del Consejo Superior de Investigaciones Científicas,

²¹ **Certifican:**

²² Que la presente memoria, **Search for associated production of a**
Higgs boson and a single top quark in $2l + \tau_{had}$ final state
using proton-proton collisions at $\sqrt{s} = 13$ TeV with the ATLAS
detector, ha sido realizada bajo su dirección en el Instituto de Física
Corpuscular, centro mixto de la Universitat de València y del CSIC, por
Pablo Martínez Agulló, y constituye su Tesis para optar al grado de
Doctor en Física.

²⁹ Y para que así conste, en cumplimiento de la legislación vigente, presenta
en el Departamento de Física Atómica, Molecular y Nuclear de la Universidad
de Valencia la referida Tesis Doctoral, y firman el presente certificado.

³²

³³ València, a DD de MES de 2022,

³⁴

³⁵ Carlos Escobar Ibáñez

Susana Cabrera Urbán

36

37

38

39

C'est quoi ce bordel ???

—DANIEL BOSSON,

⁴⁰ Preface

⁴¹ The Standard Model of particle physics is both incredibly successful and
⁴² glaringly incomplete. Among the questions left open is the striking imbalance
⁴³ of matter and antimatter in our universe, which inspires experiments to
⁴⁴ compare the fundamental properties of matter/antimatter conjugates with
⁴⁵ high precision.

⁴⁶ The discovery of a Higgs boson by the ATLAS and CMS experiments in
⁴⁷ 2012 opened a new field for exploration in the realm of particle physics.

- ⁴⁸ - ttbar sensitive to the y_t module
- ⁴⁹ - thq sesntive to the sign

⁵⁰ Poner algo bonito del top y el Higgs

⁵¹ The top quark is the heaviest elementary particle discovered so far, with
⁵² a mass of $m_{top} = 172.76 \pm 0.30$ GeV [1], followed by the Higgs boson, with
⁵³ $m_H = 125.25 \pm 0.17$ GeV [2].

⁵⁴ This thesis describes the search for the associated production of a Higgs
⁵⁵ boson and a single top quark (tHq) in the final state with three leptons,
⁵⁶ being two of them light leptons (e/μ) and the other one a hadronically-
⁵⁷ decaying tau quark (τ_{had}). The examined channel is referred as $2\ell + 1\tau_{had}$
⁵⁸ and is further divided in two sub-channels attending to the relative electric
⁵⁹ charge between the light leptons ($2\ell SS + 1\tau_{had}$ and $2\ell OS + 1\tau_{had}$). The
⁶⁰ research carried targets SM Higgs bosons decaying to $H \rightarrow \tau\tau$, $H \rightarrow WW$
⁶¹ and $H \rightarrow ZZ$.

⁶² This analysis uses an integrated luminosity of 139 fb^{-1} of proton-proton
⁶³ collision data at centre-of-mass energy of 13 TeV collected by ATLAS during
⁶⁴ LHC Run 2. The ATLAS detector is one of the four detectors at the Large
⁶⁵ Hadron Collider (LHC) of the European Organization for Nuclear Research
⁶⁶ (CERN).

⁶⁷ This analysis presents a great challenge due to the difficulty of distinguishing
⁶⁸ the tHq production in the $2\ell + 1\tau_{had}$ channels from other SM processes
⁶⁹ with much higher cross-sections. The tHq process has an extremely small

70 cross-section (70 fb at 13 TeV) and the $2\ell + 1\tau_{\text{had}}$ channel accounts only for
71 the 3.5% of the total production.

72 In order to help separating the signal events for the background pro-
73 cesses that mimic the $2\ell + 1\tau_{\text{had}}$ signature a reconstruction of the events is
74 approached by determining the information about the top quark first and
75 the Higgs boson secondly. This is a complex task due the presence of, at
76 least, four neutrinos in the final state that difficult determining the linear
77 momentum of both the top quark and Higgs boson.

78 Additional studies are carried to assign origin the light-flavoured leptons,
79 i.e. whether these came form the Higgs boson or the top quark. To do so,
80 a gradient boosted decision tree is used.

81 Moreover, due to the arduousness of separating the the tHq from the
82 backgrounds, multivariate techniques are used. With them are defined
83 signal-enriched regions and control regions to constrain the most important
84 background processes, which are those related to top-quark-antiquark-pair
85 production ($t\bar{t}$, $t\bar{t}H$, $t\bar{t}W$ and $t\bar{t}Z$) and Z boson plus jets.

86 The possible observation of a an excess of signal events with respect to
87 the Standard Model predictions, would be a clear evidence of new physics
88 in terms of \mathcal{CP} -violating Yukawa couplings between the top quark and the
89 Higgs boson.

90 Furthermore, other channels (defined by their final state) are being stud-
91 ied in the context of tHq research

92 During this thesis the “god-given” units are used. In this system (name
93 natural system) the Planck constant and the speed of light have the same
94 magnitude and dimensions ($\hbar = c = 1$), implying that:

$$95 \quad [\text{length}] = [\text{time}] = [\text{energy}]^{-1} = [\text{mass}]^{-1}.$$

96 In the international system (SI) units, the values are $\hbar = 1.055 \times 10^{-34}$ Js
97 and $c = 2.998 \times 10^8$ m/s. An exception is made for the Chapter 2, where
98 the SI is used for describing the design of the LHC and ATLAS.

99 **Conceptos triviales que también debería introducir en**
100 **algún momento [http://opendata.atlas.cern/books/current/
101 get-started/_book/GLOSSARY.html](http://opendata.atlas.cern/books/current/get-started/_book/GLOSSARY.html)**

¹⁰² **Acknowledgements**

¹⁰³ This work would not have been possible without the invaluable help of a
¹⁰⁴ large number of people, whom I have been fortunate to meet, and to whom
¹⁰⁵ I would like to thank and dedicate this thesis.

¹⁰⁶ Gracias gracias

¹⁰⁷ Contents

¹⁰⁸	Preface	v
¹⁰⁹	Acknowledgements	vii
¹¹⁰	1 Theoretical Framework	1
¹¹¹	1.1 The Standard Model of particle physics	1
¹¹²	1.1.1 Introduction to the SM and its elementary particles	2
¹¹³	1.1.2 Quantum electrodynamics	6
¹¹⁴	1.1.3 Electroweak interactions	8
¹¹⁵	1.1.4 Quantum chromodynamics	15
¹¹⁶	1.1.5 Particle masses	19
¹¹⁷	1.1.6 Charge-Parity	26
¹¹⁸	1.1.7 Wrap up	26
¹¹⁹	1.2 Top quark	32
¹²⁰	1.2.1 Top quark discovery	34
¹²¹	1.2.2 Top quark production at LHC	35
¹²²	1.2.3 Top quark decay	40
¹²³	1.2.4 Top quark polarisation	44
¹²⁴	1.2.5 Top quark physics	44
¹²⁵	1.3 Higgs boson	45
¹²⁶	1.3.1 Higgs boson discovery	45
¹²⁷	1.3.2 Higgs boson production at LHC	46

128	1.3.3	Higgs boson decay	47
129	1.3.4	Higgs boson physics	49
130	1.4	Top quark and Higgs boson interplay	49
131	1.4.1	$t\bar{t}H$	50
132	1.4.2	tHq	51
133	2	The ATLAS experiment at the Large Hadron Collider of CERN laboratory	55
134	2.1	CERN	55
135	2.2	Large Hadron Collider	57
136	2.2.1	Machine design	57
137	2.2.2	Accelerator complex	61
138	2.2.3	LHC Experiments	62
139	2.2.4	LHC Computing grid	65
140	2.2.5	Energy, Luminosity and Cross-section	67
141	2.2.6	The Pile-up effect	72
142	2.2.7	Phenomenology of proton-proton collisions	73
143	2.3	ATLAS	77
144	2.3.1	Coordinate system	80
145	2.3.2	Inner Detector	81
146	2.3.3	Calorimeters	86
147	2.3.4	Muon Spectrometer	91
148	2.3.5	Magnet system	93
149	2.3.6	Trigger and Data Acquisition System	96
150	2.3.7	ATLAS upgrade towards HL-LHC	97
151	2.4	Alignment of the inner detector	102
152	2.4.1	Alignment requirements	102
153	2.4.2	Track based alignment	102
154	2.4.3	Alignment results during Run-2	102
155	2.4.4	Alignment towards Run-3	102

157	3 Data and simulated events and object reconstruction	103
158	3.1 Data	103
159	3.2 Monte Carlo	103
160	3.2.1 MC simulations	104
161	3.2.2 MC generators	104
162	3.3 Object reconstruction and identification	104
163	3.3.1 Tracking	105
164	3.3.2 Vertices	106
165	3.3.3 Electrons and photons	106
166	3.3.4 Muons	106
167	3.3.5 Jets	106
168	3.3.6 Missing transverse energy	107
169	3.3.7 Overlap removal	107
170	4 Probing the top-quark polarisation in the single-top t-channel production	109
171		
172	4.1 Introduction	109
173	4.2 Top quark polarisation observables	110
174	4.3 Simulated event samples	110
175	4.4 Object reconstruction	110
176	4.5 Trigger requirements and event preselection	110
177	5 Search for rare associate tHq production	111
178		
179	5.1 Introduction	111
180	5.2 Data and simulated events	112
181	5.3 Object definition and reconstruction	113
182	5.4 Signal	113
183	5.4.1 Signal generation and validation	113
184	5.4.2 Parton-level truth validation	113
	5.4.3 Lepton assignment	113

185	5.4.4 Top quark and Higgs boson reconstruction	117
186	5.5 Background estimation	117
187	5.5.1 Fakes estimation	117
188	5.5.2 Prompt backgrounds	118
189	5.6 Event selection	119
190	5.6.1 Preselection	119
191	5.6.2 BDT	119
192	5.6.3 Signal Region	120
193	5.6.4 Control Regions	120
194	5.7 Systematic uncertainties	121
195	5.7.1 Theoretical uncertainties	123
196	5.7.2 Modelling uncertainties	123
197	5.7.3 Experimental uncertainties	123
198	5.8 Fit results	123
199	5.8.1 Strategy	123
200	5.8.2 Fit with Asimov data	123
201	5.8.3 Fit to data	123
202	5.8.4 Results	123
203	5.8.5 Data fit	123
204	5.9 Combination results	123
205	5.10 Conclusions	124
206	6 Conclusion	125
207	Abbreviations	128
208	Bibliography	131
209	Summary of the results	145
210	Resum de la tesi	147

211	1	Marc teòric	147
212	1.1	El Model Estàndard	147
213	1.2	La física del quark top	147
214	1.3	La física del bosó de Higgs	147
215	2	L'experiment ATLAS del LHC al CERN	147
216	2.1	El gran col·lisionador d'hadrons	147
217	2.2	El detector ATLAS	147
218	3	Mesura de la polarització del quark top al canal- <i>t</i>	147
219	3.1	Selecció d'esdeveniments	148
220	3.2	Estimació del fons	148
221	3.3	Fonts d'incertesa	148
222	3.4	Resultats	148
223	4	Recerca de processos <i>tH</i> amb un estat final $2\ell + 1\tau_{\text{had}}$	148
224	4.1	Selecció d'esdeveniments	148
225	4.2	Estimació del fons	148
226	4.3	Fonts d'incertesa	148
227	4.4	Resultats	148
228	5	Conclusions	148

²²⁹ **Chapter 1**

²³⁰ **Theoretical Framework**

²³¹ **1.1 The Standard Model of particle physics**

²³² Since the very first moment of our history, the humankind has pursued
²³³ the knowledge of nature, has tried to understand and describe how the
²³⁴ universe works at a fundamental level. In fact, the word physics comes
²³⁵ from the Greek “*φυσική*” which means “nature” [3][4]. Most of the enquires
²³⁶ regarding this, can be boiled down to two basic questions: What are the
²³⁷ ultimate building blocks of reality? and which are the rules that govern
²³⁸ them?

²³⁹ In the 7th century BCE, the pre-Socratic philosopher Thales of Miletus
²⁴⁰ already proclaimed that every event had a natural cause [5]. Later, to un-
²⁴¹ derstand how the basic components of the matter were formed, the ancient
²⁴² Indian philosophers such as Kanada and Dignaga on the 6th century BCE
²⁴³ and Greeks Democritus and Leucippus on the 5th century BCE, developed
²⁴⁴ the atomism, which comes from “*ατομον*” meaning uncuttable or indivisible
²⁴⁵ [6][7].

²⁴⁶ From then to our days, the search for the minute fragments that comprise
²⁴⁷ the matter and its interactions has led us to the Standard Model (SM) of
²⁴⁸ particle physics, one of the most successful scientific theories cultivated
²⁴⁹ so far. This understanding of the universe can explain phenomena from
²⁵⁰ behaviour of atoms to how stars burn.

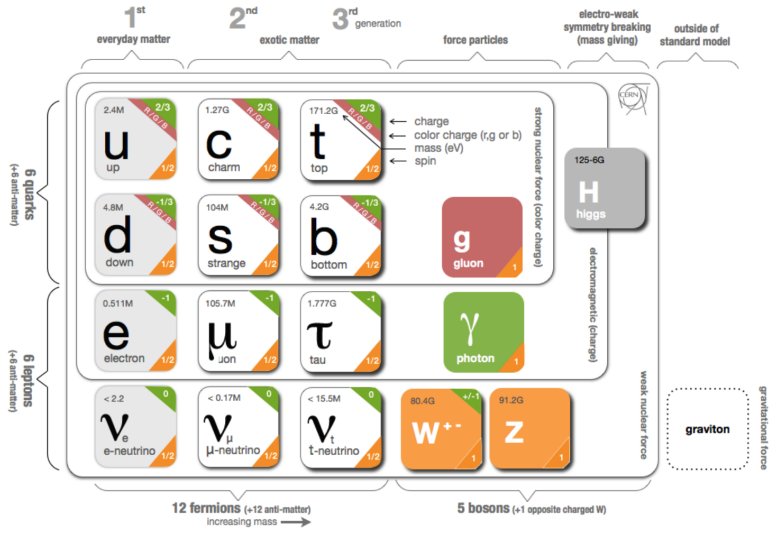


Figure 1.1: Fundamental particles of the Standard Model.

251 1.1.1 Introduction to the SM and its elementary 252 particles

253 Based on Quantum Field Theory (QFT), the SM of particle physics
254 provides the theoretical framework that constitutes what is currently ac-
255 cepted as the best description of particles physics. It aims to explain both
256 all particles of matter and their interactions. The completion of the SM
257 was a collaborative effort of several scientists during the second half of the
258 20th, being the current formulation finalised in the decade of 1970. A rep-
259 resentation of the fundamental particles, i.e. particles that are not made
260 of anything else, that compose the SM is presented in Figure 1.1. Most of
261 these particles are unstable and decay to lighter particles within fractions
262 of a second. As the scheme in Figure 1.1 indicates, the 12 fermions have
263 their corresponding 12 anti-fermions and the quarks and gluons carry colour
264 charge.

265 The SM is a gauge theory based on the symmetry group
266 $SU(3)_C \otimes SU(2)_L \otimes U(1)_Y$, which describes all fundamental interactions
267 except from the gravitational force¹. This theory provides an explana-
268 tion to strong, weak and electromagnetic interactions via the exchange of
269 the corresponding vector² bosons (spin-1 gauge fields). The mediation for
270 the electromagnetic interaction (explicated in 1.1.2) is done by one mass-
271 less photon (γ), this force is invariant under the $U(1)$ symmetry group.

¹The gravitational interaction is described by Einstein’s General Relativity (GR) [8].

²“Vector bosons” refer to all bosons that have spin 1 in contrast to the “scalar boson’s” which have spin 0.

Interaction	Theory	Mediator	Relative strength	Range (m)
Strong	QCD	g	1	10^{-15}
Electromagnetic	QED/EW	γ	$1/137$	∞
Weak	EW	W^\pm, Z	10^{-6}	10^{18}
Gravitational	GR	-	6×10^{-39}	∞

Table 1.1: Typical strength of the fundamental interactions with respect to the strong interaction. Here the strength is understood as the coupling constant. In GR the gravitational interaction is not a force but the effect of the four-dimensional spacetime curvature and, hence, it has no mediator in this formalism.

272 While for the weak interactions, guided by $SU(2)$, three massive bosons,
 273 W^+ , W^- and Z , act as mediators ($m_{W^\pm} = 80.385 \pm 0.015$ GeV and
 274 $m_Z = 91.1876 \pm 0.02$ GeV). Although the electromagnetic and weak in-
 275 teractions seem completely different at low energies, they are two aspects of
 276 the same force and can be described simultaneously by the $SU(2)_L \otimes U(1)_Y$
 277 symmetry group, which represents the so called Electro-Weak (EW) sector
 278 (detailed in Section 1.1.3). The strong force, with its 8 massless gluons
 279 (g), is described by the $SU(3)_C$ colour group (see Section 1.1.4). All these
 280 interactions differ in their magnitude, range and the physical phenomena
 281 that describe. These features are summarised in Table 1.1, where not only
 282 the interactions of the SM are included but the gravitation is as well.

283 Apart from the vector bosons, there is one massive scalar boson, the
 284 Higgs boson ($m_H = 125.25 \pm 0.17$ GeV). Through the interaction with this
 285 particle, all massive particles of Figure 1.1 gain their mass via the EW
 286 spontaneous symmetry breaking. This mechanism is described in Section
 287 1.1.5.1.

288 Before describing the fundamental interactions of the SM in the QFT
 289 formalism, let's introduce the main two types of particles according to their
 290 spin, i.e. intrinsic angular momentum: fermions and bosons.

291 Fermions

292 The fermions are the particles that follow the Fermi-Dirac statistics, i.e.
 293 obey the Pauli exclusion principle [9], resulting in a distribution of particles
 294 over energy levels in which two elements with the same quantum numbers
 295 cannot occupy the same states. The fermions include all particles with half-
 296 integer spin: quarks, leptons and baryons. A baryon is a non-fundamental
 297 particle composed of an odd number of valence quarks³ (consequently hav-

³The hadrons (baryons are mesons) are understood as a sea of partons being the valence quarks those which are more probable to be found in the hadron according to the parton distribution functions.

ing half-integer spin) and nearly all matter that may be encountered or experienced in everyday life is baryonic matter. Some examples of baryons are⁴ the proton ($u\ u\ d$), the neutron ($d\ d\ u$), Λ ($u\ d\ s$), Λ_c^+ ($u\ d\ c$) and Σ^+ ($u\ u\ s$). Apart from the 3-quark baryons, an exotic pentaquark state has been observed at LHCb experiment of the LHC [10].

The fundamental fermionic matter (Table 1.2) is organised in the three families of leptons and quarks:

$$\begin{bmatrix} \nu_e & u \\ e^- & d \end{bmatrix}, \begin{bmatrix} \nu_\mu & c \\ \mu^- & s \end{bmatrix}, \begin{bmatrix} \nu_\tau & t \\ \tau^- & b \end{bmatrix}$$

.

These three generations, which are defined as the columns in Figure 1.1, exhibit the same kind of gauge interactions and they only differ in their mass [11]. According to the EW symmetry, each family can be classified as:

$$\begin{bmatrix} \nu_\ell & q_u \\ \ell^- & q_d \end{bmatrix} \equiv \begin{pmatrix} \nu_\ell \\ \ell^- \end{pmatrix}_L, \begin{pmatrix} q_u \\ q_d \end{pmatrix}_L, \ell^-_R, q_{uR}, q_{dR}$$

(plus the corresponding antiparticles) where the subindices L and R stand from left and right handed particles respectively. This structure responds to the fact that left-handed particles convert different than right-handed ones under $SU(2)$ transformations. The left-handed fields are $SU(2)_L$ doublets and the right-handed ones $SU(2)_R$ singlets. This difference is explained with more detail in Section 1.1.3.

The fundamental representation of $SU(3)$ is a triplet, this is why each quark can appear in three different colours, whereas each antiquark can exhibit one of the corresponding “anticolours”.

The SM fermions properties are summarised in Table 1.2. As can be seen in its last rows, the neutrino flavour states do no correspond to the mass states (ν_1, ν_2, ν_3). What happens is that each flavour state is a quantum mechanical combination of neutrinos of different masses and viceversa. More details about the neutrino masses can be found in a dedicated text in Section 1.1.7.2

The fundamental fermions are usually understood as the fundamental building blocks of matter. However, while the building blocks are important, there is a point that also has to be taken into account, the force. Without force these fermions would not interact which each other. The particles that mediate these interactions are the gauge bosons.

⁴Between round brackets, the valence quarks are shown.

Family	Name	Mass	Q
Quarks	Up (u)	$2.16^{+0.49}_{-0.26}$ MeV	2/3
	Down (d)	$4.67^{+0.48}_{-0.17}$ MeV	-1/3
	Charm (c)	1.27 ± 0.02 GeV	2/3
	Strange (s)	93^{+11}_{-5} MeV	-1/3
	Top (t)	172.76 ± 0.30 GeV	2/3
	Bottom (b)	$4.18^{+0.03}_{-0.02}$ GeV	-1/3
Leptons	Electron (e^-)	$0.5109989461 \pm 0.0000000031$ MeV	-1
	Muon (μ)	$105.6583745 \pm 0.0000024$ MeV	-1
	Tau (τ)	776.86 ± 0.12 MeV	-1
	Electron neutrino (ν_e)	ν_e, ν_μ, ν_e	0
	Muon neutrino (ν_μ)	\neq	0
	Tau neutrino (ν_τ)	ν_1, ν_2, ν_3	0

Table 1.2: Properties of the quarks and leptons. The electric charge is represented here by Q. The ν_1, ν_2, ν_3 are the neutrino mass eigenstates.

331 **Bosons**

332 Bosons differ from fermions by obeying the Bose-Einstein statistics, thus,
 333 bosons are not limited to single occupancy for a determined state. In other
 334 words, the Pauli exclusion principle is not applied. All particles with integer
 335 spin are bosons; from the particles shown on the right columns of Figure 1.1
 336 to the mesons. Mesons, along with baryons, are part of the hadron family,
 337 i.e. particles composed of quarks (see Section 1.1.4). The particularity
 338 of mesons is that they are formed from an equal number of quarks and
 339 antiquarks (usually one of each) bound together by strong interactions.
 340 Some examples of mesons are π^+ ($u \bar{d}$), π^0 ($\frac{u\bar{u}-d\bar{d}}{\sqrt{2}}$), K^+ ($u \bar{s}$) and J/ψ
 341 ($c \bar{c}$).

342 The elementary vector bosons are the force carriers and presented in
 343 Table 1.1 while Higgs boson is a fundamental particle as well.

344 **Gauge Invariance**

345 Constituting one of the most successful theories of Physics, the SM is able
 346 to provide an elegant mathematical framework to describe the experimental
 347 physics results with great precision. Another key element to understand the
 348 SM is the concept of gauge invariance. As it is illustrated during the rest of
 349 the Section 1.1, by demanding that the Lagrangian remains invariant under
 350 local gauge transformations, the existence of the SM force-carrier bosons
 351 (γ, W^+, W^-, Z and g).

352 1.1.2 Quantum electrodynamics

353 The gauge invariance refers to the invariance of a theory under trans-
354 formations which the theory is said to posses internal symmetry. The trans-
355 formations which are applied in all space-time locations simultaneously are
356 known as “global” transformations while the ones that vary from one point
357 to another are “local”. Each local symmetry is the basis of a gauge theory
358 and requires the introduction of its own gauge bosons as it is discussed in
359 the following pages.

In QFT, particles are described as excitations of quantum fields that satisfy the corresponding mechanical field equations. The Lagrangians in QFT are used analogous to those of classical mechanics, where the equation of motion can be derived from the Lagrangian density function (\mathcal{L}) and the Euler-Lagrange equations for fields:

$$\frac{\partial \mathcal{L}}{\partial \phi} - \partial_\mu \frac{\partial \mathcal{L}}{\partial (\partial_\mu \phi)} = 0$$

360, where $\partial_\mu = \frac{\partial}{\partial x^\mu}$ denotes the partial derivatives with respect to the four-
361 vector x^μ and $\phi = \phi(\vec{x}, t)$ is the quantum field of a fermion or boson. The
362 Lagrangian density (or just Lagrangian, for simplicity) is used to express
363 the dynamics of the quantum field. In QFT, Noether’s theorem [12] relates
364 a symmetry in the \mathcal{L} to a conserved current.

365 The Dirac equation, $(i\gamma^\mu \partial_\mu - m)\Psi(x) = 0$, is one of the simplest relativistic field equations. Its Lagrangian describes a free Dirac fermion:

$$\mathcal{L}_0 = i\bar{\Psi}(x)\gamma^\mu \partial_\mu \Psi(x) - m\bar{\Psi}(x)\Psi(x) \quad (1.1)$$

367, being Ψ the wave function (spinor represented by four complex-valued
368 components) of the particle, γ^μ are the Dirac or gamma matrices,
369 $\{\gamma^0, \gamma^1, \gamma^2, \gamma^3\}$, m the mass of the fermion and $\bar{\Psi} = \Psi^\dagger \gamma^0$, the hermitic
370 conjugate of the wave function. The gamma matrices build a set of ortho-
371 gonal basis vectors for covariant vectors in a Minkowski space. The first
372 term of \mathcal{L}_0 is the kinetic term while the second is the mass term.

This Lagrangian is invariant under $U(1)$ global transformations such as:

$$\Psi(x) \xrightarrow{U(1)} \Psi'(x) \equiv \exp\{iQ\theta\}\Psi(x) \quad (1.2)$$

373, where $Q\theta$ is a real constant. The phase of $\Psi(x)$ is a pure convention-
374 dependent quantity without a physical meaning since the observables de-
375 pend on $|\Psi(x)|^2$.

However, if θ was x dependent, the transformation 1.2 would be:

$$\Psi(x) \xrightarrow{U(1)} \Psi'(x) \equiv \exp\{iQ\theta(x)\}\Psi(x) \quad (1.3)$$

, which is not longer a global transformation but a local transformation instead. The transformation in 1.3 would not let the \mathcal{L}_0 in 1.1 invariant because the derivative in the kinetic term would go as:

$$\partial_\mu \Psi(x) \xrightarrow{U(1)} \exp\{iQ\theta\}(\partial_\mu + iQ\partial_\mu\theta)\Psi(x) \quad (1.4)$$

376 .

The gauge principle is the requirement that the $U(1)$ phase invariance should hold locally. In order to do so, it is necessary to introduce an additional term to the Lagrangian so that when one applies $\Psi'(x) \equiv \exp\{iQ\theta(x)\}\Psi(x)$, the $\partial_\mu\theta$ term is canceled in 1.4. To achieve this invariance, a term with the vector gauge field A_μ is inserted. This field transforms as

$$A_\mu(x) \xrightarrow{U(1)} A'_\mu(x) \equiv A_\mu(x) + \frac{1}{e}\partial_\mu\theta \quad (1.5)$$

with a new covariant derivative:

$$D_\mu\Psi(x) \equiv [\partial_\mu + ieQA_\mu(x)]\Psi(x) \quad (1.6)$$

which transforms like the field:

$$D_\mu\Psi(x) \xrightarrow{U(1)} (D_\mu\Psi)'(x) \equiv \exp\{iQ\theta\}D_\mu\Psi(x)$$

377 .

The Lagrangian density can be defined by replacing the partial derivatives in \mathcal{L}_0 (1.1) by the covariant derivative in 1.6:

$$\begin{aligned} \mathcal{L}_{QED} &\equiv i\bar{\Psi}(x)\gamma^\mu D_\mu\Psi(x) - m\bar{\Psi}(x)\Psi(x) \\ &= i\bar{\Psi}(x)\gamma^\mu[\partial_\mu + ieQA_\mu(x)]\Psi(x) - m\bar{\Psi}(x)\Psi(x) \\ &= i\bar{\Psi}(x)\gamma^\mu\partial_\mu\Psi(x) - \bar{\Psi}(x)\gamma^\mu eQA_\mu\Psi(x) - m\bar{\Psi}(x)\Psi(x) \\ &= \mathcal{L}_0 - eQA_\mu\bar{\Psi}(x)\gamma^\mu\Psi(x) \end{aligned} \quad (1.7)$$

378 .

379 The resulting Lagrangian is invariant under $U(1)$ local transformation.
 380 When the conversions 1.3 and 1.5 take place, the effects of the transformation
 381 are canceled out. Along with the original Lagrangian (\mathcal{L}_0), the \mathcal{L}_{QED}
 382 has an additional term describing the interaction between the fermion Ψ
 383 and the gauge field A_μ with a strength proportional to the charge eQ . This
 384 term, $eQA_\mu\bar{\Psi}\gamma^\mu\Psi$, that has been generated only by demanding the gauge
 385 invariance under $U(1)$, is not other than the vertex of Quantum Electrodynamics
 386 (QED) (Figure 1.2).

This new A_μ term is the electromagnetic field and its quanta is the photon. A mass term containing $A^\mu A_\mu$ is forbidden because it would violate

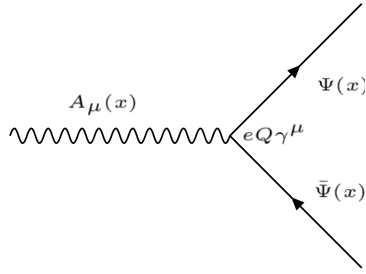


Figure 1.2: Three-point interaction vertex of QED.

the $U(1)$ local invariance. In consequence, the mediator of the new A_μ field, the photon, is predicted to be a massless particle. To make A_μ a propagating field it is necessary to add the kinetic term of the field A_μ :

$$\mathcal{L}_{kin} \equiv -\frac{1}{4}F_{\mu\nu}(x)F^{\mu\nu}(x) \quad (1.8)$$

, where $F^{\mu\nu} \equiv \partial_\mu A_\nu - \partial_\nu A_\mu$. The kinetic term $F_{\mu\nu}F_{\mu\nu}F^{\mu\nu}$ is already invariant under local $U(1)$ phase transformations. From the QED Lagrangian in 1.7 and the kinetic term in 1.8, the Maxwell equations can be derived to describe electromagnetism, the infinite range⁵ interaction that occurs between particles with electrical charge. The \mathcal{L}_{QED} with this kinetic term is written as:

$$\mathcal{L}_{QED} = \bar{\Psi}(x)(i\gamma^\mu\partial_\mu - m)\Psi(x) - eQ\bar{\Psi}(x)\gamma^\mu A_\mu\Psi(x) - \frac{1}{4}F_{\mu\nu}(x)F^{\mu\nu}(x) \quad (1.9)$$

³⁸⁷ 1.1.3 Electroweak interactions

³⁸⁸ 1.1.3.1 Weak interactions and Symmetries

³⁸⁹ The weak interaction is mediated by the W^+ , W^- and Z massive gauge
³⁹⁰ bosons. Due their large mass ($m_{W^\pm} = 80.4$ GeV and $m_Z = 91.2$ GeV), the
³⁹¹ range of the interactions is restricted to $\sim 10^{-18}$ m. It is responsible for
³⁹² radioactive decays, nuclear fusions and flavour changing⁶ decays of fermions
³⁹³ such as the decay of the muon ($\mu^- \rightarrow e^-\bar{\nu}_e\nu_\mu$).

³⁹⁴ Another particularity of this interaction is that it is the only interaction
³⁹⁵ that violates several fundamental symmetries. There is a relation between
³⁹⁶ symmetries and conservations laws which is known as Noether's theorem.
³⁹⁷ Classical physics examples of how the symmetries leads to conserved quanti-
³⁹⁸ ties are:

⁵Since the photon is (predicted to be) massless, the electromagnetic interaction has an infinite range.

⁶The leptonic charges are conserved.

- 399 • Invariance under change of time → Conservation of energy
- 400 • Invariance under translation in space → Conservation of momentum
- 401 • Invariance under rotation → Conservation of angular momentum

402 The three discrete symmetries that are fundamental for the SM formu-
 403 lation and are always hold for electromagnetic and strong interactions are:

- **Charge conjugation (\mathcal{C}):** Replace positive quantum charges by negative charges and vice versa. It does not affect mass, energy, momentum or spin. Essentially, it is a transformation that switches all particles with their corresponding antiparticles.

$$\mathcal{C}\Psi(\vec{r}, t) = \bar{\Psi}(\vec{r}, t)$$

- **Parity (\mathcal{P}):** Parity involves a transformation that changes the algebraic sign of the spatial coordinate system. It does not reverse time, mass, energy or other scalar quantities.

$$\mathcal{P} : \begin{pmatrix} x \\ y \\ z \end{pmatrix} \rightarrow \begin{pmatrix} -x \\ -y \\ -z \end{pmatrix} \quad \mathcal{P}\Psi(\vec{r}, t) = \Psi(-\vec{r}, t)$$

- **Time reversal (\mathcal{T}):** Consists in flipping the sign of the time

$$\mathcal{T} : t \rightarrow -t \quad \mathcal{T}\Psi(\vec{r}, t) = \Psi(\vec{r}, -t)$$

404 The simultaneous combination of this three symmetries mentioned above
 405 results in the \mathcal{CPT} symmetry, a profound symmetry of QFT which is
 406 consistent through all experimental observations [13]. Meanwhile, the \mathcal{P} -
 407 symmetry and the \mathcal{C} -symmetry can be combined to create the \mathcal{CP} -symmetry,
 408 the product of the two transformations. The weak interaction violates \mathcal{P}
 409 and \mathcal{C} symmetries. It also violates the combined \mathcal{CP} -symmetry. Therefore,
 410 through the CPT theorem [14], if the \mathcal{CP} is violated, \mathcal{T} is violated as well
 411 to preserve the \mathcal{CPT} invariance [15].

412 **Parity and Charge conjugation violation**

413 Previously theorised by Lee and Yang [16], the confirmation of the non-
 414 conservation of \mathcal{P} in weak interactions arrived with the Wu experiment in
 415 1957 [17]. Studying the beta decay of the Cobalt-60, Wu and collaborators
 416 found that the neutrino and the antineutrino have the relative orientations
 417 of spin and linear momentum fixed. The neutrino spin is always opposite

418 to the linear momentum, this is called left-handed particles. Meanwhile, for
419 the antineutrinos, the momentum is always aligned in the same direction as
420 the spin (right-handed particles). This causes the weak interactions which
421 emit neutrinos or antineutrinos to violate the conservation of parity.

Only left-handed particles and right-handed antiparticles are sensitive to the weak force. Dirac fermion fields, ψ , exhibit chiral symmetry and the right and left handed chiral states can be expressed as:

$$\psi_L(x) = \frac{1}{2}(1 - \gamma_5)\psi(x) \equiv P_L\psi(x) \quad (1.10)$$

$$\psi_R(x) = \frac{1}{2}(1 + \gamma_5)\psi(x) \equiv P_R\psi(x) \quad (1.11)$$

with

$$\gamma^5 \equiv \gamma_5 \equiv \gamma^0\gamma^1\gamma^2\gamma^3 = \begin{pmatrix} 1 & 0 \\ 0 & 1 \end{pmatrix}$$

422 where P_L and P_R are known as projection operators. The last equality is
423 valid in the Dirac representation.

424 In the same year, the \mathcal{C} violation was found too [18]. **Describe how**
425 **the \mathcal{C} violation was discovered**

426 \mathcal{CP} violation

427 While \mathcal{P} and \mathcal{C} are violated in a maximal way by the weak interactions,
428 the product of these two discrete transformations, \mathcal{CP} , is still a good sym-
429 metry (left-handed fermions \leftrightarrow right-handed fermions). Experiences such
430 as the Wu experiment respect the \mathcal{CP} symmetry and, in fact, in the \mathcal{CP} is a
431 symmetry of nearly all the observed phenomena. However, in 1964 Cronin
432 and Fitch discovered a slight (2%) violation of the \mathcal{CP} symmetry in the
433 decays of neutral kaons [19]. The \mathcal{CP} violation plays a fundamental role to
434 explain the dominance of matter over antimatter in the present universe.
435 More information about the matter-antimatter asymmetry can be found in
436 the dedicated text in Section 1.1.7.2.

437 Direct \mathcal{CP} violation is allowed in the SM if a complex phase is present
438 in the CKM matrix (described below). The “direct” \mathcal{CP} violation is a phe-
439 nomenon where the same decay process has a different probability for a
440 particle than for an antiparticle. An example of strong global \mathcal{CP} asy-
441 mmetry observed corresponds to the decay into two kaons and one pion. The
442 probability of $B^+ \rightarrow \pi^+ K^+ K^-$ is 20% higher than for $B^- \rightarrow \pi^- K^+ K^-$.

CKM matrix

The eigenstates that interact through weak interactions, known as “weak

eigenstates” (d' , s' , u'), are different from the the physically observed mass eigenstates (d , s , u). This make possible the charged-flavour-changing-weak decays trough the Cabibbo-Kobayashi-Maskawa (CKM) matrix. The CKM matrix, V_{CKM} , describes the mixing between the three generations of quarks in the SM. The coupling of two quarks i and j to a W boson is proportional to the CKM matrix element V_{ij} .

$$\begin{pmatrix} d' \\ s' \\ u' \end{pmatrix} = \begin{pmatrix} V_{ud} & V_{us} & V_{ub} \\ V_{cd} & V_{cs} & V_{cb} \\ V_{td} & V_{ts} & V_{tb} \end{pmatrix} \begin{pmatrix} d \\ s \\ u \end{pmatrix} \quad (1.12)$$

It is a 3×3 unitary matrix described by four independent parameters: three angles (θ_{ij}) and one phase (δ_{13}). Different equivalent representations of the CKM matrix can be found in literature but the Particle Data Group recommends the standard CKM parameterisation:

$$V_{CKM} = \begin{pmatrix} c_{12}c_{13} & -s_{12}c_{13} & s_{13}e^{-i\delta_{13}} \\ -s_{12}c_{23} - c_{12}s_{23}s_{13}e^{i\delta_{13}} & -c_{12}c_{23} - s_{12}s_{23}s_{13}e^{i\delta_{13}} & s_{23}c_{13} \\ s_{12}s_{23} - c_{12}c_{23}s_{13}e^{i\delta_{13}} & -c_{12}s_{23} - s_{12}c_{23}s_{13}e^{i\delta_{13}} & c_{23}c_{13} \end{pmatrix} \quad (1.13)$$

where $c_{ij} \equiv \cos \theta_{ij}$ and $s_{ij} \equiv \sin \theta_{ij}$, with i and j labelling the generations ($i, j \in \{1, 2, 3\}$). The angles θ_{12} , θ_{23} and θ_{13} are known as Euler angles. The complex phase δ_{13} allows the \mathcal{CP} violation [20]. There are other popular parameterisations such as the Kobayashi-Maskawa one or the Wolfenstein one.

The different elements of the CKM matrix are determined experimentally and are summarised in Table 1.3. As can be seen in this table, the largest values correspond to the diagonal elements of the CKM matrix. This implies that the processes that do not change the flavour are strongly preferred over the family-changing charged currents. For instance, for the top quark, the decay to any of the three down-type quarks is allowed but only $|V_{td}|^2 \times 100\% = 0.0064\%$ of times will decay to a down quark and $|V_{ts}|^2 \times 100\% = 0.14\%$ to a strange quark.

check: [42]

1.1.3.2 Electroweak unification

At energies above the scale of the mass of the weak vector bosons ($E_{EW} \sim m_Z \sim m_W \sim 100 \text{ GeV}$), the electromagnetic and weak interactions are unified into the Electroweak (EW) force. In other words, electromagnetism and weak interactions are simultaneously described by the symmetry

CKM element	Value
V_{ud}	0.97370 ± 0.00014 [21] [22]
V_{us}	0.2245 ± 0.0008 [23] [24]
V_{cd}	0.221 ± 0.004 [25] [26] [27]
V_{cs}	0.984 ± 0.011 [28][29] [30]
V_{cb}	0.0410 ± 0.0014 [31][32]
V_{ub}	0.0038 ± 0.00024 [33] [34][35]
V_{td}	0.0080 ± 0.0003 [36][37]
V_{ts}	0.0380 ± 0.0011 [36][37]
V_{tb}	1.013 ± 0.030 [38][39][40]

Table 1.3: Magnitude of the nine elements of the CKM matrix. The mean for the different measurements has been done by [41]. **Igual me he venido arriba con las referencias. Son las que daba el Particle Data Group**

466 group $SU(2)_L \times U(1)_Y$. The subindex L refers to left-handed fields and Y
 467 to the weak hypercharge. In contrast, at low energies, this interactions are
 468 treated as independent phenomena, the electromagnetism is described QED
 469 and the weak interaction by Fermi's theory.

In the EW model (Glashow-Salam-Weinberg model), two new quantum numbers are assigned to the particles of the SM: the weak isospin (\vec{T}) and Y . Here, the left-handed chiral states of fermions form isospin doublets (χ_L) with $T_3 = \pm 1/2$ and the right-handed form chiral states are composed of isospin singlets (χ_R) with $T_3 = 0$. For a particle, T_3 is the third component of the \vec{T} , which is related to the electric charge (Q) and the $U(1)$ hypercharge by Gell-Mann-Nishijima relation:

$$Q = T_3 + \frac{1}{2}Y \quad (1.14)$$

470 With this expression, the electromagnetic coupling and the electroweak
 471 couplings are connected. Having χ_L with $T_3 = \pm 1/2$ and χ_R with $T_3 = 0$
 472 implies that a $SU(2)$ weak interaction can rotate left-handed particles (i.e.
 473 convert a left-handed e^- into a left-handed ν_e emitting a W^-) but cannot
 474 do the same with right-handed.

475 Using the gauge invariance principle it is possible to find the QED and
 476 QCD Lagrangians, as it is described in Sections 1.1.2 and 1.1.4 respectively.

The free Lagrangian, as in the case of QED and QCD is:

$$\begin{aligned}\mathcal{L} &= i \sum_{j=1}^3 \bar{\Psi}(x) \gamma^\mu \partial_\mu \Psi(x) \\ &= i \sum_{j=1}^3 \bar{\chi}_L(x) \gamma^\mu \partial_\mu \chi_L(x) + i \sum_{k=1}^3 \bar{\chi}_R(x) \gamma^\mu \partial_\mu \chi_R(x)\end{aligned}\quad (1.15)$$

where the wave function Ψ has been spited into the left isospin doublets χ_L and and right isospin singlets χ_R . The indices j and k run over the three generations of the SM. This Lagrangian should be invariant when a gauge transformation under the $SU(2)_L \times U(1)_Y$ symmetry group in the flavour space is applied:

$$\chi_L(x) \xrightarrow{SU(2)_L \times U(1)_Y} \chi'_L(x) = \exp\{i\alpha^n \tau_n\} \exp\{i\beta y\} \chi_L(x) \quad (1.16)$$

$$\chi_R(x) \xrightarrow{SU(2)_L \times U(1)_Y} \chi'_R(x) = \exp\{i\beta y\} \chi_R(x) \quad (1.17)$$

with $\alpha, \beta \in \mathbb{R}$ and $n \in \{1, 2, 3\}$. This transformation is given by the generators of $SU(2)_L \times U(1)_Y$, i.e. the Pauli matrices (τ_n) and the weak hypercharge y . Note that $SU(2)_L$ transformation, $\exp\{i\alpha^n \tau_n\}$, only acts on the doublet fields. This term containing the Pauli matrices is non-abelian like in QCD and, like in QCD, this leads to self-interacting terms.

To ensure invariance under $SU(2)_L \times U(1)_Y$, four different gauge fields have to be added (three from $SU(2)$ and one from $U(1)$). Four is also the correct number of gauge bosons needed to describe EW interactions: W^+ , W^- , Z and Pgamma. While the three week isospin currents couple to the triplet of vector bosons W_μ^n with $n \in \{1, 2, 3\}$, the weak hypercharge couples to an isosinglet B_μ . The fields W_μ^1 and W_μ^2 are electrically charged whereas W_μ^3 and B_μ are neutral fields. The EW covariant derivative is defined as:

$$D^\mu \chi_{L_j}(x) = [\partial_\mu - ig \frac{\tau_i}{2} W_\mu^i(x) - ig' \frac{y_j}{2} B_\mu(x)] \chi_{L_j}(x) \quad i \in [1, 2, 3] \quad (1.18)$$

$$D^\mu \chi_{R_j}(x) = [\partial_\mu - ig' \frac{y_j}{2} B_\mu(x)] \chi_{R_j}(x) \quad (1.19)$$

where g and g' are the interaction couplings to W_μ^i isotriplet and the B_μ isosinglet.

Using the derivatives in equations 1.18 and 1.19, the Lagrangian in 1.20 is already invariant under local $SU(2)_L \times U(1)_Y$ transformations:

$$\mathcal{L} = i \sum_{j=1}^3 \bar{\chi}_L^j(x) \gamma^\mu D_\mu \chi_L^j(x) + i \sum_{k=1}^3 \bar{\chi}_R^k(x) \gamma^\mu D_\mu \chi_R^k(x) \quad (1.20)$$

Finally, if kinetic terms for the gauge bosons are included in 1.20, the EW SM Lagrangian is obtained:

$$\begin{aligned}\mathcal{L}_{EW} = & i \sum_{j=1}^3 \bar{\chi}_L^j(x) \gamma^\mu D_\mu \chi_L^j(x) + i \sum_{k=1}^3 \bar{\chi}_R^k(x) \gamma^\mu D_\mu \chi_R^k(x) \\ & - \frac{1}{4} W_{\mu\nu}^n(x) W_n^{\mu\nu}(x) - \frac{1}{4} B_{\mu\nu}(x) B^{\mu\nu}(x)\end{aligned}\quad (1.21)$$

Where the addition of kinetic terms gives rise to cubic and quadratic self-interactions among the gauge fields. Note that the mass terms of the fields are forbidden in order to ensure local gauge invariance and since the physical W^+ , W^- and Z bosons have a mass different from zero, for the moment let's assume that something breaks the symmetry generating the observed masses.

The in \mathcal{L}_{EW} in 1.21 can be divided in two different parts according to the charge of the bosons: charged currents and neutral currents. Relating the charged currents (W_μ^1 and W_μ^2) to the W^+ and W^- bosons of the SM and the neutral (W_μ^3 and B_μ) ones with the Z and γ , it is possible to build linear combinations fo the original gauge fields that define the SM bosons.

Therefore, from the charged-current interactions, the W^+ and W^- bosons are:

$$W^\pm \equiv \frac{1}{\sqrt{2}}(W_\mu^1 \mp i W_\mu^2) \quad (1.22)$$

While for the neutral-current these combinations can be defined as a rotation of the so called Weinberg (or weak mixing) angle θ_W :

$$\begin{pmatrix} W_\mu^3 \\ B_\mu \end{pmatrix} \equiv \begin{pmatrix} \cos \theta_W & \sin \theta_W \\ -\sin \theta_W & \cos \theta_W \end{pmatrix} \begin{pmatrix} Z_\mu \\ A_\mu \end{pmatrix}$$

Rewriting this equation, the photon and Z -boson fields are

$$A_\mu = B_\mu \cos \theta_W + W_\mu^3 \sin \theta_W Z_\mu \quad = -B_\mu \cos \theta_W + W_\mu^3 \sin \theta_W \quad (1.23)$$

In order to ensure that this A_μ is the one of QED, apart from the Gell-Mann-Nishijima relation (equation 1.14), it is requiered that the couplings of the γ , W and Z satisfy the relation:

$$g \sin \theta_W = g' \cos \theta_W = e \quad (1.24)$$

495 .

Within the unified EW model, once θ_W is known, the properties of Z are specified. Current measurements of θ_W give a value of $\sin^2 \theta_W = 0.2310 \pm 0.0005$ [43].

499 There is no mass term for the bosons in the EW Lagrangian that has
500 been obtained in 1.21 by demanding the $SU(2)_L \times U(1)_Y$ local invariance,
501 which enters in contradiction with the experimental observations for the
502 W and Z bosons ($m_{Z,W} \sim 80$ GeV). The introduction of such a mass term
503 would break the symmetry, however, the it is possible to add the mass for
504 the W and Z bosons without loosing the properties of the symmetry. The
505 method to do so is known as Englert–Brout–Higgs–Guralnik–Hagen–Kibble
506 mechanism or, more commonly, just as Higgs mechanism. This mechanism
507 is described in Section 1.1.5.

508 1.1.4 Quantum chromodynamics

509 1.1.4.1 Quarks and colour

510 Quantum chromodynamics (QCD) is QFT-based theory for describing
511 the strong interactions between quarks and gluons (partons). This type of
512 interaction is the responsabile of the nuclear force, the one that acts between
513 the protons and neutrons of atoms binding them together. Without the
514 strong force, the protons inside the nucleus would push each other apart
515 due to the electromagnetic repulsion. It also holds the quarks within a
516 hadron together.

QCD is based in the $SU(3)$ symmetry group and its name derives from the “colour” charge, an analogous to the electric charge of QED but for strong interactions. The colour charge was introduced in 1964 [44] to explain how quarks could coexist within some hadrons apparently having the same quantum state without violating the Pauli exclusion principle. To satisfy the Fermi-Dirac statistics it is necessary to add an additional quantum number, the colour, to the theory. Each specie of quark (q) may have three different colours (q^α , $\alpha = 1, 2, 3$): red, green, blue. Baryons and mesons are described then by the colour singlet combinations:

$$B = \frac{1}{\sqrt{6}} \epsilon^{\alpha\beta\gamma} |q_\alpha q_\beta q_\gamma\rangle \quad M = \frac{1}{\sqrt{3}} \epsilon^{\alpha\beta} |q_\alpha \bar{q}_\beta\rangle$$

517 .

518 Additionally, it is postulated that all hadrons must have a global neutral
519 colour charge, i.e. the hadrons must be “colourless”. This assumption
520 is known as confinement hypothesis and it is made to avoid the existence
521 of non-observed extra states with non-zero colour. It is called colour con-
522 finement because it implies that it is not possible to observe free quarks
523 since they carry colour charge and, hence, they have to be confined within
524 colour-singlet combinations. Figure 1.3 depicts how different colours and
525 anticolours combine to create the “colourless” state.



(a) Quark colours combine to be colourless. (b) Antiquark colours also combine to be colourless.

Figure 1.3: Colour charge combinations for quarks and antiquarks

526 **1.1.4.2 Gauge invariance for $SU(3)$**

The dynamics of the quarks and gluons are controlled by the QCD Lagrangian. Using the power of the gauge invariance principle it is possible to deduce \mathcal{L}_{QCD} similarly to the reasoning developed in Section 1.1.2. Firstly, let's denote a quark field of colour α and flavour f by q_f^α . The vector $q_f^T \equiv (q_f^1, q_f^2, q_f^3)$ is defined under the $SU(3)$ colour space, meaning that each dimension corresponds to a colour. The Lagrangian

$$\mathcal{L}_0 = \sum_f \bar{q}_f (i\gamma^\mu \partial_\mu - m_f) q_f \quad (1.25)$$

is invariant under global $SU(3)$ transformation in the colour space,

$$q_f^\alpha \rightarrow (q_f^\alpha)' = U_\beta^\alpha q_\beta^\alpha, \quad UU^\dagger = U^\dagger U = 1, \quad \det U = 1 \quad (1.26)$$

527 .

In the $SU(N)$ algebra, $SU(N)$ is the group of $N \times N$ unitary matrices (U) which can be written in the form $U = \exp\{i(\lambda^a/2)\theta_a\}$ with $a = 1, 2, \dots, N^2 - 1$. Therefore, the $SU(3)$ matrices can be written as

$$U = \exp\left\{i\frac{\lambda^a}{2}\theta_a\right\} \quad (1.27)$$

where the index a goes from 1 to 8 for the arbitrary parameter θ_a and $\frac{\lambda^a}{2}$, which denotes the fundamental representation of the $SU(3)$ algebra. The Einstein notation for summation over repeated indices is implied. The matrices λ^a are traceless and satisfy the commutation relations [11]:

$$\left[\frac{\lambda^a}{2}, \frac{\lambda^b}{2}\right] = if^{abc} \frac{\lambda^c}{2} \quad (1.28)$$

528 , being f^{abc} the $SU(3)_C$ structure constants, which are real and totally 529 antisymmetric.

To satisfy the gauge invariance requirement, the Lagrangian has to be invariant under $SU(3)$ local transformations, i.e, transformations in which

the phase is dependent of the space-time location, $\theta_a = \theta_a(x)$. To fulfil the condition, the quark derivatives in the Lagrangian in 1.25 have to be substituted by covariant objects. Since there are eight independent gauge parameters, eight different gauge bosons $G_a^\mu(x)$ are needed⁷. These bosons are the eight gluons and the new covariant objects are:

$$D^\mu q_f \equiv \left[\partial_\mu + ig_s \frac{\lambda^a}{2} G_a^\mu(x) \right] q_f \equiv [\partial_\mu + ig_s G^\mu(x)] q_f$$

- 530 The compact matrix notation is used $[G^\mu(x)]_{\alpha\beta} \equiv \left(\frac{\lambda^a}{2} \right)_{\alpha\beta} G_a^\mu(x)$.

To ensure that the covariant derivative ($D^\mu q_f$) transforms like the q_f , the transformation of the gauge fields are:

$$D^\mu \rightarrow (D^\mu)' = UD^\mu U^\dagger \quad G^\mu \rightarrow (G^\mu)' = UG^\mu U^\dagger + \frac{i}{g_s} (\partial_\mu U) U^\dagger \quad (1.29)$$

. The quark and gluon fields transform under an infinitesimal local transformation, i.e. $\theta_a(x) = \delta\theta_a(x) \approx 0$, the $SU(3)_C$ unitary matrices (eq. 1.27) can be expressed as their first order expansion:

$$U = \exp\left\{ i \frac{\lambda^a}{2} \theta_a(x) \right\} \approx 1 + i \left(\frac{\lambda^a}{2} \right) \delta\theta_a(x)$$

and, consequently, the transformations for the colour-vector field (eq. 1.26) and gluon field (eq. 1.29) become:

$$\begin{aligned} q_f^\alpha &\rightarrow (q_f^\alpha)' = q_f^\alpha + \left(\frac{\lambda^a}{2} \right)_{\alpha\beta} \delta\theta_a q_f^\beta \\ G_a^\mu &\rightarrow (G_a^\mu)' = G_a^\mu - i \frac{i}{g_s} \partial_\mu (\delta\theta_a) - f^{abc} \delta\theta_b G_c^\mu \end{aligned}$$

531 .

532 In contrast to the transformation for the photon field in QED (equation 1.5), the non-commutativity⁸ of the $SU(3)_C$ matrices give rise to an
 533 additional term involving the gluon fields themselves ($-f^{abc} \delta\theta_b G_c^\mu$), as the
 534 relation 1.28 expresses. For constant $\delta\theta_a$, the transformation rule for the
 535 gauge fields is expressed in terms of the structure constants f^{abc} ; thus, the
 536 gluon fields belong to the adjoint representation for the colour group. There
 537 is a unique coupling at $SU(3)_C$, g_s . All the colour-triplet flavours couple to
 538 the gluon fields with exactly the same interaction strength.

⁷The eightfold multiplicity of gluons is labeled by a combination of color and anticolor charge (e.g. red–antigreen)

⁸Because the generators of $SU(3)$ do not commute, QCD is known as non-Abelian gauge theory.

It is necessary to introduce the corresponding fields strengths to build a gauge-invariant kinetic terms for the gluon fields.

$$G^{\mu\nu} \equiv -i\frac{-i}{g_s}[D^\mu, D^\nu] = \partial_\mu G^\nu - \partial_\nu G^\mu + ig_s[G^\mu, G^\nu] \equiv \frac{\lambda^a}{2}G_a^{\mu\nu}(x)$$

$$G_a^{\mu\nu} \equiv \partial_\mu G_a^\nu - \partial_\nu G_a^\mu - g_s f^{abc} G_b^\mu G_c^\nu$$

Under a $SU(3)_C$ transformation,

$$G^{\mu\nu} \rightarrow (G^{\mu\nu})' = U G^{\mu\nu} U^\dagger \quad (1.30)$$

and the colour trace $\text{Tr}(G^{\mu\nu}G_{\mu\nu}) = \frac{1}{2}G^{\mu\nu}G_{\mu\nu}$ remains invariant. Normalising the gluon kinetic term, the $SU(3)_C$ invariant QCD Lagrangian is obtained:

$$\mathcal{L}_{QCD} \equiv -\frac{1}{4}G_a^{\mu\nu}G_a^{\mu\nu} + \sum_f \bar{q}_f(i\gamma^\mu D_\mu - m_f)q_f \quad (1.31)$$

540 Note how the gluon-gluon vertex is find by demanding the gauge invari-
 541 ance under local $SU(3)_C$ transformation. A mass term is forbidden for the
 542 gluon fields by the $SU(3)_C$ gauge symmetry because something of the form
 543 $\frac{1}{2}m_G^2 G_a^\mu G_\mu^a$ would not be invariant under the transformation in 1.29. The
 544 gluons are, then, predicted by the theory to be spin-1 massless particles.

545 Thanks to the colour symmetry properties, this Lagrangian looks very
 546 simple and all its interactions depend on the strong coupling constant, g_s .
 547 In contrast to the Lagrangian derived for QED (eq 1.7), in \mathcal{L}_{QCD} the boson
 548 field have a self-interacting term. This gluon self-interactions give rise to the
 549 triple and quadratic gluon vertex (center and right diagrams in Figure 1.4).
 550 This self-interactions among the gluon fields can explain features the asymp-
 551 totic freedom and confinement, properties that were not present in QED.
 552 The asymptotic freedom causes interactions between particles to become
 553 asymptotically weaker as the energy scale increases and the corresponding
 554 length scale decreases. The confinement implies that the strong forces in-
 555 crease with the distance, therefore, as two colour charges are separated,
 556 at some point it becomes energetically favorable for a new quark-antiquark
 557 pair to appear rather than keep getting further. This new quarks bond with
 558 the previous two, preventing single quarks to be isolated. This mechanism,
 559 depicted in Figure 1.5, explains why the strong interaction is responsable
 560 for keeping the quarks together forming hadrons.

561 **Maybe, expand the QCD Lagrangian in 1.31 and explain its**
 562 **different elements.**

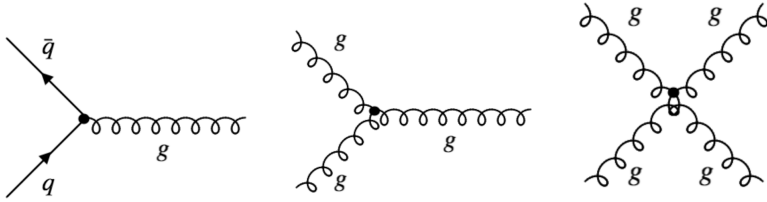


Figure 1.4: The predicted QCD interaction vertices arising from the requirement of $SU(3)_C$ local gauge invariance. The presence of the triples and quadruple gluon vertices is possible to the Non-Abelian nature of $SU(3)_C$.



Figure 1.5: The QCD colour confinement explains the inseparability of quarks inside a hadron in spite of investing ever more energy. In this example, the mechanism is shown for a meson.

563 1.1.5 Particle masses

For the QED Lagrangian, \mathcal{L}_{QED} (eq. 1.9), it is clear how the mass of the photon must be zero in order to satisfy the $U(1)$ local gauge symmetry because, if a mass term for the vector gauge field A_μ is included, the \mathcal{L}_{QED} would be:

$$\mathcal{L}_{QED} = \bar{\Psi}(x)(i\gamma^\mu\partial_\mu - m)\Psi(x) - eQ\bar{\Psi}(x)\gamma^\mu A_\mu\Psi(x) - \frac{1}{4}F_{\mu\nu}(x)F^{\mu\nu}(x) + \frac{1}{2}m_\gamma^2 A_\mu A^\mu$$

and, with the $U(1)$ transformation in equation 1.5, the new mass term becomes:

$$\frac{1}{2}m_\gamma^2 A_\mu A^\mu \rightarrow \frac{1}{2}m_\gamma^2 (A_\mu + \frac{1}{e}\partial_\mu\theta)(A^\mu + \frac{1}{e}\partial^\mu\theta) \neq \frac{1}{2}m_\gamma^2 A_\mu A^\mu$$

564 Confirming that the photon mass term is not invariant under local $U(1)$
 565 and, consequently, that the photon must be massless to satisfy the gauge
 566 invariance. Experimental efforts to measure the mass of the photon have
 567 set an upper limit of $m_\gamma \leq 1 \times 10^{-18}$ eV [45].

568 With the Lagrangian of QCD in equation 1.31 happens the same, the
 569 mass term for the gluon fields are forbidden by the $SU(3)_C$ gauge symmetry.
 570 Therefore, the mediating bosons for the strong interactions are massless as
 571 well (experimentally, a mass as large as upper limits of a few MeV have
 572 been seted, see [46]).

573 While the prohibition of mass terms for the bosons of QED and QCD is
 574 not a problem, this requirement also applies to the $SU(2)_L$. This condition

575 enters into open contradiction with the measurements of large masses for
 576 the W ($m_W = 80.370 \pm 0.007$ (stat.) ± 0.017 (syst.) MeV[47]) and Z ($m_Z =$
 577 91.1852 ± 0.0030 GeV [48]) bosons of weak interactions. <- to do: Aquí
 578 no estoy utilizando las mismas medidas de la masa de m_W y m_Z
 579 que antes. He de escoger una and stick to it.

580 For weak interactions, the problem of massless particles do not only
 581 affect the bosons. Since under the $SU(2)_L$ transformations left-handed
 582 particles transform as weak isospin doubles and right-handed particles as
 583 isospin singlets, the mass term of a spinor field Ψ written as chiral states
 584 also breaks the required gauge invariance: $-m\bar{\Psi}(x)\Psi(x) = -m\bar{\Psi}(x)(P_R +$
 585 $P_L)\Psi(x) = -m(\bar{\Psi}_R(x)\Psi_L(x) + \bar{\Psi}_L(x)\Psi_R(x))$

586 The Higgs mechanism describes how both the W and Z bosons and the
 587 fermions acquire mass without breaking the local gauge symmetry of the
 588 SM.

589 1.1.5.1 The Higgs mechanism

Goldstone theorem and spontaneous symmetry breaking

For a scalar field ϕ with a Lagrangian of the form:

$$\mathcal{L} = \frac{1}{2}\partial_\mu\phi_i\partial^\mu\phi_i - V(\phi) \text{ where } V(\phi) = \frac{1}{2}\mu^2\phi_i\phi_i + \frac{1}{4}\lambda(\phi_i\phi_i)^2 \quad (1.32)$$

This Lagrangian is invariant under $\phi_i \rightarrow \phi'_i = R_{ij}\phi_j$, where R_{ij} are rotational matrices in 4-dimensions. The mass term is the one with $\phi_i\phi_i$ and the parameter λ has to be positive for \mathcal{L} to describe a physical system, if $\lambda < 0$ the potential is unbounded from below. Contrary, the parameter μ^2 can be either positive or negative. As depicted in Figure 1.6a, if $\mu^2 > 0$, the vacuum expectation value (i.e. minimum of potential) is located at the origin ϕ_0 and this \mathcal{L} would describe a spin-0 particle of mass μ . However, if $\mu^2 < 0$, the potential $V(\phi)$ has the form of Figure 1.6a and \mathcal{L} would not represent anymore the Lagrangian of a particle of mass μ . The vacuum expectation value is now multivalued:

$$\phi_0 = \pm\sqrt{-\frac{\mu^2}{\lambda}} \equiv \pm v$$

Expanding the field around the minima at $\phi_i = (0, 0, 0, v)$, the \mathcal{L} becomes:

$$\begin{aligned} \mathcal{L} = & \frac{1}{2}\partial_\mu\sigma\partial^\mu\sigma + \mu^2\sigma^2 - \sqrt{\mu^2\lambda}\sigma^3 - \frac{1}{4}\lambda^4 \\ & + \frac{1}{2}\partial_\mu\pi_i\partial^\mu\pi_i - \frac{1}{4}\lambda(\pi_i\pi_i)^4 - \lambda v\pi_i\pi_i\sigma - \frac{1}{2}\pi_i\pi_i\sigma^2 \end{aligned} \quad (1.33)$$

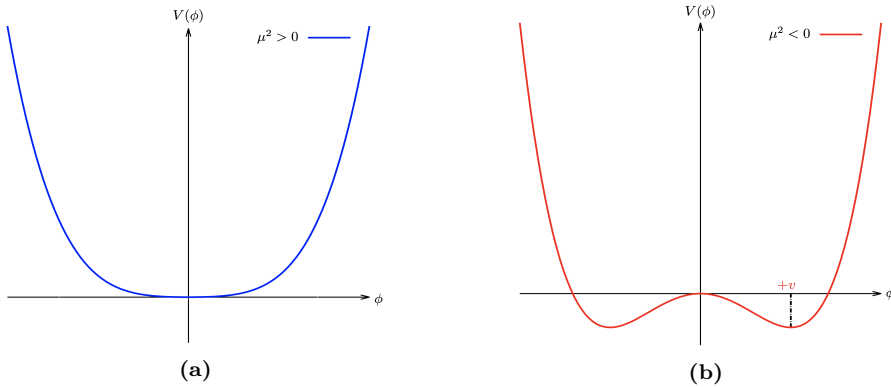


Figure 1.6: The potential $V(\phi)$ of Lagrangian 1.32 for (a) μ^2 positive and (b) negative.

590 where i runs from 1 to 3. Here $\sigma = \phi_4 - v$ and $\pi_i = \phi_i$ are new boson fields,
 591 being the latter massless and the with a mass of $m_\sigma^2 = -2\mu^2$. The new terms
 592 break the original symmetry because the symmetry of the Lagrangian is not
 593 longer a symmetry of the vacuum, it has been spontaneously broken. One
 594 massive σ boson and three massless π_i bosons with a residual $O(3)$ symmetry
 595 have appeared. This is a consequence of the Goldstone theorem which states
 596 that “for a continuous symmetry group \mathcal{G} spontaneously broken down to a
 597 subgroup \mathcal{H} , the number of broken generators is equal to the number of
 598 massless scalars that appear in the theory” [49]. Therefore, since the $O(N)$
 599 group has $N(N-1)/2$ generators, the $O(N-1)$ has $(N-1)(N-2)/2$ and,
 600 hence, $N-1$ Goldstone bosons appear. The example shown is for $N=4$.

The Higgs mechanism in the SM - Bosons

To apply this mechanism to the SM, it is necessary to generate mass for the W^+ , W^- and Z bosons while keeping the photon massless. In order to do so, the EW symmetry group $SU(2)_L \times U(1)_Y$ has to be broken into a $U(1)$ subgroup describing electromagnetism. A gauge-invariant interaction that gives masses to fermions without mixing chiral components is introduced by defining a $SU(2)$ isospin doublet of complex scalar field with hypercharge $Y = 1$:

$$\Phi = \begin{pmatrix} \phi^+ \\ \phi^0 \end{pmatrix}$$

Being ϕ^+ positively charged and ϕ^0 neutral. The Lagrangian \mathcal{L}_{Higgs} has to be added to the \mathcal{L}_{EW} in 1.21.

$$\mathcal{L}_{Higgs} = (D_\mu \Phi)^\dagger (D^\mu \Phi) - V(\Phi) \text{ where } V(\Phi) = \mu^2 \Phi^\dagger \Phi + \lambda (\Phi^\dagger \Phi)^2$$

with $\lambda > 0$ required for vacuum stability. When $\mu^2 > 0$, the minimum of the potential occurs when both fields (ϕ^+ and ϕ^0) are at zero. If $\mu^2 < 0$, the minimum of the potential has an infinite number of degenerate states that

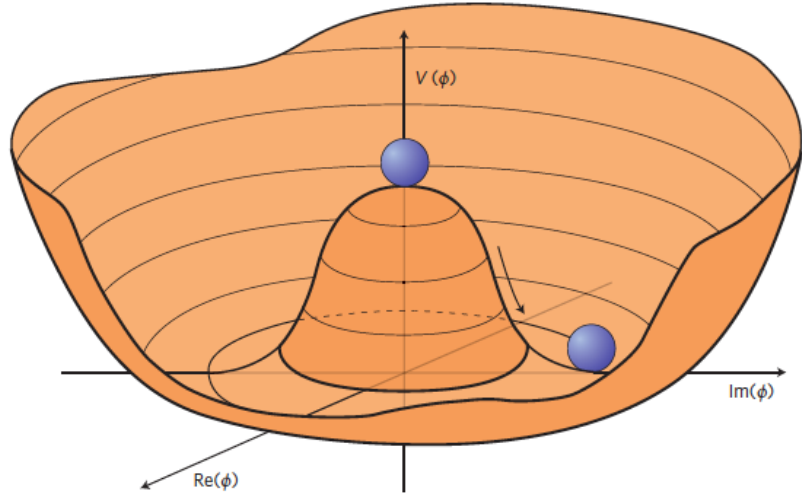


Figure 1.7: An illustration of the Higgs potential $V(\Phi)$ in the case of $\mu^2 < 0$. Choosing any particular point in the circle defined by v spontaneously breaks the $U(1)$ rotational symmetry. This type of potential is frequently called “Mexican hat”.

satisfy $\Phi^\dagger \Phi = \mu^2/2\lambda$ and the physical vacuum state will correspond to any particular point on the circle of Figure 1.7. Having to chose a particular point breaks the global $U(1)$ symmetry of the Lagrangian. Without loss of generality, in this scenario, the ground state Φ_0 can be chosen to be:

$$\Phi_0 = \frac{1}{\sqrt{2}} \begin{pmatrix} 0 \\ v \end{pmatrix} \text{ where } v = 2\sqrt{\frac{\mu^2}{\lambda}}$$

being v the vacuum expectation value. This defines the already mentioned circle in the minimum of $V(\Phi)$ in the $\mu^2 < 0$ scenario.

The Lagrangian density must be formulated in terms of deviations from one of these ground states. This can be done by introducing an excitation, $h(x)$, that can be understood as a small deviation of the field from the ground state. Accordingly, the fields can be expanded around the minimum as:

$$\Phi = \frac{1}{\sqrt{2}} \begin{pmatrix} 0 \\ v + h(x) \end{pmatrix} \exp\{i\chi(x)\}$$

The new field $\chi(x)$ can be set to zero in the so called “unitary gauge”.

$$\Phi = \frac{1}{\sqrt{2}} \begin{pmatrix} 0 \\ v + h(x) \end{pmatrix} \quad (1.34)$$

Expanding the covariant derivative of the \mathcal{L}_{Higgs} :

$$\begin{aligned}
 (D_\mu \Phi)^\dagger (D^\mu \Phi) &= \left| \left(\partial_\mu + ig \frac{\tau^k}{2} W_\mu^k(x) + ig' \frac{y}{2} B_\mu \right) \right|^2 \\
 &= \frac{1}{2} \left| \begin{pmatrix} \partial_\mu + i\frac{1}{2}(gW_\mu^3 + g'\frac{y}{2}B_\mu) & i\frac{g}{2}(W_\mu^1 - iW_\mu^2) \\ i\frac{g}{2}(W_\mu^1 - iW_\mu^2) & \partial_\mu - i\frac{1}{2}(gW_\mu^3 - g'\frac{y}{2}B_\mu) \end{pmatrix} \begin{pmatrix} 0 \\ v+h \end{pmatrix} \right|^2 \\
 &= \frac{1}{2}(\partial_\mu h)^2 + \frac{1}{8}(v+h)^2 |W_\mu^1 - iW_\mu^2|^2 \\
 &\quad + \frac{1}{8}(v+h)^2 |gW_\mu^3 - g'B_\mu| + (\text{interaction terms})
 \end{aligned}$$

Where the τ_k with $k = 1, 2, 3$ are the Pauli Matrices. In this equation there are terms mixing the W^3 and the B_μ fields that, by using the physical fields defined in equation 1.1.3.2, should disappear since the physical bosons do not mix. Applying the relation 1.1.3.2 into the covariant derivative,

$$(D_\mu \Phi)^\dagger (D^\mu \Phi) = \frac{1}{2} + \frac{g^2 v^2}{4} W_\mu^+ W^{-\mu} + \frac{g^2 v^2}{8 \cos^2 \theta_W} Z_\mu Z^\mu + 0 A_\mu A^\mu$$

, the W^+ , W^- and Z bosons have finally acquired mass. Through the Higgs mechanism, their masses within the SM are:

$$M_W = \frac{1}{2} g v \quad M_Z = \frac{1}{2} \frac{g v}{\cos \theta_W}$$

603 Additionally, a new scalar field $h(x)$ has appeared with its correspondent
 604 mass term, the Higgs field. Note that the $h(x)$ was introduced as a perturba-
 605 tion from the ground state of the Higgs potential $V(\Phi)$, so the Higgs boson
 606 can be understood as an excitation of the Higgs potential. Apart from cou-
 607 plings to the electroweak gauge fields, the Higgs field has also self-interaction
 608 vertices. The mass of this boson is $m_H = \sqrt{2}\mu$.

With this covariant term, the Higgs Lagrangian density of the system is obtained:

$$\begin{aligned}
 \mathcal{L}_{Higgs} &= \frac{1}{2}(\partial_\mu h)(\partial^\mu h) + \frac{g}{4}(v+h)^4 W_\mu W^\mu + \frac{g^2}{8 \cos^2 \theta_W} (v+h)^2 Z_\mu Z^\mu \\
 &\quad + \frac{\mu^2}{2}(v+h)^2 - \frac{\lambda}{16}(v+h)^4
 \end{aligned}$$

and expressing it in terms of the boson masses and coupling parameters, it can be written as:

$$\begin{aligned}\mathcal{L}_{Higgs} = & \frac{1}{2}(\partial_\mu h)(\partial^\mu h) - \frac{1}{2}m_H^2 h^2 + \frac{1}{2}m_W W_\mu W^\mu + \frac{1}{2}m_Z Z_\mu Z^\mu + gm_W h W_\mu W^\mu \\ & + \frac{g^2}{4}W_\mu W^\mu + g \frac{m_Z}{2\cos\theta_W} h Z_\mu Z^\mu - g^2 \frac{1}{4\cos^2\theta_W} h^2 Z_\mu Z^\mu - g \frac{m_H^2}{4m_W} h^3 \\ & - g^2 \frac{m_H^2}{32m_W^2} h^4 + \text{const.}\end{aligned}\tag{1.35}$$

As can be seen in the Lagrangian 1.35, the coupling strengths of the W and Z fields to the Higgs are proportional to m_W and m_Z respectively. This why it is said that the more a fundamental particle interacts with the Higgs boson, the more massive it is.

The Higgs mechanism in the SM - Fermions

The Higgs mechanism for spontaneous symmetry breaking of the $SU(2)_L \times U(1)_Y$ gauge group of the SM generates the masses of the W^\pm and Z bosons. For originating the mass of the fermions without violating the EW gauge symmetry a similar procedure is carried but taking into account that the left-handed particles transform different than the right-handed. To do so, additional terms including the Yukawa couplings are added into the Lagrangian. These terms are of the form:

$$-y_f (\bar{\chi}_L^f \Phi \chi_R^f + \bar{\chi}_R^f \Phi^\dagger \chi_L^f)$$

where the f superindex runs over all quarks and charged leptons. It is usual to express the second part of the sum just as “plus hermitic conjugate” (“+ h.c.”). Note that the hermitic conjugate part is necessary to ensure that expression fulfills the requirement for a hermitian operator to be self-adjoint in a complex Hilbert space. The different y_f constants are known as Yukawa couplings of the particle f to the Higgs field. The Higgs doublet is denoted by Φ . For the electron $SU(2)$ doublet, the element with this coupling can be written as:

$$\mathcal{L}_e = -y_e \left[(\bar{\nu}_e \bar{e})_L \begin{pmatrix} \phi^+ \\ \phi^0 \end{pmatrix} e_R + \bar{e}_R (\phi^{+*} \phi^{0*}) \begin{pmatrix} \nu_e \\ e \end{pmatrix}_L \right] \tag{1.36}$$

Here, y_e is the Yukawa coupling of the electron to the Higgs boson. After spontaneously breaking the symmetry as it is done in eq. 1.34, the Lagrangian in 1.36 becomes:

$$\mathcal{L}_e = \frac{-y_e}{\sqrt{2}} v (\bar{e}_L e_R + \bar{e}_R e_L) + \frac{-y_e}{\sqrt{2}} h (\bar{e}_L e_R + \bar{e}_R e_L) \tag{1.37}$$

The y_e is not predicted by the Higgs mechanism, but can be chosen to be consistent with the observed electron mass (m_e) so that $y_e = \sqrt{2}m_e/v$. Using this relation, the Lagrangian in 1.37 becomes:

$$\mathcal{L}_e = -m_e \bar{e}e - \frac{m_e}{v} \bar{e}eh \quad (1.38)$$

613 The first element of the Lagrangian in 1.38 gives mass to the electron and
 614 gives rise to the coupling of the electron to the Higgs fields in its non-
 615 zero vacuum expectation. The second term represents the coupling of the
 616 electron and the Higgs boson itself.

617 The non-zero vacuum expectation value occurs only in the neutral part
 618 of the Higgs doublet (the lower in $\Phi = \begin{pmatrix} \phi^+ \\ \phi_0 \end{pmatrix}$) due to the form in the
 619 ground state in 1.34. This implies that the combination $\bar{\chi}_L^f \Phi \chi_R^f + \bar{\chi}_R^f \Phi^\dagger \chi_L^f$
 620 can only generate masses for the fermions in the lower component of an
 621 $SU(2)$ doublet, i.e. the charged leptons and the down type quarks. Putting
 622 aside the procedure to give mass to the up-type quarks, this explains why
 623 the neutrinos do not get mass through the Higgs mechanism.

For the up-type quarks, a gauge invariant term can be constructed from $\bar{\chi}_L^f \Phi_c \chi_R^f + \bar{\chi}_R^f \Phi_c^\dagger \chi_L^f$:

$$\mathcal{L}_u = y_u (\bar{u} \bar{d})_L \begin{pmatrix} -\phi^{0*} \\ \phi^- \end{pmatrix} u_R + \text{h.c.}$$

Applying the symmetry breaking:

$$\mathcal{L}_u = \frac{-y_u}{\sqrt{2}} v (\bar{u}_L u_R + \bar{u}_R u_L) + \frac{-y_u}{\sqrt{2}} h (\bar{u}_L u_R + \bar{u}_R u_L)$$

with a Yukawa coupling between the up quark and the boson $y_u = \sqrt{2}m_u/v$, resulting in:

$$\mathcal{L}_u = -m_u \bar{u}u - \frac{m_u}{v} \bar{u}uh$$

624 .

Therefore, for Dirac fermions, mass terms that let the Lagrangian invariant under local gauge transformations can be constructed from

$$\mathcal{L} = -y_f [\bar{\chi}_L^f \Phi \chi_R^f + (\bar{\chi}_R^f \Phi \chi_L^f)^\dagger] \quad \text{or} \quad \mathcal{L} = y_f [\bar{\chi}_L^f \Phi_c \chi_R^f + (\bar{\chi}_R^f \Phi_c \chi_L^f)^\dagger]$$

. The left Lagrangian is used for the leptons and down-type quarks, while the right one is used for the up-type quarks. These elements give rise not only to the mass of the fermions but also to the interaction strengths

between these fermions and the Higgs boson. The Yukawa coupling of the fermions to the Higgs field is given by:

$$y_f = \sqrt{2} \frac{m_f}{v} \quad (1.39)$$

where the Higgs vacuum expectation value is fixed by the Fermi coupling G_F and is measured to be $v = \sqrt{2} G_F \approx 246.22 \text{ GeV}$. The G_F is measured from the μ^+ lifetime [50]. The G_F is also used to determine the magnitude of the elements in the CKM matrix.

The value of fermionic masses is not predicted by the SM but obtained through experimental observations. Given the $m_{top} = 172.76 \pm 0.30 \text{ GeV}$, it is of particular interest the Yukawa coupling of the top quark to the Higgs field, y_t , which is almost exactly equal to one. It is important to verify this because deviation of the measured y_t from the SM prediction would be a proof of new phenomena beyond the SM that could provide an answer to several open questions concerning the fundamental interactions of elementary particles.

1.1.6 Charge-Parity

Probably, this section is gonna be absorbed by 1.1.3

1.1.7 Wrap up

Perhaps the ultimate and definitive (if talking about definitive makes any sense) theory of particle physics is a simple equation with a small number of free parameters. Meanwhile, the SM is here, and while it is not the ultimate theory, it is unquestionably one of modern physics' greatest successes. Despite its achievements, many questions remain unsolved.

1.1.7.1 The parameters of the Standard Model

The SM contains 25 free parameters that must be determined through observation and experimentation. These are the masses of the twelve fermions (assuming color variations and antiparticles are not viewed as separate fermions), or, more precisely, the twelve Yukawa couplings to the Higgs field.

$$m_{\nu_1}, m_{\nu_2}, m_{\nu_3}, m_e, m_\mu, m_\tau, m_u, m_d, m_c, m_s, m_t \text{ and } m_b$$

The three coupling constants of describing the strength of the gauge interactions

$$g, g' \text{ and } g_s$$

the two parameters describing the Higgs potential (μ and λ) or, equivalently, its vacuum expectation value and the Higgs mass

$$v \text{ and } m_h$$

The three mixing angles and the complex phase of the CKM matrix and the four of the PMNS matrix (the Pontecorvo–Maki–Nakagawa–Sakata matrix is similar to the CKM matrix but for the mixing of neutrino-mass eigenstates with neutrino-falvour eigenstates):

$$\theta_{12}, \theta_{13}, \theta_{23}, \rho_{13}, \theta'_a, \theta'_b, \theta'_c \text{ and } \theta'_d$$

646 From the 25 free parameters of the SM, 14 are associated to the Higgs
 647 field, eight with the flavour sector and only three with the gauge interac-
 648 tions.

649 1.1.7.2 Problems with the Standard Model

650 While the SM is very good theory that has passed rigorous testing, this
 651 is not the ending of the story, there are several limitations of the SM and
 652 a variety phenomena that it does not explain. The SM does not cover all
 653 questions in the universe and, hence, physicist continue looking for better
 654 theories to explain more. There is a long list of small and minor issues with
 655 the SM but lets focus on the most relevant ones.

656 Gravity

657 Gravity is the first force that any person learns about and the one known
 658 by the humankind for the most time. The SM describes all the other funda-
 659 mental interactions but this one. In the Table 1.1, the four forces are
 660 presented along with the theories to describe them. While QCD, QED and
 661 EW interactions are part of the SM, the GR is not. GR is a geometric the-
 662 ory that currently describes the gravitation in modern physics. Some of the
 663 suggested solutions to integrate gravitational interactions in the SM consist
 664 in postulating a new force carrier particle, the “graviton”, that mediates
 665 this interaction in a similar way to how the gauge bosons were proposed.
 666 Other explanations state that the gravity can only be described by a deeper
 667 theory in which the time-space structure is not flat like it is in the SM but
 668 dynamic.

669 Neutrino masses

670 According to the SM the neutrinos are massless, nevertheless, many ex-
 671 periments confirm that this is not true [51]. This is due to a property of

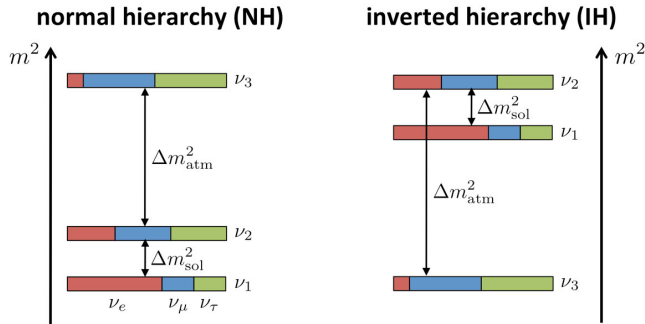


Figure 1.8: Two potential mass orderings of neutrinos are the normal ordering (normal hierarchy) and the inverted ordering (inverted hierarchy)

neutrinos that allows them to change their flavour while traveling through the space, this feature is known as “neutrino oscillations”. Each of the three neutrino flavours (ν_e , ν_μ , ν_τ) is a linear combination of three discrete neutrino-mass eigenstates (ν_i with $i \in \{1, 2, 3\}$) with mass eigenvalues (m_i). While the neutrino oscillation experiments could probe the squared neutrino-mass eigenvalues (Δm_{ij}^2), both the total scale of the masses and the sign of Δm_{ij} remains as some the most relevant open questions in particle physics. Regarding to the sign of Δm_{ij} , it is known that the mass of ν_2 is slightly higher than ν_1 ($\Delta m_{21}^2 \equiv m_2^2 - m_1^2 \sim 10^{-4}$ eV) but for the third mass eigenstate it has not been measured yet whether it is greater (normal ordering) or lower (inverted ordering) than the other two. This is referred as “hierarchy problem” and is depicted in Figure 1.8. Nevertheless, the absolute square difference is known ($\Delta m_{31}^2 \equiv |m_3^2 - m_1^2| \sim 10^{-3}$ eV).

Non-zero neutrino masses opened an interesting portal on beyond SM physics and, even though neutrinos are very elusive when it comes to detect them, some next-generation experiments such as Dune are very promising when it comes to set competitive and model independent limits on neutrino masses.

Regarding to the nature of this mass, one could add mass terms to the SM as it is done in Section 1.1.5.1 for the up-type quarks but the origin of the neutrino masses is still not known. It is possible that this mass comes from the Higgs mechanism, however, this is not clear. Also, if neutrinos gained mass through Yukawa interaction, it would imply the presence of right-handed neutrinos, which has not been observed.

696 Matter-antimatter asymmetry

697 In principle, the Big Bang should have produced an equal amount of matter
698 and antimatter which would all have then annihilated, leaving behind an

empty Universe filled with EM radiation. However, everything we see now is essentially totally constituted of matter, from the tiniest life forms on Earth to the greatest celestial objects. In comparison, there isn't a lot of antimatter around.

By looking at the CMB radiation, which contain the residual photons of the Big Bang, researchers have determined that there was a symmetry between the matter and antimatter content in the early universe. For every 3×10^9 antimatter particles, there were 3×10^9 and 1 matter particles. The matter and antimatter annihilate and produced the CMB and the remaining 1 part turned into all the stars and galaxies that are seen. The field of cosmology that studies the processes that produced an asymmetry between leptons and antileptons in the very early universe is called leptogenesis.

Researches carried during the last few decades have revealed that the laws of nature do not equally apply to matter and antimatter. So far, the only non-trivial difference between matter and antimatter found is the \mathcal{CP} asymmetry (or \mathcal{CP} violation, which has been introduced in Section 1.1.3). Alas, the quantity of \mathcal{CP} asymmetry included in the SM is insufficient to explain the composition of the observable universe and, hence, extensive searches of new sources of \mathcal{CP} violation are being carried.

In this context, the studies described in this thesis are part of the seek of new \mathcal{CP} -violation sources. As Section 1.4.2 details, the observation of a cross-section greater than the one predicted by the SM would imply that Higgs-single-top-quark associated production does not conserve \mathcal{CP} .

Strong \mathcal{CP} problem

723

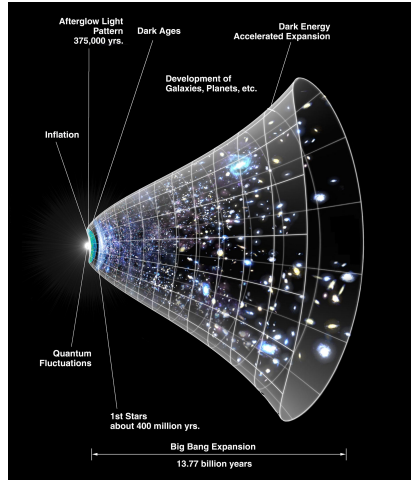
Dark energy

According to cosmological observations, the matter described by the SM only makes up around 5% of the universe. It turns out that roughly 68% of the universe is dark energy, which is not considered by the SM.

Dark energy is an unknown type of energy postulated to explain the observed accelerated expansion of the universe. This expansion is dominated by a spatially smooth component with negative pressure called dark energy. Modern cosmological measurements are based in supernovae, cosmic microwave background fluctuations, galaxy clustering and weak gravitational lensing, and methods agree with a spatially flat universe with about 30% matter (visible and dark) and 70% dark energy [52].

735 **Dark matter**

736 The rest of the energy content in the
 737 universe is the matter. Dark matter (DM) adds up for approximately
 738 85% of all matter and 27% of all en-
 739 ergy. This matter is called dark be-
 740 cause it does not interact with the
 741 electromagnetic field, so maybe a
 742 name such us invisible matter would
 743 have been more appropriate since
 744 rather than being dark it just does
 745 not emit or reflect light. The only
 746 way to interact with DM is via grav-
 747 itational interaction, which is bout
 748 25 orders of magnitud weaker than the weak force (as Table 1.1 shows).
 749 This is why DM is so difficult to detect. The SM does not provide a proper
 750 explanation but searches are being carrie and candidates such as weakly
 751 interacting massive particles (WIMPs) or axions have been proposed.



753 The existence of DM has been inferred through gravitational effects
 754 in astrophysical and cosmological observations. The rotational speed of
 755 the galaxies[53], the gravitational lensing[54] and the CMB angular spec-
 756 trum[55] are some examples of phenomena that cannot be explained with
 757 general relativity unless there is more present matter what it is seen.

758 Although the vast majority of scientific community accepts dark matter
 759 existence, alternative explanations for the observed phenomena have sug-
 760 gested. Most of these model consists in modifications of GR. The search
 761 of DM at particle colliders, which is focussed on large missing transverse
 762 energy signatures, have not result in any observation. Nevertheless, the ex-
 763 istence of a particle is never discarded, only its presence within the detector
 764 sensitivity limits.

765 **Unification of the strong interaction**

766 There are unification attempts to treat all interactions as one, with the same
 767 coupling constant and the same symmetry group⁹. In the same way the EW
 768 unifies QED and Weak forces, the grand unified theories (GUT) unifies all
 769 three interactions (QED, Weak and QCD) of the SM at high energies, where
 770 the coupling constants approach each other. Note that gravity is still left
 771 out, because it is much weaker than the other interactions.

⁹The most popular symmetry group for unification is $SU(5)$.

772 **Supersymmetry**

773 Originally motivated by the hierarchy problem, supersymmetry (SUSY) is
 774 an extension to the SM. In SUSY the equations for force and the equations
 775 for matter are identical and each SM particle has its supersymmetric partner
 776 “sparticle” from which differs by half spin unit. Therefore, for each SM
 777 fermion, the corresponding sfermion is a spin-0 scalar and hence a boson.
 778 Identically, there is a super-partner for each of the SM bosons. The gluons
 779 have the spin-half gauginos. The Higgs have a weak isospin doublet or spin-
 780 half Higgsinos ($\tilde{H}_{1,2}^0$ and \tilde{H}^\pm). The new particles interact through the forces
 781 of the SM but would have different masses

782 SUSY is not a theory but a principle and any theory with that property
 783 is said to be supersymmetric. So, there is not one but dozens of supersym-
 784 metric theories. A lot of focus has been put searching for supersymmetric
 785 particles but so far the supersymmetric partners have not been found, which
 786 is a good reason to be skeptical about SUSY. **maybe cite here some AT-**
 787 **LAS SUSY searches**

788 **Others**

789 The different problems mentioned hitherto are just some of the most relevant
 790 open questions that fundamental physics has not being able to answer yet.
 791 Nonetheless, there are many other issues whose discussion would need many
 792 pages and are outside the scope of this work. Even so, it won’t harm to list
 793 a few of them:

- 794 • Hierarchy problem: It is caused by the enormous distance between
 795 two fundamental physics scales: the EW scale ($\sim 10^2$ GeV) and the
 796 Planck scale ($\sim 10^{19}$ GeV).
- 797 • Strong \mathcal{CP} problem: It refers to the fact that, while QCD does not
 798 explicitly prohibit \mathcal{CP} violation in strong interactions, it has yet to be
 799 observed in experiments.
- 800 • Naturalness: It is the property that the dimensionless ratios between
 801 free parameters or physical constants appearing in a physical theory
 802 should take values of order unity. By looking at the parameters of the
 803 SM described in Section 1.1.7.1, it can be seen that the naturalness
 804 principle is not satisfied. For instance, the masses of the first gen-
 805 eration of fermions are in the range of 1 MeV while the top quark has
 806 a mass of 173 GeV. Though this is not a flaw in the theory itself, it is
 807 frequently seen as a sign of undiscovered principles hidden behind a
 808 more comprehensive theory.
- 809 • Composite Higgs models:

- Majorana neutrinos: It is not clear yet if neutrinos are Majorana particles, i.e. they are their own antiparticles ($\nu = \bar{\nu} = \nu_M$). Current experiments trying to solve this question are focused on neutrino-less double- β decay, which can occur only if neutrinos are Majorana particles.
- String theory: It is a theoretical framework in which fundamental point-like particles are understood as vibrational states of a more basic object, the so-called “string”. A string is a one-dimensional entity that can be either open (forming a segment with two endpoints) or closed (forming a loop) and may have other special properties. Despite being in development since the late 1970s, it has not been accepted nor discarded yet.

Most of theoretical concepts of the SM were in place by the end of the 1960s. With the discovery of the W and Z bosons at CERN in the mid 1980s and the Higgs boson in 2012, the SM has established itself as one of the major pillars of modern physics. The understanding of the universe at the most fundamental level is based in this theory, which has been tried to be summarised through the entire Section 1.1.

Despite its brilliance and success, the SM is not the ending of the story. As exposed above, there are far too many unanswered questions and loose ends. The HL-LHC (see Section ??) and the next generation of experiments will look for evidence of physics outside the SM in the next years.

Among the open questions, unresolved concerns and measurements to be completed, this research is focused on the top quark¹⁰. On one hand, contributions to the measurement of the polarisation of this quark are presented and, on the other hand, the study of the associated production of a single-top quark with a Higgs boson is present as well. Now that the basics of the SM have been settled, in the sections to come, the context of these two topics is being discussed.

1.2 Top quark

The top quark (t) or, for simplicity, just top is the up-type quark of the third generation of fermions. Sometimes called truth quark, its most distinctive feature is its huge mass, which is the largest among all fundamental particle particles. The left-handed top is the $Q = 2/3$ and $T_3 = +1/2$ member of the weak isospin doublet that also contains the bottom quark. The

¹⁰Here and in the following, the usage of the term top quark includes the top antiquark.

right-handed top quark is the $SU(2)_L$ weak isospin singlet ($Q = 2/3$ and $T_3 = 0$). Its phenomenology is driven by its large mass. The top quark is often regarded as a window for new physics since it provides a unique laboratory where to test the understanding of the SM.

Due to being so massive, its life time is very short ($\tau_t = 5 \times 10^{-25}$ s [54]). Actually, it is shorter than the hadronisation time ([cite](#)), this represents a unique opportunity to study quarks in free state, something that is very rare due to colour confinement, as explained in Section 1.1.4. In fact, the top quark is the only quark that can be investigated in isolation. Some of its properties, such as the spin information, can be accessed through its decay products and, consequently, be measured. This is the base to study its polarisation, a work that is contextualised in Section 1.2.4 and described in Chapter 4).

Another consequence of its large mass is that the top quark is the only quark with a Yukawa coupling (y_t) to the Higgs boson on the order of one; hence, a thorough understanding of its properties (mass, couplings, decay branching ratios, production cross section, etc.) can reveal crucial information on basic interactions at the electroweak symmetry-breaking scale and beyond. The main objective of this thesis is, precisely, the study of the top quark and Higgs boson interplay to, ultimately, help to determine if the y_t is that predicted by the SM or there is some \mathcal{CP} -violating phase that would affect the sign of the Higgs-top Yukawa coupling. The theoretical base for the understanding the associated production of a top quark and a Higgs boson given in Section 1.4 and the analysis investigating this matter is presented in Chapter 5.

870 Top quark mass

The most precisely studied property of the top quark is its mass. The most recent results for the top quark mass measurements result in $m_{top} = 172.76 \pm 0.30$ GeV [1]. This number is an average of the measurements at LHC with ATLAS (172.69 ± 66 GeV [56]) and CMS (172.6 ± 3.5 GeV at CMS [57]) and at Tevatron with CDF and D \emptyset (combined result: 174.30 ± 0.89 GeV [58]). These values are measured from the kinematics of $t\bar{t}$ events¹¹.

Figure 1.9 summarises the measurements of ATLAS and CMS for m_{top} from direct top quark decay.

¹¹This m_{top} results are sensitive to the top quark mass used in the MC generator that is usually interpreted as the pole mass.

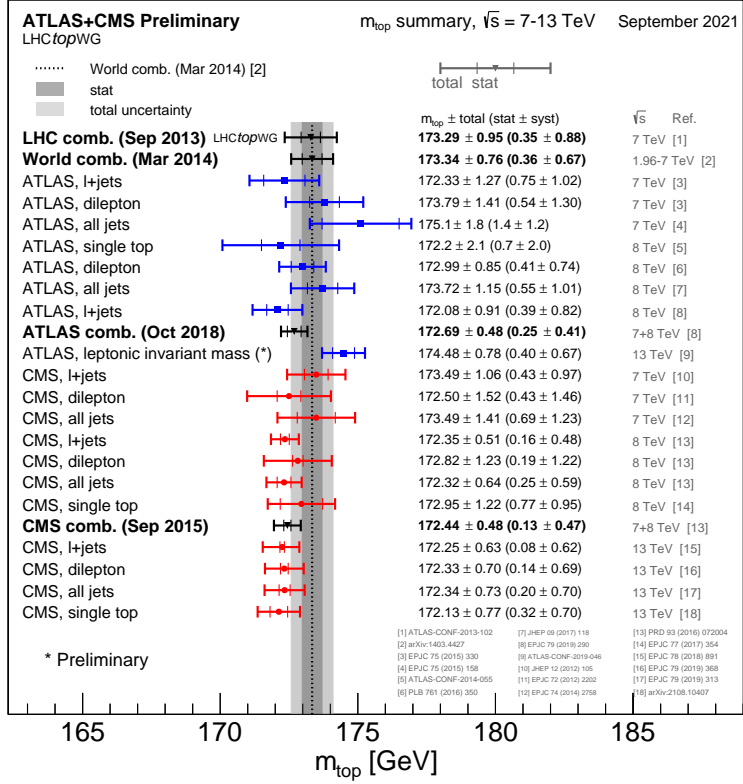


Figure 1.9: Summary of the ATLAS and CMS measurements from top quark decay. Results compared to LHC m_{top} combination.

879 1.2.1 Top quark discovery

880 In 1973, Kobayashi and Maskawa postulated the possibility of a third
 881 generation of quarks to explain \mathcal{CP} violations in kaon decays[59]. To match
 882 the names of the up and down quarks, the new generation's quarks were
 883 given the names top and bottom. The GIM mechanism, which predicted
 884 the existence of the yet-to-be-discovered charm quark, was used to make
 885 this prediction. When the charm was observed [60], the GIM was integ-
 886 rated into the SM and the postulation of the third family, and thus the top
 887 quark, gained acceptance. Shortly after the charm, the bottom quark was
 888 discovered in the E288 experiment at Fermilab [61], reinforcing the idea of
 889 the existence of the top quark. However, due to its large mass, it took 18
 890 years to confirm the existence of the top.

891 The top quark was observed for the first time at Tevatron with the
 892 CDF [62] and D \emptyset [63] detectors via flavour-conserving strong interaction
 893 in 1995. Back then and until the start of LHC Run-1, Tevatron was the
 894 only accelerator powerful enough to produce top quarks.

895 1.2.2 Top quark production at LHC

896 The LHC is sometimes referred as a top quark factory due to its ability
897 to produce such particles. In this collider, at pp collisions, the top quark
898 is mainly produced via two mechanisms: through QCD in top and anti-top
899 pairs ($t\bar{t}$), and by means of the Wtb vertex of EW in single-top quarks
900 associated with other particles. Apart from the $t\bar{t}$ (Section 1.2.2.1) and
901 single-top (Section 1.2.2.2) productions, the associated $t\bar{t} + X$ and four-top-
902 quark productions (Sections 1.2.2.3 and 1.2.2.4 respectively) are presented
903 as well.

904 Since the top quark production is si relevant at LHC, the top quarks
905 often constitute a main background in other physics analysis and, as a result,
906 a better understanding of this particle's properties will directly translate
907 into improvements in those searches.

908 1.2.2.1 Top pairs

909 The production top and anti-top pair of quarks is the largest source of
910 production of top quarks in hadron collisions. This process is one of the
911 most important at LHC because it allows to precisely study the properties
912 of the top quark. Additionally, due to the dominance of this production
913 mode, the top-quark-pair production is also a major background in many
914 searches for rare processes.

915 For the $p\bar{p}$ collisions at Tevatron or pp at LHC, the $t\bar{t}$ production is
916 described by perturbative QCD. In this approach, a hard scattering process
917 between the two hadrons is the result of an interaction between the quarks
918 and gluons that constitute these hadrons. This model is described with
919 detail in Section 2.2.7.

920 At LHC, the gluon fusion (Figure 1.10) dominates with a 90% of the $t\bar{t}$
921 production. It is followed by the quark and anti-quark annihilation (Figure
922 1.11), which accounts for a 10% of the the total top-quark-pair production.
923 Due to its primordial importance for the physics programme of LHC, the
924 theoretical calculations for the $t\bar{t}$ production are done to an accuracy of
925 next-to-next-to-leading order (NNLO) in QCD [64] and measured by AT-
926 LAS and CMS. Figure 1.12 shows the measurements for the $t\bar{t}$ production
927 cross section ($\sigma_{t\bar{t}}$) at $\sqrt{s} = 13$ TeV. The measurements and the theory cal-
928 culations are quoted at $m_{top} = 172.5$ GeV.

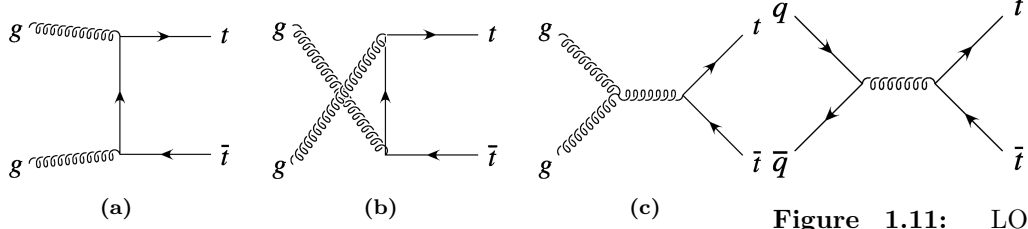


Figure 1.10: Representative Feynman diagrams of the LO processes contributing to the $t\bar{t}$ production through gluon fusion at LHC.

Figure 1.11: LO Feynman diagram for $t\bar{t}$ production via quark and anti-quark annihilation.

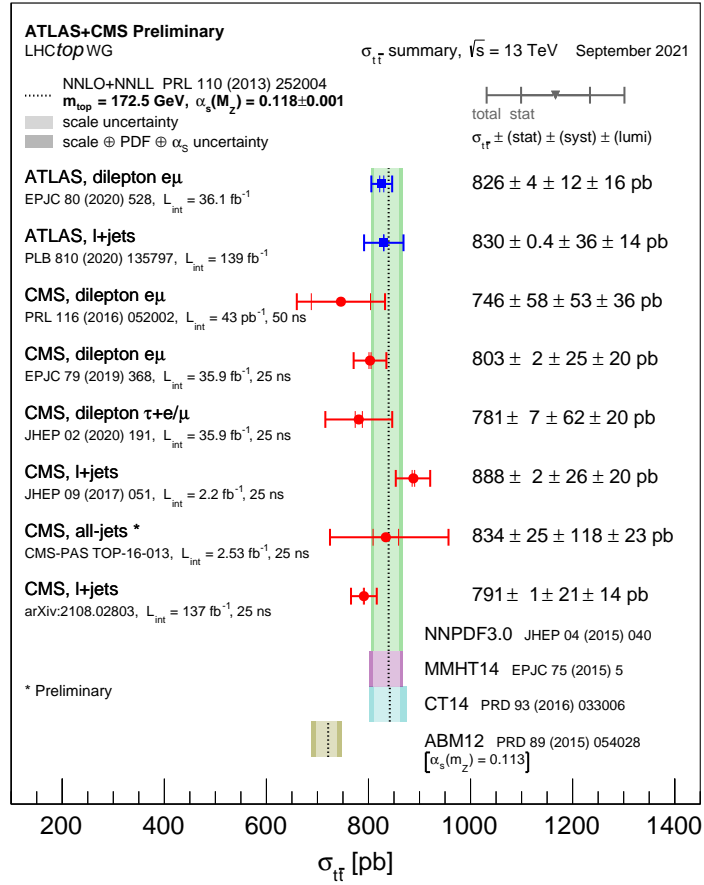


Figure 1.12: Summary of measurements $\sigma_{t\bar{t}}$ at 13 TeV compared to the exact NNLO QCD calculation complemented with NNLL resummation.

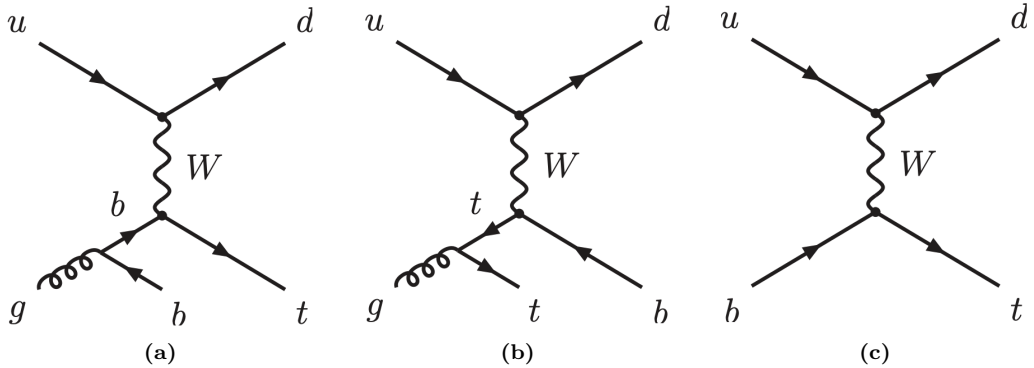


Figure 1.13: Representative Feynman diagrams for the single-top-quark production in the t -channel process.

929 1.2.2.2 Single top

930 In addition to the top-quark-antiquark-pair production, the single-top-
 931 quark processes are of great importance to the study of the top quark prop-
 932 erties at the LHC. This mechanism has a cross section three times smaller
 933 than that of $t\bar{t}$ and are almost exclusively produced through the electroweak
 934 Wtb vertex. This is precisely the reason why single-top-quark production is
 935 essential to gather information the Wtb interaction and to directly measure
 936 $|V_{tb}|$ at hadron colliders. The reason to decay and be produced from the
 937 bottom quark and not from strange or down quarks is because the CKM
 938 elements V_{ts} and V_{td} are much more smaller than V_{tb} being $|V_{tb}| = 0.99915$,
 939 $|V_{ts}| = 0.0403$ and $|V_{td}| = 0.00875$.

940 At LO, there are three production modes for single top, being the t -
 941 channel the dominant mechanism at the LHC with, approximately 70% of
 942 the single top quark cross section ($\sigma_{Single-t}$) at a $\sqrt{s} = 13$ TeV. The other
 943 processes are the s -channel and the associated production tW production.
 944 Only t -channel and tW productions are relevant to the electroweak single
 945 top production at LHC.

946 **t -channel**

947 This production mode, involves the scattering of a light quark and a gluon
 948 from the proton sea as shown in Figure 1.13. Note that additional dia-
 949 grams to those in Figure 1.13 are obtained by either replacing the u and d
 950 by a c and s quarks or by switching the light quarks in the fermion line.
 951 The diagrams for antitop production are the charge conjugate of the ones
 952 presented.

The measurements cross sections at 13 TeV for single-top ($\sigma_{t-channel,t}$) and single-anti-top ($\sigma_{t-channel,\bar{t}}$) quarks in the t -channel production are

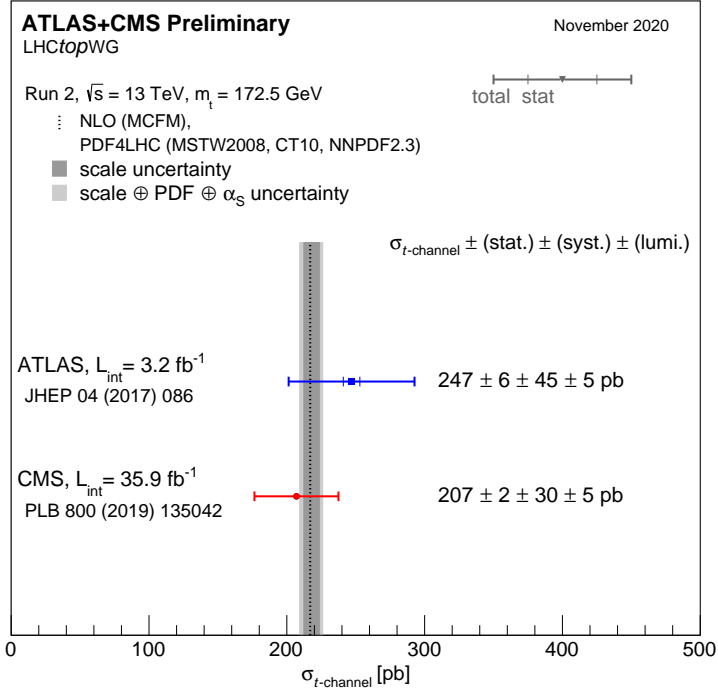


Figure 1.14: Summary of the ATLAS and CMS Collaboration measurements of the single top production cross-sections in the t -channel at 13 TeV.

shown in Figure 1.14. The theoretical calculations at NLO for $\sigma_{t\text{-channel}, t+\bar{t}}$ at 13 TeV are:

$$\begin{aligned}\sigma_{t\text{-channel}, t} &= 136^{+4.1}_{-2.9}(\text{scale}) \pm 3.5(\text{PDF} + \alpha_s) \text{ pb}, \\ \sigma_{t\text{-channel}, \bar{t}} &= 81.0^{+2.5}_{-1.7}(\text{scale}) \pm 3.2(\text{PDF} + \alpha_s) \text{ pb}, \\ \sigma_{t\text{-channel}, t+\bar{t}} &= 217^{+6.6}_{-4.6}(\text{scale}) \pm 6.5(\text{PDF} + \alpha_s) \text{ pb}.\end{aligned}$$

953 These numbers have been obtained using HATHOR 2.1 [65][66].

954 The dominant process in the SM is the one in diagram 1.13a, while
 955 the one in 1.13b is included in order to form a gauge invariant set but its
 956 contribution is not very significative since for the gluon it is easier to decay to
 957 $b\bar{b}$ pair than to a $t\bar{t}$ pair. These two $3 \rightarrow 2$ production modes are known as
 958 4 Flavour Scheme (FS) because the proton is considered to be composed by
 959 five quark flavours (u, d, c and s) and is characterised by having a b quark
 960 in the final state. This final state b quark is sometimes referred as second
 961 b and it has a transverse momentum (p_T) distribution peaking around 2 or
 962 3 GeV as can be seen in Figure 1.15. This is the reason why the final b
 963 quark from the gluon splitting frequently goes undetected, because it does
 964 not pass the p_T threshold of the detector.

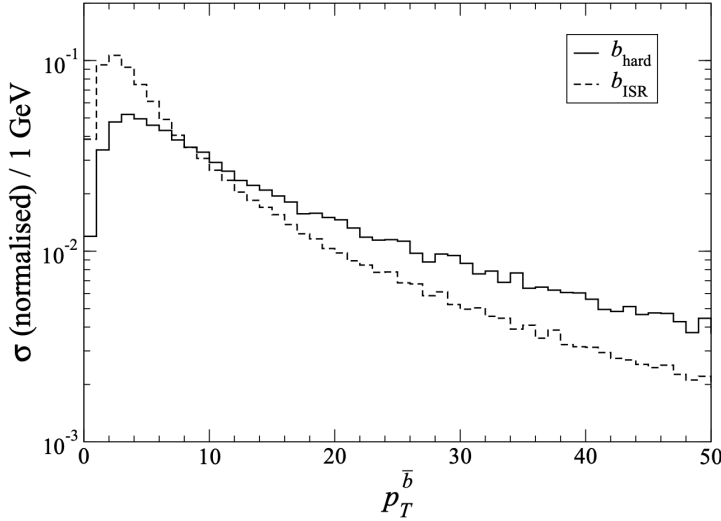


Figure 1.15: Normalised p_T distribution of the second b quark in the t -channel process, generated by Monte Carlo (MC) simulation [67].

965 The $2 \rightarrow 2$ process in 1.13c is known as 5FS because the proton is
966 considered to be composed by five flavours of quarks (u, d, c and s) and it
967 is characterised by having a b quark in the initial state. The simulations for
968 the 4FS and 5FS diagrams are produced separately and merged afterwards.
969 When adding the two contributions, some double-counting may appear due
970 to the overlap in the phase space so one has to be careful.

971 s-channel

972 The s -channel process for single-top is the one with less impact among
973 single-top production channels. It is depicted in Figure 1.16. This produc-
974 tion mode is also referred as the quark-antiquark annihilation or W^* process
975 and it is very similar to the Drell-Yann.

According to the LHC cross section group, at 13 TeV of center-of-mass energy, the cross sections for the single top and single anti-top production in the s -channel ($\sigma_{s\text{-channel}}$) are:

$$\begin{aligned}\sigma_{s\text{-channel},t} &= 6.35^{+0.18}_{-0.15}(\text{scale}) \pm 0.9(\text{PDF} + \alpha_s) \text{ pb}, \\ \sigma_{s\text{-channel},\bar{t}} &= 3.97^{+0.11}_{-0.09}(\text{scale}) \pm 0.15(\text{PDF} + \alpha_s) \text{ pb}, \\ \sigma_{s\text{-channel},t+\bar{t}} &= 10.32^{+0.29}_{-0.34}(\text{scale}) \pm 0.27(\text{PDF} + \alpha_s) \text{ pb}.\end{aligned}$$

976 Note that while at LHC the s -channel production has not been observed
977 at LHC, for Tevatron it was a significant part of the total single-top cross-
978 section.

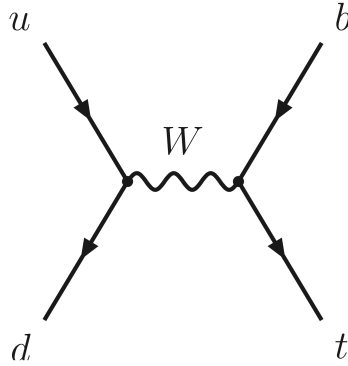


Figure 1.16: Representative Feynman diagram for the single-top-quark production in the s -channel.

Associated tW

Finally, the associated production of a single top quark with a W boson (sometimes referred as tW -channel) is represented by two the Feynman diagrams in Figure 1.18. To these two diagrams, the charge conjugate processes could be added to complete the tW mechanisms. The cross section for the associated tW is:

$$\sigma_{tW,t+\bar{t}} = 71.7 \pm 1.80(\text{scale}) \pm 3.40(\text{PDF} + \alpha_s) \text{ pb.}$$

979 This and all σ in the section are calculated for a top mass of $m_{top} =$
 980 172.5 GeV and NLO in QCD with HATHOR v.2.1. The PDF and α_s un-
 981 certainties are calculated using the PDF4LHC prescription [68] with the
 982 MSTW2008 68% CL NLO [69][70], CT10 NLO [71] and NNPDF2.3 [72]
 983 PDF sets, added in quadrature to the scale uncertainty.

984 **1.2.2.3 Associated $t\bar{t} + X$ production**

985 **1.2.2.4 Four tops**

986 Figure 1.22

987 **1.2.3 Top quark decay**

As advanced in the Section 1.2.2.2, due to the large V_{tb} element of the CKM matrix, the top quark decays almost entirely ($\sim 99.8\%$) thorough the medium of the Wtb vertex to a b quark and a W boson. The final state decay is classified according to the subsequent decay of the W boson. As W are massive vector bosons, its lifetime is very short ($\tau_W \approx 3 \times 10^{-25} \text{ s}$).

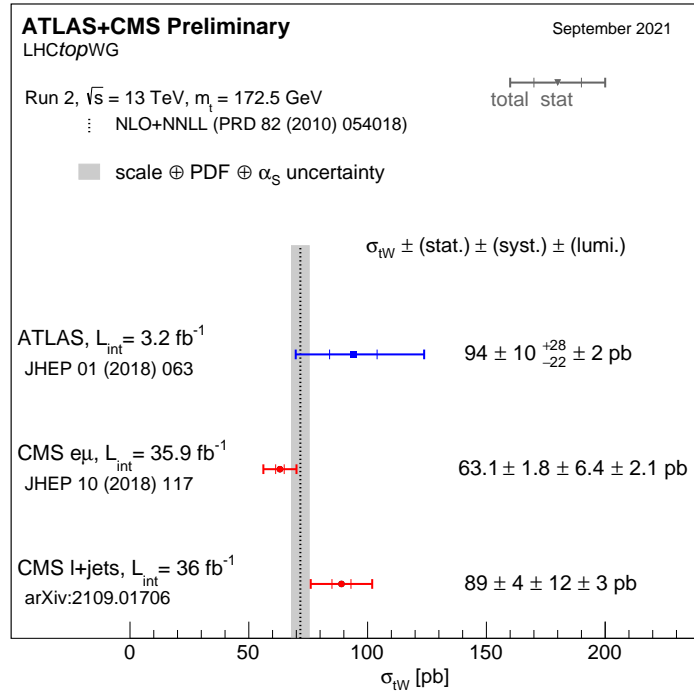


Figure 1.17: Cross-section measurements for the associated tW production boson performed by ATLAS and CMS at 13 TeV, and combined result compared with the NLO+NNLL prediction.

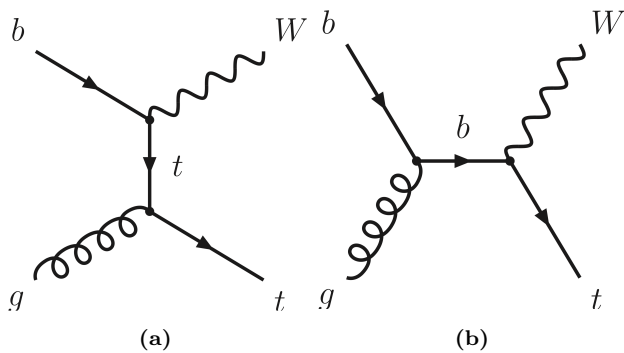


Figure 1.18: Representative Feynman diagrams for the single-top-quark production in association with a W boson.

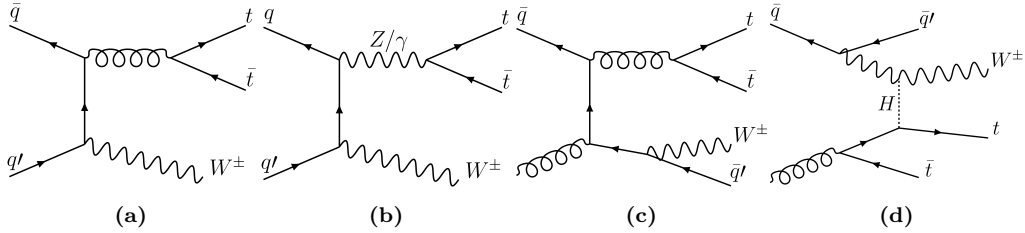


Figure 1.19: Representative Feynman diagrams for $t\bar{t}W$ production. Left diagrams show the $\bar{q}q' \rightarrow t\bar{t}W$ processes and right ones the $\bar{q}g \rightarrow t\bar{t}Wq'$ production.

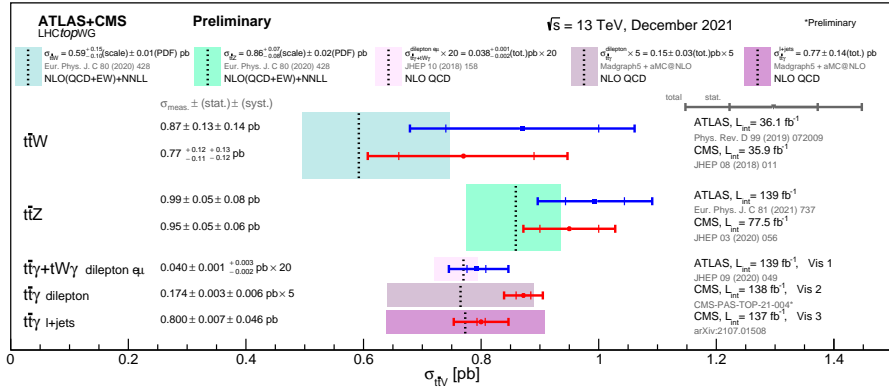


Figure 1.20: Summary of the ATLAS and CMS measurements of the $t\bar{t} + X$ production cross-sections at 13 TeV. Here $X = W, Z$ and γ .

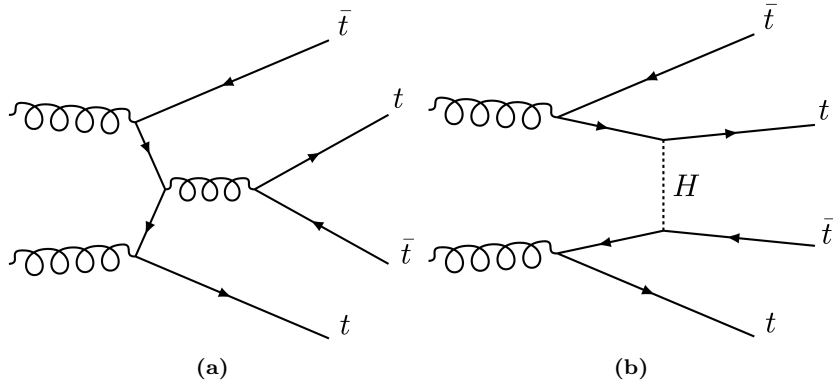


Figure 1.21: Representative Feynman diagrams for the $gg \rightarrow t\bar{t}t\bar{t}$ production.

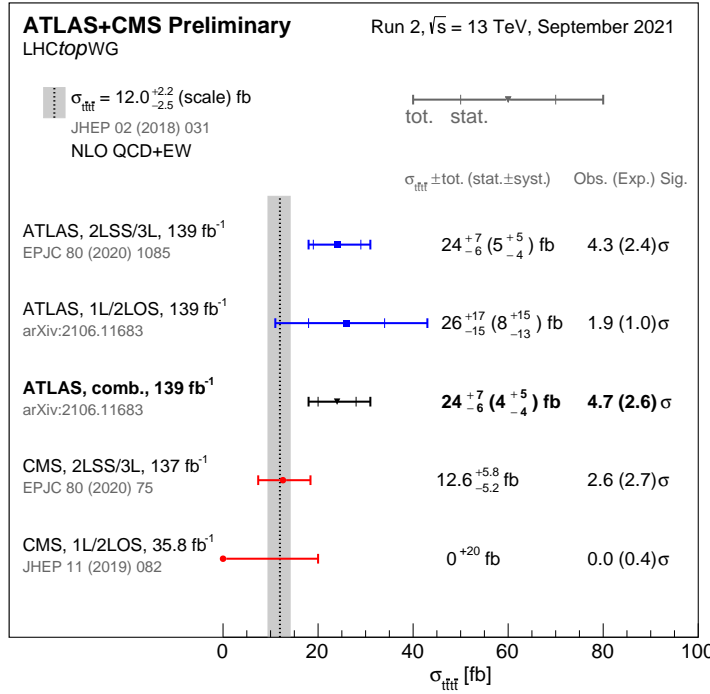


Figure 1.22: Summary of the ATLAS and CMS measurements of the $t\bar{t} t\bar{t}$ production cross-sections at 13 TeV in various channels

For the W^+ , the decay modes are:

$$\begin{aligned}
 W^+ &\rightarrow e^+ \nu_e & (10.71 \pm 0.16)\% \\
 W^+ &\rightarrow \mu^+ \nu_\mu & (10.63 \pm 0.15)\% \\
 W^+ &\rightarrow \tau^+ \nu_\tau & (11.38 \pm 0.21)\% \\
 W^+ &\rightarrow q\bar{q} \text{ (hadrons)} & (67.41 \pm 0.27)\% \\
 W^+ &\rightarrow \text{invisible} & (1.4 \pm 2.9)\%
 \end{aligned}$$

988 For the conjugate processes involving the W^- , the branching ratios (BR)
 989 are the same. Therefore, the W decay and consequently the t decay can be
 990 classified either as leptonic or hadronic. The decay chain of the top quark is
 991 represented in Figure 1.23. Due to its large mass, the W can decay to any
 992 quark except the top quark. For a certain decay mode, the BR is defined
 993 as the fraction times that the particle decays in that particular mode with
 994 respect to total possible decays.

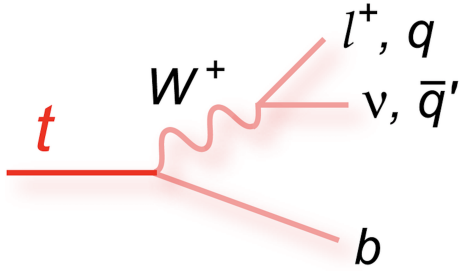


Figure 1.23: Decay of a top quark to a b quark and a W boson. The W boson can decay either leptonically to a neutrino and a lepton or hadronically to a pair of quarks. In the hadronic W decay, a jet triplet is formed along with the b quark.

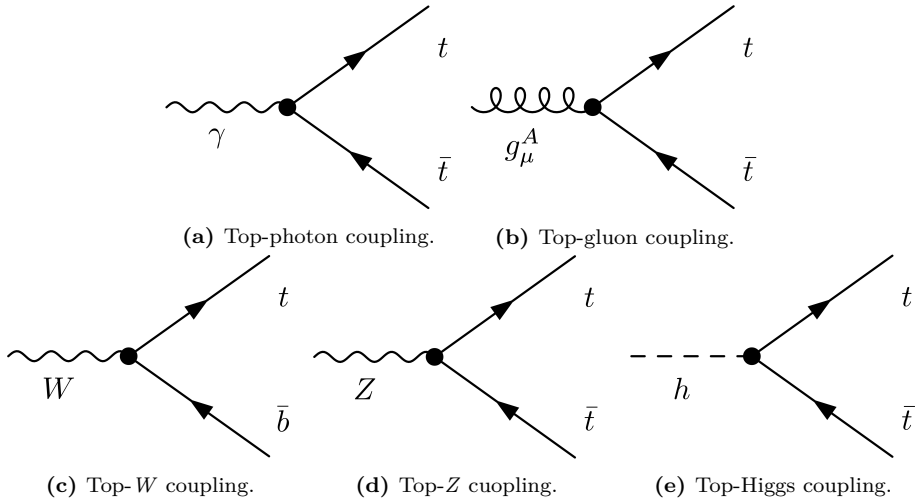


Figure 1.24: Top quark coupling to SM bosons.

995 1.2.4 Top quark polarisation

996 1.2.5 Top quark physics

997 **Probably this section is not necessary since the physics are**
 998 **mostly explained above.** The top quark couples directly to all SM vector
 999 (γ, W^+, W^-, Z, g) and scalar (H) bosons. For both photons and gluons,
 1000 the interaction is described by a vectorial fermion-gauge coupling $\bar{\Psi}\Psi A_\mu$.
 1001 From boson-fermion interacting term of the \mathcal{L}_{QED} in 1.9, the coupling of
 1002 the top quark to photons (Figure 1.24a) has a strength of $eQ\gamma^\mu = \frac{2}{3}e\gamma^\mu$.
 1003 Meanwhile, for the top-gluon coupling (Figure 1.24b), the expanded form
 1004 of the gluon-fermion term in the \mathcal{L}_{QCD} of 1.31 gives the $g_s \frac{\lambda_a}{2} \gamma^\mu$.

1005 For the charged weak current only the left-handed top couples
 1006 to the W^\pm with coupling. This is done via the Wtb vertex with a strength
 1007 of $g\gamma^\mu(1 - \gamma^5)V_{tb}$ (Figures 1.23 and 1.24c). The value of V_{tb} is given in Table

1008 1.3. The top couples to the Z bosons (Figure 1.24d) with unequal left and
 1009 right-handed components, $\frac{ig}{2\cos\theta_W}\gamma^\mu(v_t - a_t\gamma^5)$. Being $v_t = 1/2 - 2Q_t\sin^2\theta_W$
 1010 and $a_t = 1/2$. Finally, for the Higgs boson (Figure 1.24e), the top quark
 1011 couples with a Yukawa type interaction $\bar{\Psi}\Psi\phi$ with a strength $y_t = \frac{\sqrt{2}m_{top}}{v}$,
 1012 as equation 1.39 states. All of these couplings are flavour-conserving, with
 1013 the exception of the charged-current interaction with the W bosons.

1014 1.3 Higgs boson

1015 Following the top quark, the Englert-Brout-Higgs-Guralnik-Hagen-
 1016 Kibble-Higgs boson or, for simplicity, Higgs boson (H) or just Higgs is
 1017 the most massive particle in the SM with a mass of $m_H = 125.25 \pm 0.17$
 1018 GeV [2]. The value provided by [2] is an average of the ATLAS com-
 1019 bined measurement ($m_H = 124.86 \pm 0.27$ GeV [73]) and the CMS results
 1020 ($m_H = 125.46 \pm 0.16$ [74]).

1021 The Higgs boson was the final piece in the SM puzzle. Its existence
 1022 was theorised in 1964 by three independent groups: Englert-Brout [75],
 1023 Higgs [76] and Guralnik-Hagen-Kibble [77], and its discovery meant one of
 1024 the greatest successes of the SM. This theory was not only able to calculate
 1025 with great precision the physics but also predicted the existence of a particle
 1026 that was found later (see 1.3.1).

1027 In the SM, fundamental particles acquire mass through their interactions
 1028 with the Higgs fields. It is important to note that not all mass is related to
 1029 the Higgs mechanism. For instance, the mass of the proton does not come
 1030 from the interaction of its components with the Higgs but from the kinetic
 1031 energy of the particles that compose the proton.

1032 1.3.1 Higgs boson discovery

1033 Any particle physicist enthusiast remembers July 4th of 2012 pretty
 1034 well, it was LHC experiments ATLAS [78] and CMS [79] who announced
 1035 the discovery of a massive state H with the properties expected for the
 1036 Higgs boson.

1037 Both the ATLAS and CMS Collaborations reported excesses of events
 1038 for 2011 ($\sqrt{s} = 7$ TeV and $\mathcal{L} = 4.8 \text{ fb}^{-1}$) and 2012 ($\sqrt{s} = 8$ TeV and $\mathcal{L} = 458 \text{ fb}^{-1}$)
 1039 datasets of proton-proton collisions. This surplus of events was compatible
 1040 in its production and decay with the SM Higgs boson in the mass region
 1041 $m_H \in [124, 135]$ GeV with significances of 2.9σ for ATLAS and 3.1σ for
 1042 CMS. At Tevatron (circular proton-antiproton collider at Fermilab), the

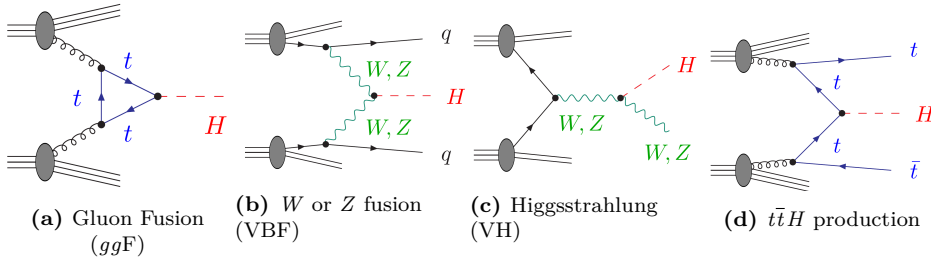


Figure 1.25: Lowest-order Feynman diagrams for the dominant production mechanisms of a Higgs boson at hadron colliders.

experiments CDF [80] and D \emptyset [81] also reported an excess in the mass region $m_H \in [120, 135]$ GeV.

1.3.2 Higgs boson production at LHC

One of the reasons why the Higgs boson was found the latest among SM fundamental particles is because it is a fairly heavy particle and, hence, it was necessary a lot of energy to produce it. Even though that colliders such us SLAC or LEP had enough energy, they were colliding electrons and positrons and, since the coupling of the Higgs to fermions is proportional to the fermions mass, the process $e^- e^+ \rightarrow H$ processes is highly suppressed¹² and, for this reason, there were not enough statistics of events with a Higgs boson. The most favoured way of producing a Higgs boson is trough the mediation of the heaviest fundamental particles in the SM because these have the strongest couplings with the Higgs and, consequently, the greater cross section.

The four most dominant processes for Higgs boson production at LHC are summarised in Figure 1.25:

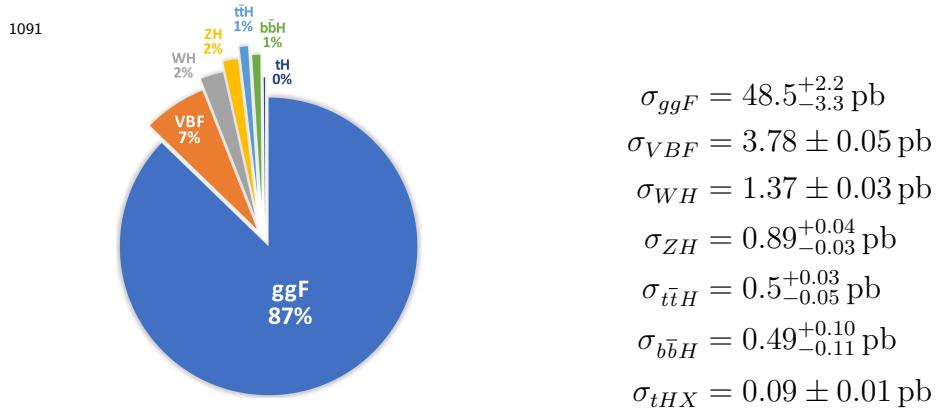
- **Gluon Fusion (ggF):** This channel is depicted in Figure 1.25a and, as the diagram shows, the process $gg \rightarrow H$ has to be mediated by a massive fermion loop. This due to the fact that there is no direct gluon-Higgs coupling within the SM. Although in principle all quarks should be included in the loop, in practise it is the top quark the one doing so because its coupling to the Higgs boson is 35 times stronger than the next-heaviest fermion, the bottom quark.

Due to the abundance of gluons in pp collisions, the ggF is very favoured at LHC.

¹²The dominant Higgs production in $e^- e^+$ annihilation is the so called Higgsstrahlung, an s -channel process in which the H is produced in association to a Z boson similarly to Figure 1.25c.

- **Vector Boson Fusion (VBF):** The second most important is the radiation by the incoming quarks of a W or Z vector bosons that fuse to form a Higgs as Figure 1.25b illustrates. The vector bosons of the process $V\bar{V} \rightarrow H$ are originated from initial state quarks which scatter thorough the final state (changing its flavours in the case of W fusion) producing two forward jets.
- **Higgsstrahlung (VH):** There is another significant contribution involving the W or Z bosons, the Higgsstrahlung or associated WH or ZH production. Here, a, off-shell W or Z (formed from the annihilation of two quarks) radiate a Higgs boson via $V^* \rightarrow VH$. Figure 1.25c depicts the VH associated production.
- **Quark-pair associated production ($q\bar{q}H$):** In this mode, the Higgs is produced from a $q\bar{q}$ pair via $q\bar{q} \rightarrow H$ with a $q\bar{q}H$ final state. Typically, the involved quark pair is either a $b\bar{b}$ or $t\bar{t}$. In the case of $t\bar{t}$ (Figure 1.25d), the top quarks decay before hadronising, leading to a high multiplicity final state.
- **Associated Higgs boson and single-top quark (tHX):** This sub-dominant contribution can be either a tHq or a tWH .

The cross section of the different procedures for Higgs boson production at $\sqrt{s} = 13$ TeV are shown in Figure 1.26 as a function of m_H . For Figure 1.26a, the σ_{tH} accounts for the t -channel and s -channel but not the tW -channel. Assuming a $m_H = 125.2$ GeV, the cross-sections for Higgs production are [82]:



1.3.3 Higgs boson decay

The Higgs boson has a very short lifetime ($\tau_H = 1.6 \times 10^{-22}$ s [82]) and, hence, is always detected through its decay products. Despite the expected

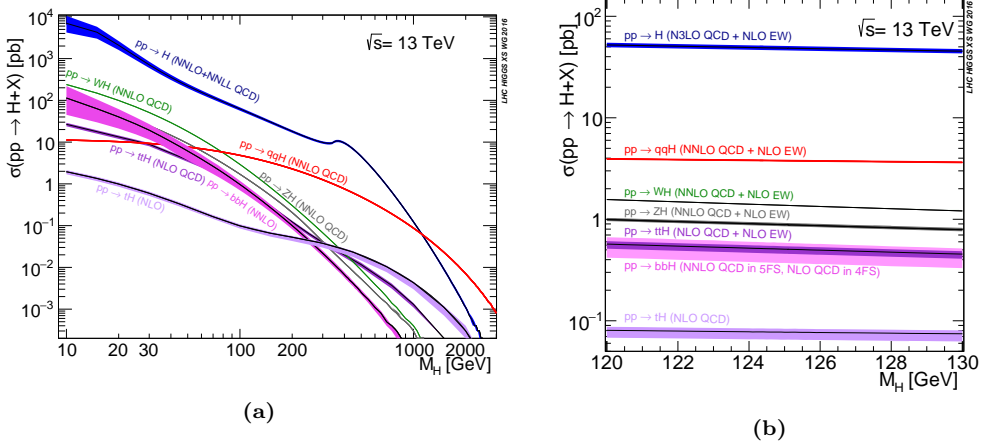
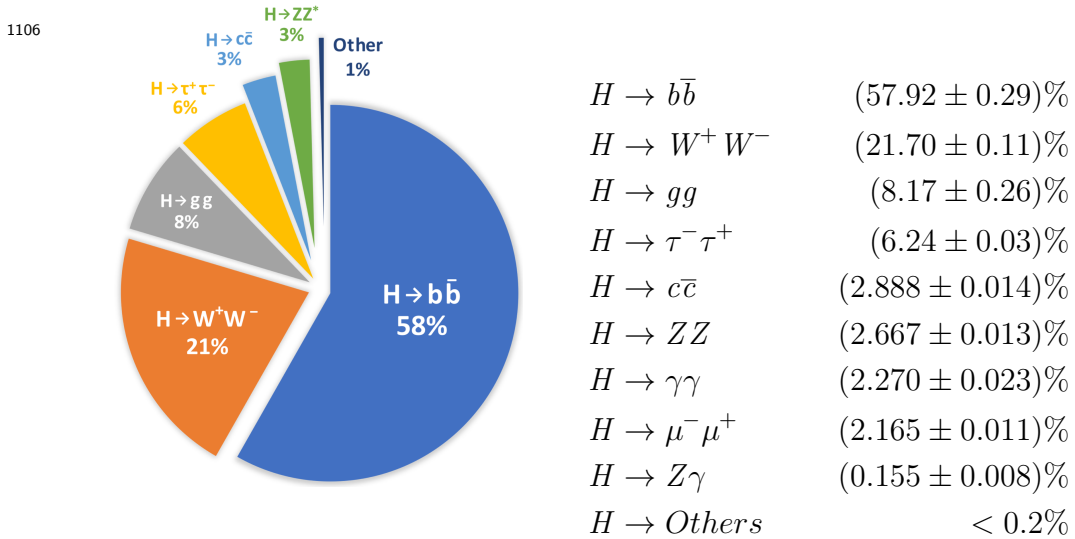


Figure 1.26: Higgs boson production cross sections as function of m_H at $\sqrt{s} = 13$ TeV [82].

large Yukawa coupling between the Higgs boson and the top quark, the $H \rightarrow t\bar{t}$ is forbidden because the $m_H < 2m_{top}$. Consequently, the most prominent decay mode is the $H \rightarrow b\bar{b}$ followed by the $H \rightarrow W^+W^-$. For the rest fermionic decays, the decay rates are ordered by the fermion mass. Regardless of the expected large coupling between the weak force bosons and the Higgs, the $H \rightarrow VV^*$ is suppressed due to the requirement that one vector boson has to be produced off-shell.

Add some diagrams of the Higgs decay modes

For the analysis carried in this thesis, are of particular the decays $H \rightarrow W^+W^-$, $H \rightarrow ZZ$ and $H \rightarrow \tau^-\tau^+$. Sorted by its importance and assuming a $m_H = 125.2$ GeV, the BR for the Higgs are [83]:



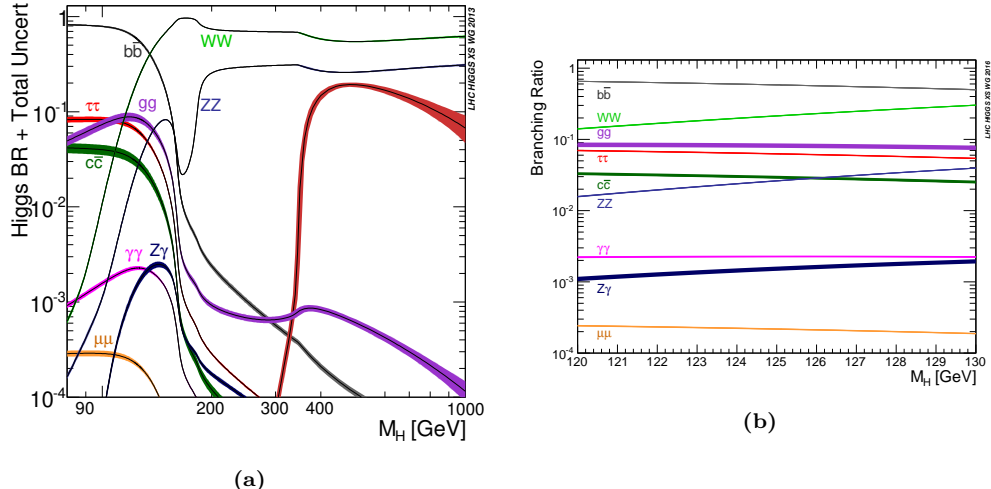


Figure 1.27: Standard Model Higgs boson decay branching ratios as function of m_H at $\sqrt{s} = 13$ TeV citeLHCIGGSSWG2013.

1.3.4 Higgs boson physics

Work in progress

The gauge symmetry is broken by the vacuum, triggering the EW Spontaneous Symmetry Breaking (SSB). This means that the symmetry group of the EW sector, $U(2)_L \otimes U(1)_Y$.

$$SU(3)_C \otimes SU(2)_L \otimes U(1)_Y \xrightarrow{\text{SSB}} SU(3)_C \otimes U(1)_{QED}$$

Production and decay rates, constrains on its couplings: <https://arxiv.org/abs/1606.02266>

The Higgs mass is given by $m_H = \sqrt{\lambda/2}v$, being v the vacuum expectation value of the Higgs field and λ the Higgs self-coupling.

Electro weak symmetry breaking [84]: <https://arxiv.org/pdf/1512.08749.pdf> In this paper the Yukawa coupling of the top is introduced, link it with the tHq paper.

Work in progress

1.4 Top quark and Higgs boson interplay

So far, the couplings of the Higgs boson to the SM particles have been found to be proportional to the mass of these particles. Since the top quark is the most massive particle and the coupling of Higgs to SM particles is

1125 uniquely determined by the mass of these particles, the Yukawa coupling
 1126 between the top quark and the Higgs boson (y_t) is expected to be the
 1127 greatest among all fermions and, hence, its study is of crucial importance,
 1128 as it is discussed in references [85][86] and developed in the succeeding
 1129 sections.

1130 The production of a pair or top quarks along with a Higgs boson ($t\bar{t}H$)
 1131 it is possible to measure the absolute value of y_t . This process has the
 1132 advantage of being the leading mechanism to produce the Higgs together
 1133 with the quark top. At $\sqrt{s} = 13$ TeV it has a cross section of **poner cálculos**
 1134 **del SM para $\sigma_{t\bar{t}H}$** (the definition of cross section can be found in Section
 1135 2.2.5).

1136 Despite having a very much lower cross section than $t\bar{t}H$ (**poner**
 1137 **números**), the Higgs boson production alongside a single top quark (tHq or
 1138 tH) brings valuable information, specially regarding the sign of the Yukawa
 1139 coupling. Note that the sign of y_t is not physical by itself but the relative
 1140 sign compared to the coupling of the Higgs to weak¹³ boson is, in deed,
 1141 physical [85]. This is explored with more detail in 1.4.2.

1142 A change in the Yukawa sign and/or absolute value with respect to its
 1143 SM value would signal an origin of the fermion masses different from the
 1144 described by the EWSB because the relative sign of the Higgs coupling to
 1145 fermions and gauge vector bosons is crucial for recovering the unitarity and
 1146 renormalizability of the theory s[87].

1147 **All section 1.4 is work in progress**

1148 $\rightarrow \mathcal{CP}$ Properties of Higgs Boson Interactions with Top Quarks in the
 1149 tH and $t\bar{t}H$ processes at ATLAS: <https://inspirehep.net/literature/1790698>
 1150

1151

1152 Only 1% of all Higgs bosons are produced in association with top quarks,
 1153 the observation of such processes is very challenging. Notably, it is a im-
 1154 mensely ambitious task to measure the associated production of a Higgs
 1155 with a single top which has an extremely low cross section as can be seen
 1156 in Figure 1.26b.

1157 **1.4.1 $t\bar{t}H$**

1158 The first associated production of a Higgs boson with a pair of top
 1159 quarks was observed in 2008 by ATLAS [88] and CMS [89]. This process
 1160 marked a significant milestone for the field of high-energy physics because

¹³The coupling of the Higgs to the gauge bosons is taken as positive.

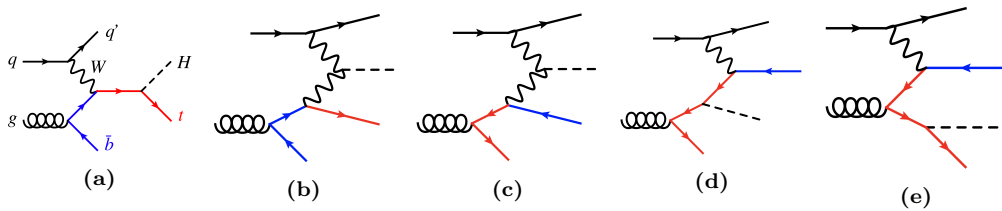


Figure 1.28: LO Feynman diagrams for t -channel tH production in the 4FS.

it helped establishing the first direct measurement of the tree-level coupling of the Higgs boson to the top quark, which interacted with the predicted strength.

The associated production of H with top quark pair has been studied by ATLAS and CMS previously during Run-1 at $\sqrt{s} = 7$ TeV and 8 TeV [90] [91] and Run-2 [buscar $t\bar{t}H$ en Run-2]

1.4.1.1 $t\bar{t}H$ Standard Model

1.4.1.2 $t\bar{t}H$ Charge-Parity

1.4.2 tHq

The tH production is divided in tHq and tWH .

tHq production modes

At LO, the production of a Higgs boson in association with a single top quark (tHq) in pp collisions is classified in three groups according to the virtuality of the W boson. These groups are: t -channel production, s -channel production and associated production with an on-shell W boson. This categorisation is the same as for the single-top-quark (Section 1.2.2.2), which makes sense since the tH associated production is, basically, a single-top-quark process in which a Higgs boson is radiated either from the W or the top.

In the t -channel production modes are classified in 4FS and 5FS as it is done for the single-top case. The 4FS and the 5FS modes are shown in Figures 1.28 and 1.28 respectively. For the 4FS modes, the diagrams in which the gluon decays to a top pair (1.28c, 1.28d and 1.28e) contribute less than the ones in which it does to a $b\bar{b}$ (1.28a and 1.28b).

Poner las tablas para las cross section de Demartin [92] para t -channel y s -channel

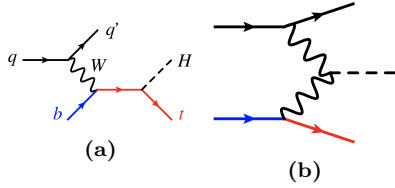


Figure 1.29: LO Feynman diagrams for t -channel tH production in the 5FS.

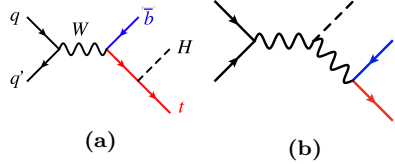


Figure 1.30: LO Feynman diagrams for s -channel tH production in the 5FS.

1187 Since the s -channel contribution is so small to the total cross section of
 1188 the tHq process,

1189 For tH and single-top-quark production at colliders, the 5FS calculations
 1190 are easier than the 4FS due to the lesser final state-multiplicity and simpler
 1191 phase space. This is why in the 5FS the single-top production is known
 1192 at NNLO while the 4FS this is done only for NLO. Another advantage of
 1193 the 5FS is that the t -channel, s -channel and associated tWH production do
 1194 not interfere until NNLO. Contrary, the in 4FS, the t -channel at NLO and
 1195 s -channel at NNLO can interfere. Nevertheless, this interferences are very
 1196 small and can be neglected [92].

1197 **Poner algo in información del tWH production mode para tH**
 1198 **y** The tWH production is a background in the tHq analysis.

1199 In reference 1.31 is shown that the shapes of the distributions of most
 1200 observables in the s -channel differ significantly from those of the t -channel.
 1201 So, even though the total cross section of the tHq production with the s -
 1202 channel is much more smaller than the one for t -channel, one could think
 1203 that including the s -channel in the analysis would increase the precision.
 1204 This is not the case because the LHC is not sensible for to the tHq produc-
 1205 tion via s -channel. In fact, not even the s -channel-single-top production
 1206 (without any associated Higgs boson) has been found at LHC.

1207 **Summarise production modes described in [92]**

tHq sensibility to y_t

As already commented in the introduction of the Section 1.4, the main interest of the tHq process is that it is among the few processes in the LHC that are sensible to the relative size and phase between the couplings of the

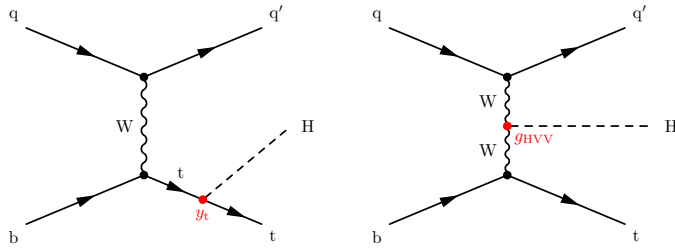


Figure 1.31: Representative LO Feynman diagrams for the t -channel tHq associated production, where the Higgs boson couples either to the top quark (left) or the W boson (right)

Higgs top and the Higgs to the gauge bosons. The other mechanisms to determine this relative sign are $H \rightarrow \gamma\gamma$ and $gg \rightarrow ZZ$. This is due to the fact that in the SM the tHq production where the H couples to the W (Figure 1.31 right) interfere destructively with those in which the H is radiated from the top (Figure 1.31 left). As it is later explained in Section 2.2.5, the cross section is proportional to the square of the matrix element, \mathcal{M} and if there are several diagrams for a same process, the matrix elements have to be summed before squaring leading to interference terms. For the tHq production

$$\sigma_{tHq} \propto |\mathcal{M}_{qq \rightarrow tHq}|^2 = |\mathcal{M}_{qq \rightarrow tHq_{WH}} + \mathcal{M}_{qq \rightarrow tHq_{tH}}|^2 \quad (1.40)$$

When squaring the scattering amplitude, the destructive interference¹⁴ term decreases the σ_{tHq} . This behaviour makes the tHq cross section exceptionally sensible to the departures of y_t from the SM predictions. Typically, the destructive interference yields a reduction in the rate as compared to the contribution from each individual diagram by about an order of magnitude [93]. Therefore, in the presence of non-SM new physics, a positive relative sign between the tH and the WH couplings would imply that the amount of tHq events recorded should increase a factor of ~ 13 over the SM expectations, surpassing the $t\bar{t}H$ production [94].

The tHq production has been studied at LHC Run-1 by CMS [39]

Usar los papers the tHq de CMS la sección 5 de Demartin [92]

¹⁴By destructive interference is meant that the relative sign between $\mathcal{M}_{qq \rightarrow tHq_{WH}}$ and $\mathcal{M}_{qq \rightarrow tHq_{tH}}$ is negative.

1219 **1.4.2.1 tH Standard Model**

1220 **1.4.2.2 tH Charge-Parity**

1221 **1.4.2.3 ATLAS and CMS results**

1222 In order to gather the necessary information, the widest possible cam-
1223 paign of measurements has to be undertaken, including all the different
1224 Higgs decay modes. In this context, the scope of this thesis is the study of
1225 the production tH with a final state characterised by two light leptons (ℓ),
1226 i.e. electrons (e^\pm) or muons (μ^\pm), and one hadronically decaying tau lepton
1227 (τ_{had}). This signature is usually referred as dileptau or lep-had channel and
1228 is denoted by $2\ell + 1\tau_{\text{had}}$.

₁₂₂₉ **Chapter 2**

₁₂₃₀ **The ATLAS experiment at the
1231 Large Hadron Collider of
1232 CERN laboratory**

₁₂₃₃ The work developed in this thesis is framed in the context of the ATLAS
₁₂₃₄ detector, a general-purpose particle physics detector registering the events
₁₂₃₅ originated from the collisions produced by the largest and most powerful
₁₂₃₆ particle accelerator built up to this date, the LHC. This experimental setup
₁₂₃₇ is located in one of the largest and most renowned centres for scientific
₁₂₃₈ research in the world, the CERN.

₁₂₃₉ This chapter is devoted to the introduction of the CERN laboratory and
₁₂₄₀ a description of the technical design of LHC and ATLAS. The CERN or-
₁₂₄₁ ganisation is presented through an overview of its history, its achievements
₁₂₄₂ and some of the most relevant research projects carried out currently. The
₁₂₄₃ essential technical aspects of the LHC machine design are covered. The
₁₂₄₄ distribution and functioning of the accelerator complex and the main exper-
₁₂₄₅ iments conducted at LHC are summarised as well. Finally, a full overview
₁₂₄₆ of the different components of the ATLAS detector is exposed, presenting
₁₂₄₇ the specific features of each of its parts.

₁₂₄₈ **2.1 CERN**

₁₂₄₉ The European Organization for Nuclear Research, known as CERN, is
₁₂₅₀ the largest particle physics laboratory in the world. The convention estab-
₁₂₅₁ lishing CERN was ratified in 1954. Its name is derived from the French
₁₂₅₂ acronym *Conseil Européen pour la Recherche Nucléaire*, which was the pro-
₁₂₅₃ visional body designated in 1952 to foster the fundamental physics research

in Europe, and the acronym has been maintained until CERN’s foundation. Initially formed by 12 member states, now it has 23 member states and many non-European countries involved in different ways such as associate members, partners and observers [95].

The main site of the laboratory is located at Meyrin, a municipality of the Canton of Geneva (Switzerland), at the Franco–Swiss border. There are other sites in the vicinity of the Meyrin site, being the most relevant the Prévessin Site, the CERN’s second-largest site, straddling the communes of Prévessin-Moën (France).

Since its beginning, CERN’s objective has been helping to uncover what the universe is made of and how it works. CERN started its first accelerator, the Synchrocyclotron, on 1957 and rapidly observed the electron decay of the pion for the very first time [96]. Thereafter, the laboratory has continued contributing to not only particle and nuclear physics but also more technical fields. For instance, one of the most important achievements made through CERN experiments is the discovery in 1973 of neutral currents in the Gargamelle bubble chamber installed in the Proton Synchrotron (PS) [97]. This observation was an indirect evidence for the existence of the Z boson and ten years later, in 1983, CERN announced the discovery of the Z and W bosons [98]. This finding was done at the UA1 and UA2 experiments, located within the Super Proton Synchrotron (SPS), and it was awarded with the laboratory first Nobel Prize in 1984. Other major successes of CERN were the determination of the number of light neutrino families at the Large Electron-Positron Collider (LEP) on 1995 [99] and the creation for the very first time of antihydrogen atoms in 1995 at the PS210 experiment [100]. More crucial accomplishment followed such as the discovery during the 1990’s of \mathcal{CP} violation by NA31 [101] and NA48 experiments [102]. And, in 2012, the Higgs boson discovery by ATLAS and CMS[78] [79], a fundamental test for the robustness of the SM as described in Section 1.3.1. More recently, in 2015, a state consistent with a pentaquark was observed at LHCb [103].

Currently, a wide diversity of projects are carried at CERN being the most renowned of them the LHC and its experiments which are described in more detail in Section 2.2. In addition, fixed-target experiments, antimatter experiments and experimental facilities make use of the LHC injector chain. The main fixed-target experiments at CERN are the Antiproton Decelerator (AD) [104] for slowing antiprotons for the antimatter factory [105] and the On-Line Isotope Mass Separator (ISOLDE) facility for short-lived ions [106]. The world’s first proton-driven plasma wakefield acceleration experiment is also at CERN, the Advanced Proton Driven Plasma Wakefield Acceleration Experiment (AWAKE) [107]. In the International Space Station (ISS), the

1295 Alpha Magnetic Spectrometer (AMS) tries to observe dark matter [108].
1296 The research programme at CERN covers topics from the basic structure
1297 of matter to cosmic rays, and from the Standard Model to supersymmetry.

1298 Important breakthroughs and advances have been done by CERN on
1299 three main technical fields: accelerators, detectors and computing. Behind
1300 these three areas of technology, lies a great number of topics of expertise:
1301 cryogenics, ultra-high vacuums, particle tracking, radiation monitoring, su-
1302 perconductivity, plasma-physics and many more. Probably, the most pop-
1303 ular of the contributions is the invention of the World Wide Web (WWW)
1304 in 1989 at CERN facilities [109]. All of this proves the versatility and cap-
1305 ability of CERN as a contributor to science, technology and society.

1306 2.2 Large Hadron Collider

1307 In the mid of the decade of 1980, the plans for building the Large Hadron
1308 Collider (LHC) were started. At several high-energy physics workshops
1309 and conferences, the idea of assembling a machine able to reach multi-TeV
1310 energies was discussed. This instrument would allow physicists to search for
1311 the Higgs boson at all possible masses. In 1991 the Long-Range Planning
1312 Committee of CERN proposed the construction of the LHC as the best step
1313 forward in CERN's future [110]. The approval of the LHC project arrived
1314 in 1994 and in 1995 the Conceptual Design Report was published [111].
1315 Finally, on 10 September 2008, a beam of protons was successfully directed
1316 into the LHC pipes for the first time.

1317 A summary of the main parameters of LHC for pp collisions is pre-
1318 sented in Table 2.1. These parameters are shown for how the machine was
1319 designed, for Run-1 (2011-2012) and Run-2 (2015-2018) as well as the ex-
1320 pected parameters for Run-3 (2025-2027). The forecasted values for the
1321 High Luminosity (HL) LHC upgrade (after 2027) are exposed too.

1322 2.2.1 Machine design

1323 The LHC is a circular hadron accelerator with a circumference of 27 km.
1324 Located where once was the LEP collider, the accelerator used by CERN
1325 from 1999 to 2000 [112], the LHC tunnels are almost entirely outside the
1326 main site, being mainly on french territory. An overall schematic view of
1327 the LHC is shown in Figure 2.1.

1328 The LHC has two rings with ultra-high vacuum (to prevent collisions
1329 with gas molecules while moving through the accelerator) inside of which

Parameter	Design	Run-1	Run-2	Run-3	HL-LHC
Beam energy	7	3.5 - 4	6.5	7	7
Center-of-mass energy (\sqrt{s}) [TeV]	14	7 - 8	13	14	14
Bunch spacing [ns]	25	50	25	25	25
Bunch Intensity [10^{11} ppb]	1.15	1.6	1.2	up to 1.8	2.2
Number of bunches (n_b)	2800	1400	2500	2800	2800
Transverse emittance (ϵ) [μm]	3.5	2.2	2.2	2.5	2.5
Amplitude function at the interaction point (β^*) [cm]	55	80	30→25	30→25	down to 15
Crossing angle [μrad]	285	-	300→260	300→260	TBD
Peak Luminosity [$10^{34} \text{ cm}^2 \text{ s}^{-1}$]	1.0	0.8	2.0	2.0	5.0
Peak pileup	25	45	60	55	150
Nominal magnetic field (B) [T]	8.73	4.16 - 7.76	7.73	8.73	8.73
Injection energy [GeV]				450	
Circumference length [km]				26.7	
Radius [km]				4.24	
Number of dipole magnets				1232	
Length of dipole magnets [m]				14.3	
Number of quadrupole magnets				395	
Total mass [tons]				27.5	

Table 2.1: Summary of main accelerator parameters for the LHC, showing the design values, and those used during Run-1 and Run-2, as well as the expected parameters for Run-3 and the HL-LHC.

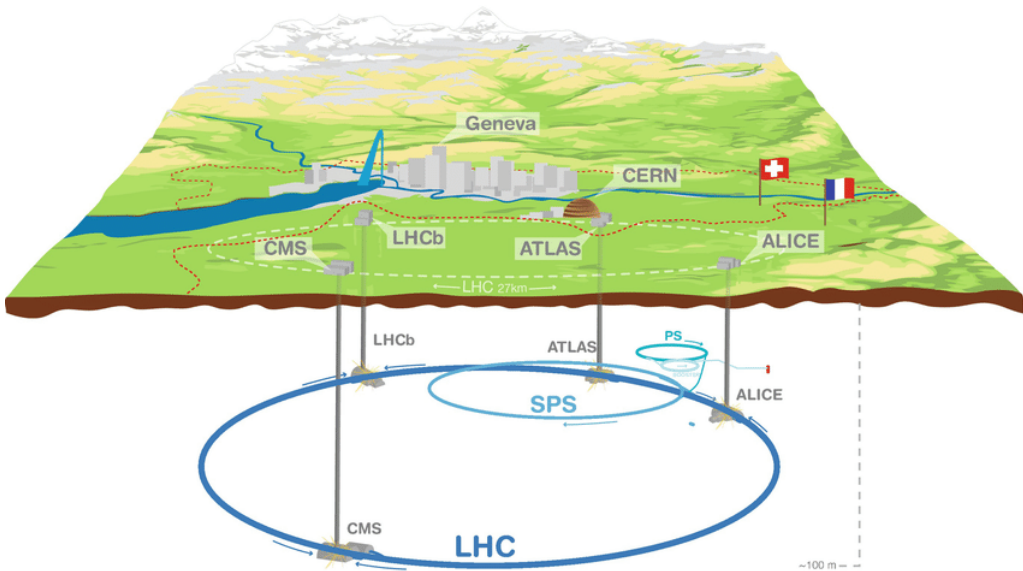


Figure 2.1: Overall view of the LHC including the ATLAS, CMS, ALICE and LHCb experiments.

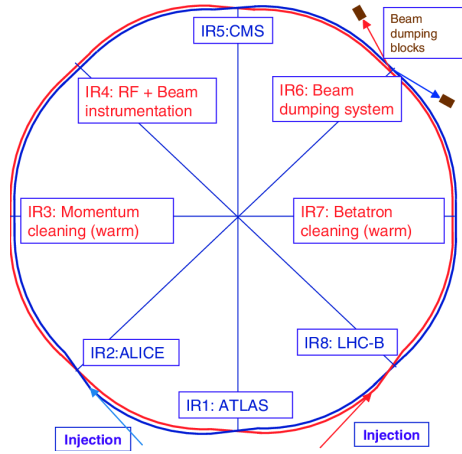


Figure 2.2: Schematic layout of the LHC (Beam 1 clockwise, Beam 2 anti-clockwise).

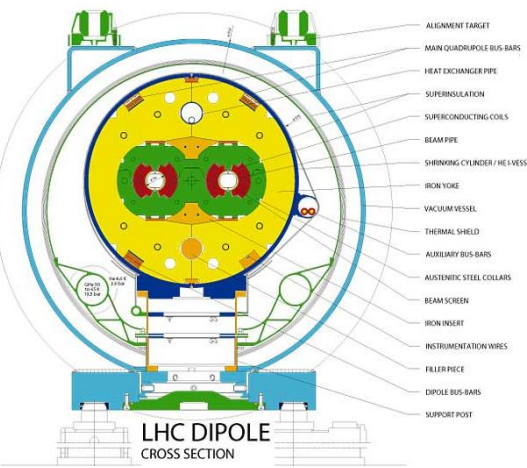


Figure 2.3: LHC dipole cross section.

1330 particle beams travelling in opposite directions. It was designed to accelerate and collide proton beams with a center-of-mass energy (\sqrt{s}) up to
 1331 14 TeV at a luminosity (\mathcal{L}) of $10^{34} \text{ cm}^2 \text{ s}^{-1}$ (see Section 2.2.5 for details
 1332 about luminosity). As well as protons, it can collide heavy ions, in partic-
 1333 ular lead nuclei, at $\sqrt{s} = 2.3 \text{ TeV}$ per nucleon and a peak luminosity of $\mathcal{L} = 10^{27} \text{ cm}^2 \text{ s}^{-1}$ [113]. These specifications make the LHC the accelerator
 1334 with higher collision energy [114].
 1335

1337 The beams in the LHC are made up of bunches of protons that are
 1338 spaced 7 m apart and collide every 25 ns. Each bunch contains 1.1×10^{11}
 1339 hadrons, being 2556 the maximum possible number of bunches that can be
 1340 reached with the beam preparation method currently used [115]. The size
 1341 of each bunch is 25 cm [116].
 1342

The LEP tunnel lies between 45 m and 170 m below the surface on a plane inclined at 1.4% sloping towards the Léman lake. The underground construction adds some shielding from outside interferences that could interact with the detectors and cause anomalous readings. Even 100 m underground, the cosmic rays can reach the detectors, so these are used to help to calibrate them. The tunnel has an internal diameter of 3.7 m, which makes it extremely difficult to install two completely separate proton rings [117] as in the Superconducting Super Collider (SSC). Therefore, the counter-rotating rings are built under the *two-in-one* twin-bore superconducting magnet design. These twin bore configurations have the disadvantage of having the rings magnetically coupled, which adversely affects flexibility [118]. Figure 2.3 shows an example of the LHC twin-bore dipole magnet.
 1343
 1344
 1345
 1346
 1347
 1348
 1349
 1350
 1351
 1352
 1353

1354 The LHC is not a perfect circle. Approximately 22 km of the LHC ring
1355 consists of 8 curved sections. The remaining 5 km of the tunnel are made of 8
1356 straight sections, denominated insertion regions (IR), that provide space for
1357 the experiments. Figure 2.2 shows the distribution of IR and crossing points
1358 for the LHC. This layout follows that of the LEP tunnel. The number of
1359 crossing points where the beams pass from one ring to the other for colliding
1360 was decreased from the original 8 at LEP to 4 in the LHC in order to reduce
1361 costs and optimise the utility insertions containing Radio Frequency (RF),
1362 the collimation and the beam dump systems [111].

1363 The arcs contain the dipole bending magnets, which are shown in Section
1364 2.3. The 1232 twin-bore magnets curve the trajectory of the particle beam
1365 that would, otherwise, follow a straight line. Dipoles are also equipped with
1366 additional multipole lattice magnets (sextupole, octupole and decapole),
1367 which correct for small imperfections in the magnetic field at the extremities
1368 of the dipoles.

1369 Each of the 8 straight sections is approximately 528 m long. The RF
1370 cavities delivering 2 MV (an accelerating field of 5 MV/m) at 400 MHz are
1371 located in the IR4. The 16 RF cavities compensate the synchrotron radi-
1372 ation losses (the electromagnetic radiation emitted when charged particles
1373 travel in curved paths) that take place at the arcs of LHC. The energy ra-
1374 diated per particle by synchrotron radiation is proportional to the inverse
1375 of the mass of the particle: $\Delta E \propto 1/m^4$. This radiation is, thus, smaller
1376 for protons than for electrons. That is why the LHC machine has much less
1377 synchrotron radiation losses than LEP and its design would ideally have
1378 longer arcs and shorter straight sections for the same circumference. But
1379 using the tunnel as built for LEP was the cost-effective solution. During
1380 the 20 minutes that are needed to reach the beams maximum energy, the
1381 bunches have passed the RF cavities more than 10 million times [111].

1382 The RF cavities (also known as resonators) are metallic chambers spaced
1383 at intervals along the accelerator shaped to resonate at specific frequencies,
1384 allowing radio waves to interact with passing particle bunches. The main
1385 role of the RF cavities is to keep the proton bunches tightly packed to
1386 ensure the required luminosity at the interaction point. They also transfer
1387 RF power to the beam to accelerate it to the top energy [119].

1388 At the insertion of the arc and straight sections, quadrupole magnets
1389 are installed to suppress the dispersion of particles. Acting as focal lenses,
1390 quadrupole magnets gather the particles together. This system not only
1391 cancels the horizontal dispersion arising in the arc but also adapts the LHC
1392 reference orbit to the geometry of the LEP tunnel. Before entering the
1393 detectors, the inner triplets (which are made mostly from quadrupoles)

1394 tighten the beam, from 0.2×10^{-3} m down to 16×10^{-6} m. These are known
1395 as insertion magnets.

1396 In total there are more than 9000 magnets all over the LHC and more
1397 than 50 types of magnets are needed to make the particles circulate in
1398 their path without losing speed. The coils are made of niobium-titanium
1399 (NbTi) which is cooled to less than 2 K with superfluid helium to reach
1400 superconductivity.

Of course, only stable charge particles¹ such as electrons, positrons, protons, antiprotons and some ions, can be accelerated by the magnetic fields described. The force that experiments a charged particle with charge q moving under a magnetic field B at a speed v is given by Lorentz law

$$\vec{F} = q \vec{v} \times \vec{B} \quad (2.1)$$

1401 and, since \vec{B} is perpendicular to \vec{v} , this force is always directed to the
1402 center of the circle of radius r : $F = Bqv = m\frac{v^2}{r}$.

1403 2.2.2 Accelerator complex

1404 To accelerate the proton beams, the existing CERN accelerator complex
1405 is used. These accelerators were, back in the day, the state of the art
1406 colliders and now they serve as injection system for the LHC. The path
1407 followed by the particle beams is presented in Figure 2.4. The accelerator
1408 complex consists in several machines interconnected with higher and higher
1409 capabilities, i.e. the beams are injected from one accelerator to the next in
1410 sequence, boosting the particles to higher energies in each step until they
1411 enter into the LHC.

1412 The proton bunches are produced ionising a gas of hydrogen atoms and
1413 then they are accelerated to a momentum of 50 MeV by the linear accelerator
1414 (LINAC2). Starting from Run-3, the LINAC2 is being replaced by the
1415 LINAC4. After being produced, the beams enter into the first circular
1416 accelerator, the Proton Synchrotron Booster (PSB) which has 630 m radius
1417 and increases the energy of the protons until 1.4 GeV.

1418 The main advantage of circular accelerators compared to linear ones is
1419 that they can speed up particles with much less physical space. Circular
1420 accelerators ramp up two different beams with opposite charges at the same
1421 time with a single magnetic field. The maximum energy transferred to the
1422 beams in a circular accelerator is given by p_T [GeV] = $0.3qB[T]r[m]$, being

¹Long-lived particles such as the muon ($\tau \approx 2 \times 10^{-6}$ s) are discussed to be used on a muon collider [120].

1423 p_T the transverse momentum of the particles, q the charge of the particles
1424 ($q = 1$ for protons), B the magnetic field applied and r the radius of the
1425 circular accelerator.

1426 Right after the PSB, the Proton Synchrotron brings the particles 25 GeV.
1427 The next step in the chain raises the energy to 450 GeV. This is done by the
1428 SPS, which is 6.9 km long. Once the protons have 450 GeV, the minimum
1429 energy at which the LHC can maintain a stable beam, they are injected
1430 into the LHC by two different 2 km-long Transfer Injection (TI) lines [121].
1431 Protons will circulate in the LHC for 20 minutes until reaching the maximum
1432 speed and energy (650 GeV per beam) [118].

1433 Heavy-ion collisions were included in the conceptual design of the LHC
1434 from an early stage. Lead ions for the LHC are extracted from a source
1435 of vaporised lead and enter LINAC3 before being collected and accelerated
1436 in the Low Energy Ion Ring (LEIR). They, then, follow the same route to
1437 maximum acceleration as the protons [118].

1438 2.2.3 LHC Experiments

1439 In the LHC four major experiments are carried, each of them with its own
1440 detector (Figure 2.5). These particle detectors measure particles produced
1441 as debris from the pp collisions through the interaction with the material
1442 of the sub-detectors. Distributed along the collider as is shown in Figures
1443 2.1, 2.2 and 2.4, these highly sophisticated experiments are:

- 1444 • **A Toroidal LHC ApparatuS (ATLAS)** [122]: Located in the IR1,
1445 it is a generic multi-purpose experiment for high luminosity (up to \mathcal{L}
1446 = $10^{34} \text{ cm}^2 \text{ s}^{-1}$). It studies proton-proton collisions and investigates
1447 a wide range of physics, from the search for extra dimensions to dark
1448 matter. It has the dimensions of a cylinder, 46 m long, 25 m in dia-
1449 meter. The ATLAS detector weighs 7×10^3 tonnes. The design of the
1450 ATLAS detector features excellent jet and E_T^{miss} resolution, particle
1451 identification and flavour tagging and standalone muon measurements.
1452 ATLAS will be covered in detail in Section 2.3.
- 1453 • **Compact Muon Solenoid (CMS)** [123]: Built inside the IR5, it's
1454 the other general-purpose experiment for high luminosity (same \mathcal{L} as
1455 ATLAS). CMS has the same objectives and goals as ATLAS but both
1456 its hardware and software designs are different. Even though CMS is
1457 smaller than ATLAS (21 m long, 15 m in diameter) it is much heavier,
1458 weighting 14×10^3 tonnes. The bulk of its weight is the steel yoke that
1459 confines the 4 T magnetic field of its superconducting solenoid. The

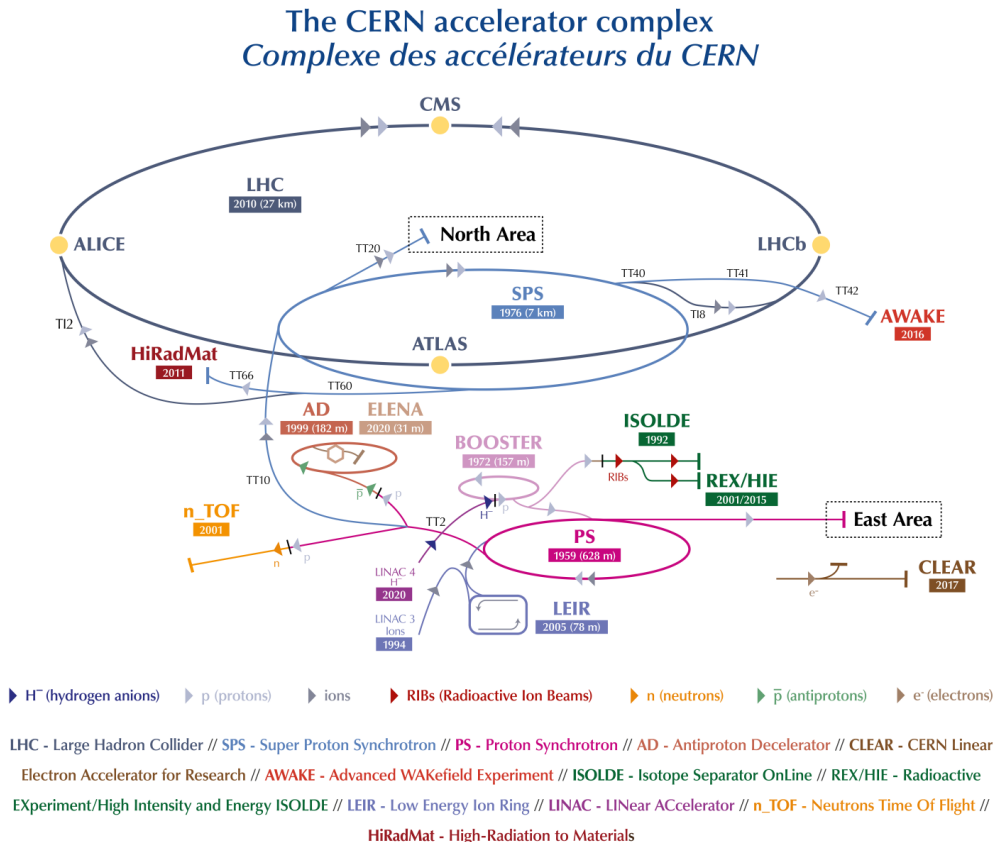


Figure 2.4: Scheme of CERN accelerator complex. Protons are injected from the LINAC2 into the PS Booster, then the PS, followed by the SPS, before finally reaching the LHC.

design of CMS emphasises magnificent electron/photon energy and momentum resolution. The role of coexistence of CMS and ATLAS is fundamental so that one can verify and confirm the experiments of the other independently.

- **Large Hadron Collider beauty (LHCb)** [124]: Hosted at IR2, it is a lower luminosity experiment designed to study the small asymmetries between matter and antimatter through \mathcal{CP} violation using rare decays of b -quark based hadrons. The detector is arranged as a succession of planar sub-detectors since most of the b -flavoured mesons follow the beam pipe direction when created in the proton-proton collision. LHCb delivers remarkable low-momentum track reconstruction and particle identification.
- **A Large Ion Collider Experiment (ALICE)** [125]: It is a low luminosity experiment in IR8 that focuses on QCD, the strong-

1474 interaction sector of the SM. The main feature of ALICE is a general-
 1475 purpose detector that it uses heavy-ion collisions to study matter in-
 1476 teracting at extreme densities and temperatures, thus reproducing the
 1477 quark-gluon plasma. This detector provides highly efficient track re-
 1478 construction in an environment full of heavy ions. Besides running
 1479 with Pb ions, the physics programme includes collisions with lighter
 1480 ions, lower energy collisions and a dedicated proton-nucleus run.

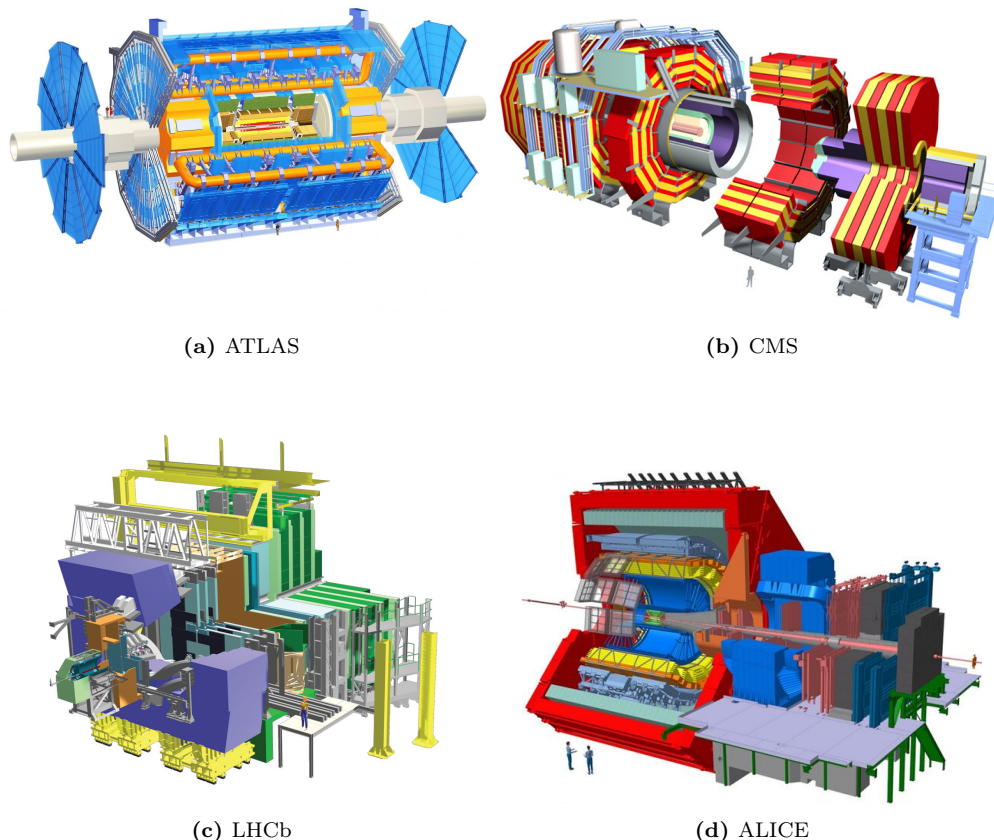


Figure 2.5: Scheme of LHC main experiments. Note that the images are not equally scaled.

1481 Along the LHC machine, there are other experiments much more smaller
 1482 than ATLAS, CMS, LHCb and ALICE, typically sharing the cavern with
 1483 the major projects. The most relevant among the minor experiments are:

- 1484 • **The Large Hadron Collider forward (LHCf)** [126]: Uses
 1485 particles thrown forward by collisions in the Large Hadron Collider
 1486 as a source to simulate cosmic rays in laboratory conditions. It shares
 1487 its cavern with the ATLAS detector [127].

- **The Massive Timing Hodoscope for Ultra Stable neutrAL pArticles (MATHUSLA)** [128]: Is dedicated large-volume displaced vertex detector for the HL-LHC on the surface above ATLAS or CMS for the search for neutral long-lived particles.
- **MilliQan** [129][130]: Consists on a small-scale detector experiment aiming to detect millicharged particles, i.e., particles with charges much smaller than that of the electron.
- **Monopole and exotic particle detector at the LHC (MoEDAL)** [131]: Deployed at LHCb cavern, it is optimised to detect highly ionising particles such as magnetic monopoles, dyons and multiple-electrically charged stable massive particles predicted in a number of theoretical scenarios.
- **TOTEM** [132]: Aims to measure the total cross-section of $p\bar{p}$ interaction using a luminosity-independent method and study elastic and diffractive scattering at the LHC. As CERN longest experiment, TOTEM detectors are spread across almost half a kilometre around the CMS interaction point.
- **ForwArd Search ExpeRiment (FASER)** [133][134]: Designed to search for new, yet undiscovered, light and weakly-interacting particles and study the interactions of high-energy neutrinos.

2.2.4 LHC Computing grid

The data collected by the different LHC experiments is stored, processed and, then, made available for all the researchers of each collaboration². This is possible thanks to the last piece of the LHC, its computing model and infrastructure: the LHC Computing Grid (LCG). It consists of several computing farms distributed around the world and interconnected. Figure 2.6 shows the geographical distribution of the different facilities that comprise the LCG. Just as the WWW enables access to information, the Grid enables access to computer resources. Employing a grid certificate, is possible for any user to run jobs on the grid and to access the data stored. The implementation of the grid model implies an effective coordination among all LHC collaboration centres [135].

Different types of computing centres have been defined and classified in Tiers [137]:

²Within the grid context, each collaboration is known as Virtual Organisation (VO).



Figure 2.6: Worldwide LHC Computing Grid geolocalisation of sites [136].

- **Tier-0:** This facility is located at CERN and it is responsible for archiving (first copy) and distributing the raw data received from the Event Filter, i.e., the data emerging from the Data Acquisition systems (DAQ) after the trigger. It provides prompt reconstruction and distributes a copy of the raw data to the Tier-1 centres.
- **Tier-1:** These facilities archive the raw data permanently and provide the computational capacity for reprocessing and for physical analysis. It also stores the simulated and reprocessed data. Currently, there are thirteen large computer centres serving as Tier-1 (see Figure 2.7). These make data available to their Tier-2 centres [138].
- **Tier-2:** Typically located at universities and other scientific institutes, there are more than 150 Tier-2 sites. The derived datasets produced by the physics groups are copied to the Tier-2 facilities for further analysis. The MC simulations for event production are executed at this level.
- **Tier-3:** The local computing resources, from local clusters to even just an individual PC are referred to as Tier-3. There is no formal engagement between worldwide LCG and the Tier-3.

This system provides near real-time access to LHC data. The LCG collaboration spreads out over 42 countries with 170 computing centres and 1 million computer cores, being the world's largest computer grid. It deals with over two million tasks daily. These specifications make the LCG the most sophisticated system for data taking and analysis ever built for science.

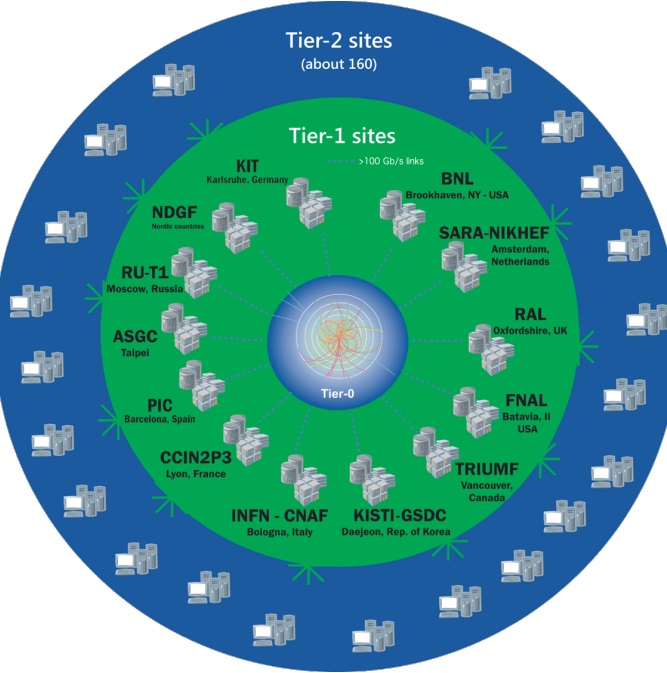


Figure 2.7: LCG Tiers [138].

1545 2.2.5 Energy, Luminosity and Cross-section

1546 Energy

1547 Another name to refer to the field of Particle Physics is “high energy phys-
 1548 ics”. Particles such as the Higgs boson or the top quark are more than 100
 1549 times heavier than the proton so, in order to produce them, huge energies
 1550 are required. The energy of the interaction, \sqrt{s} , allows the production of
 1551 physical effects. The greater the energy is, the bigger is the range of the
 1552 different processes that can be produced by the accelerator.

The four-vector, $\mathbf{p} = (E, \vec{p})$, of a particle of mass m describes its kinematics with its energy E and \vec{p} . The square of the four-vector, \mathbf{p}^2 , corresponds to the particle mass:

$$\mathbf{p}^2 = E^2 - \vec{p}^2 = m^2 \quad (2.2)$$

When two particles of mass m_1 and m_2 and momenta \vec{p}_1 and \vec{p}_2 respectively collide, the center of mass energy, \sqrt{s} , can be expressed as:

$$s = E_{CM}^2 = (\mathbf{p}_1 + \mathbf{p}_2)^2 = (E_1 + E_2)^2 - (\vec{p}_1 + \vec{p}_2)^2 \quad (2.3)$$

For symmetric colliding beams, such those of LHC, the collision point is at rest in the laboratory frame ($\vec{p}_1 = -\vec{p}_2$) and, hence, the energy is

$$s = E_{CM}^2 = (E_1 + E_2)^2 \quad (2.4)$$

1553 Since the energy of each beam is 650 GeV during Run-2, the center of mass
 1554 energy of LHC collisions is

$$\sqrt{s} = E_{CM} = (E_{beam1} + E_{beam2}) = 650 \text{ GeV} + 650 \text{ GeV} = 13 \text{ TeV} \quad (2.5)$$

When LHC is used for fix target experiments, one of the particles in the collision is at rest ($\vec{p}_2 = 0$) and the equation 2.3 writes as:

$$E_{CM}^2 = (m_1^2 + m_2^2 + 2m_2 E_{1,lab}) \quad (2.6)$$

Then, the energy for a proton-proton fix target collision with one beam at 650 GeV is

$$\begin{aligned} E_{CM}^2 &= (m_p^2 + m_p^2 + 2m_p E_{beam}) \\ &= 2(0.938 \text{ GeV})^2 + 2 \cdot 0.938 \text{ GeV} \cdot 650 \text{ GeV} = 1221.2 \text{ GeV}^2 \\ E_{CM} &= 34.9 \text{ GeV} \end{aligned} \quad (2.7)$$

1555 This shows why colliding beams are essential to achieve high center of mass
 1556 energies.

1557 **Luminosity**

1558 Besides \sqrt{s} , the luminosity is the most relevant parameter in an experiment,
 1559 especially in searches for events with small cross-section. It measures the
 1560 ability of the particle accelerator to produce enough events of the desired
 1561 type.

The luminosity, \mathcal{L} , is the ratio of events detected in a certain period of time for a given cross-section (σ):

$$\mathcal{L} = \frac{1}{\sigma} \frac{dN}{dt} = \frac{1}{\sigma} R \quad (2.8)$$

1562 where N is the number of the events and t the time. $R = \frac{dN}{dt}$ is known as
 1563 reaction rate. It can be understood as number of particle collision per unit
 1564 area (typically expressed in cm^2) and per second, therefore it is measured in
 1565 $\text{cm}^2 \text{s}^{-1}$ [139]. For instance, for LEP was $\mathcal{L}_{LEP} = 1.0 \times 10^{32} \text{ cm}^2 \text{s}^{-1}$ and
 1566 the LHC is designed to achieve $\mathcal{L}_{LHC_{pp}} = 2.1 \times 10^{34} \text{ cm}^2 \text{s}^{-1}$ in pp collisions
 1567 and $\mathcal{L}_{LHC_{PbPb}} = 6.1 \times 10^{27} \text{ cm}^2 \text{s}^{-1}$ for heavy ion collisions.

For two beams colliding, the instantaneous luminosity is proportional to the number of bunches per beam (n_1 and n_2), the revolution frequency (f) with which the bunches are crossing and the number of proton bunches in

the machine (n_b), and it is and inversely proportional to the beams effective transverse area in which the collision takes places (Area = $4\pi\sigma_x\sigma_y$)

$$\mathcal{L} = f \cdot \frac{n_1 n_2 n_b}{4\pi\sigma_x\sigma_y} \cdot F(\theta_c, \sigma_x, \sigma_z) \quad (2.9)$$

where $F(\theta_c, \sigma_x, \sigma_z)$ is a factor accounting for the luminosity reduction due to the beam crossing angle (θ_c). At the LHC, assuming that the particles travel at the speed of light, for its 27 km, the bunch crossing frequency is $f = 11245.5$ Hz. The maximum number of proton bunches in the machine with 25 ns slots is³ $n_b = 2808$. In each bunch there are $n_1 \approx n_2 \approx 1.15 \times 10^{11}$ particles. Finally, characterising the optics of the collision at the interaction point (IP), the RMS transverse beam width in the horizontal and vertical directions are $\sigma_x \approx \sigma_y \approx 12, \dots, 50 \mu m$. The expression 2.9 assumes that the particles in the beam are Gaussian distributed. According to equation 2.9 the instantaneous luminosity only depends on the machine and its beam parameters [140][141].

The integrated luminosity over time is given by

$$L = \int \mathcal{L} dt \quad (2.10)$$

and it is used to determine the number of events, N , that have taken place during that time: $N = \sigma \times L$. The ability to observe low cross-section events is

$$N_{events}^{obs} = \sigma_{process} \times \text{efficiency} \times L \quad (2.11)$$

, where the efficiency of the detection is to be optimised by the experimental physicist, the integrated luminosity (L) is delivered by LHC and the cross-section of the process ($\sigma_{process}$) is given by nature.

On one hand, several factors can limit the maximum luminosity that can be achieved at LHC [139]:

- **Beam-beam effect:** The bunches of two beams or the particles in the same bunch can interact electromagnetically, this leads to distortions from the orbit and results in an increase of the emittance, ϵ .
- **Crossing angle:** Often used to avoid unwanted collisions in machines with many bunches, due to the crossing angle θ_c , the luminosity is reduced by a factor $F(\theta_c, \sigma_x, \sigma_z) = \sqrt{1 + (\theta_c \sigma_z / 2\sigma x)^2}$.
- **Beam offset:** Originated from the beam-beam effects or misalignments in the quadrupole magnets, the beams can collide with small

³The theoretical maximum of 3564 bunches cannot be reached due to space needed between bunch trains and for the beam dump kicker magnets.

Year	2015	2016	2017	2018
Peak instantaneous luminosity ($\times 10^{33} \text{ cm}^2 \text{ s}^{-1}$)	5	13	16	19
Total delivered integrated luminosity (fb^{-1})	4.0	38.5	50.2	63.4

Table 2.2: Peak luminosity and total integrated luminosity delivered by the LHC at $\sqrt{s} = 13 \text{ TeV}$ in Run-2 per year [143].

1592 transverse offset. Such beams' offsets induce a loss of \mathcal{L} at the inter-
 1593 action point.

- 1594 • **Hourglass effect:** Appears when beams collide in a point away from
 1595 the IP.

1596 On the other hand, there are diverse strategies to maximise the lumin-
 1597 osity delivered by a machine [140]:

- 1598 • **Maximise the total beam current:** Improvements in beam col-
 1599 limitation, cryogenics vacuum and background protection could extend
 1600 the limit on the maximum beam current.
- 1601 • **Compensate reduction factor:** The hourglass effect may be re-
 1602 duced by shorter bunches at the expense of a higher longitudinal pileup
 1603 density (see Section 2.2.6).

1604 The cumulative luminosity delivered by LHC to ATLAS during the Run-
 1605 2 per year is shown in Figure 2.8. In Figure 2.9, the total Run-2 cumulative
 1606 luminosity is presented differentiating between the delivered and recorded
 1607 luminosity and showing that almost all delivered events are considered to
 1608 be good data quality. The delivered luminosity accounts for the luminosity
 1609 given from the start of stable beams until the LHC requests ATLAS to
 1610 put the detector in a safe standby mode to allow a beam dump or beam
 1611 studies. The recorded luminosity reflects the DAQ inefficiency, as well as
 1612 the inefficiency of the so-called “warm start”: when the stable beam flag is
 1613 raised, the tracking detectors undergo a ramp of the high-voltage and, for
 1614 the pixel system, turning on the preamplifiers. The All Good Data Quality
 1615 criteria require all reconstructed physics objects to be of good data quality
 1616 [142].

1617 **Cross-section**

1618 The cross-section is a metric of the likely is a particular reaction to occur.
 1619 The higher the cross section is for a process, the more probable is for it to
 1620 take place. Denoted by σ , it is measured in units of area named barns: 1
 1621 barn = $b = 10^{-24} \text{ cm}^2$. For instance, for the LHC energy:

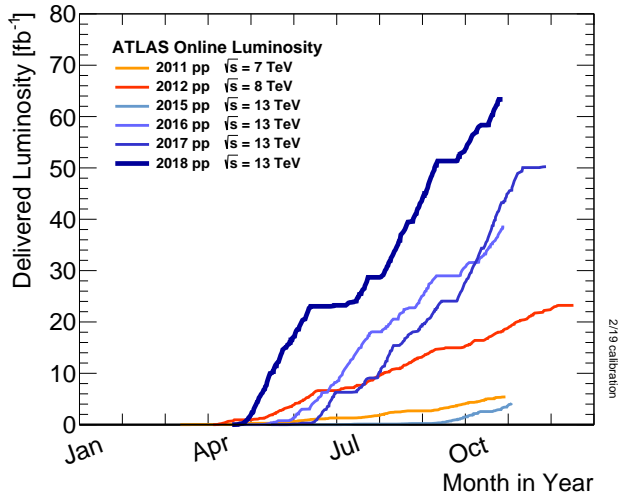


Figure 2.8: Cumulative luminosity versus day delivered to ATLAS during stable beams and for high energy pp collisions.

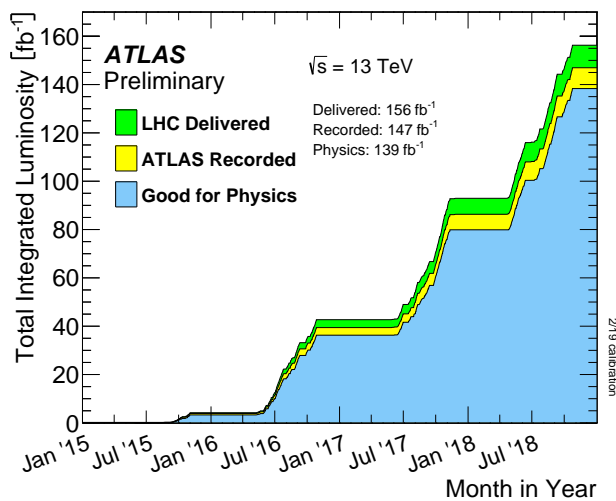
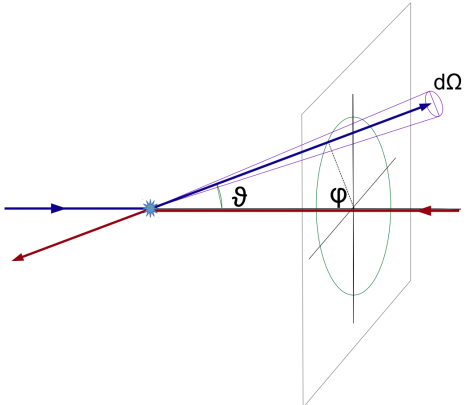


Figure 2.9: Total cumulative luminosity versus time delivered to ATLAS (green), recorded by ATLAS (yellow) and certified to be good quality data (blue) during stable beams for pp collisions at $\sqrt{s} = 13 \text{ TeV}$.

- 1622 • $\sigma(pp \rightarrow X) \approx 0.1 \text{ b}$
- 1623 • $\sigma(pp \rightarrow X + H) \approx 1 \times 10^{-11} \text{ b}$
- 1624 • $\sigma(pp \rightarrow X + H; H \rightarrow \gamma\gamma) \approx 50 \times 10^{-15} \text{ b}$

1625 In experiments with rotational symmetry, such as ATLAS, it is usual to
1626 define the differential cross-section ($\frac{d\sigma}{d\Omega}$) as the cross-section per solid angle.
1627 If the differential cross-section is integrated over corresponding the angular
1628 range, the cross-section for a specific region (σ_ϑ) is obtained:

$$1629 \quad \sigma_\vartheta = \int_0^\vartheta \int_0^{2\pi} \frac{d\sigma}{d\Omega} \sin(\vartheta) d\phi d\vartheta$$


with $\vartheta \in [0, \pi]$ is the coverage of the scattering angle.

The total cross-section is determined by the matrix element \mathcal{M} , which is independent of the experimental setup. The \mathcal{M} , also known as scattering amplitude, relates the initial state and the final state of a physical system undergoing a scattering process. Using \mathcal{M} , the total cross-section for a process is determined by:

$$\sigma_{tot} = \int \frac{d\sigma}{d\Omega} d\Omega = \int \frac{1}{\Phi} |\mathcal{M}|^2 dQ$$

1630 being Φ the incident particle flux in the process and the parameter dQ
1631 describes the kinematic phase space.

1632 2.2.6 The Pile-up effect

1633 Pile-up is a challenging matter among detectors and for the acquisition
1634 and analysis of the data. In particle physics, pile-up is called to the situation
1635 where the detector is being affected by several events at the same time.

1636 Even though the bunches are composed by $\sim 10^{11}$ protons, there are
1637 only around 30 collisions per crossing with nominal beam currents. The
1638 mean number of interactions per bunch crossing is presented in Figure 2.10
1639 for each year of Run-2. The data shown in Figure 2.10 is recorded by AT-
1640 LAS during stable beams at $\sqrt{s} = 13 \text{ TeV}$. The mean number of interactions

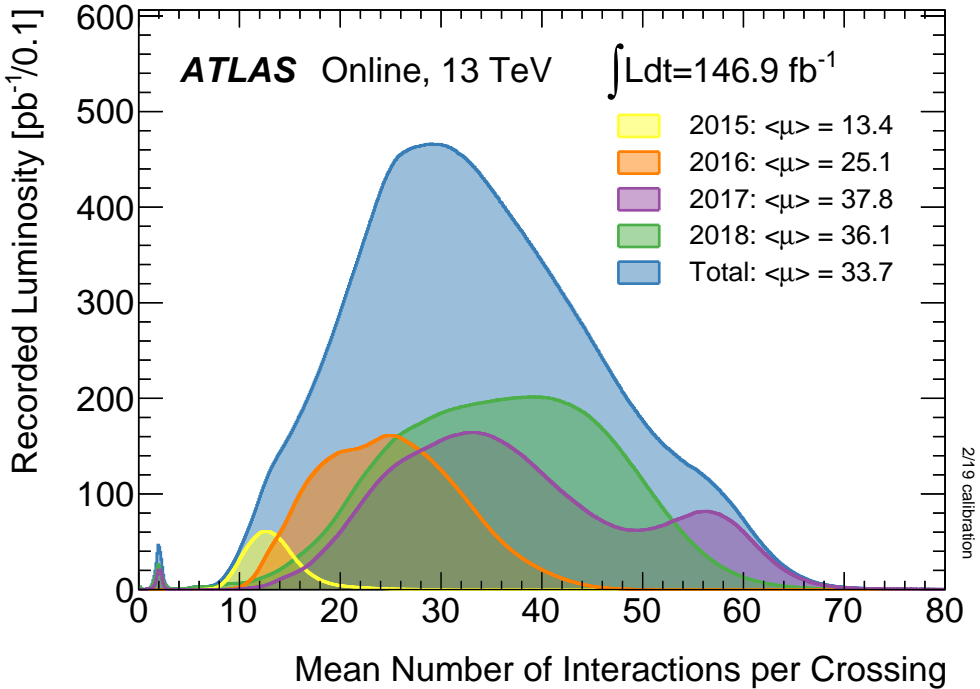


Figure 2.10: Luminosity-weighted distribution of the mean number of interactions per crossing $\langle \mu \rangle$ for Run-2 with pp collisions data.

per crossing corresponds to the mean of the poisson distribution of the number of interactions per crossing calculated for each bunch. It is calculated from the instantaneous per bunch luminosity as $\langle \mu \rangle = \mathcal{L}_{bunch} \times \sigma_{inel}/f_r$ where \mathcal{L}_{bunch} is the instantaneous luminosity per bunch, $\sigma_{inel} = 80$ mb is the inelastic cross section of pp collisions at 13 TeV and $f_r = 11.245$ kHz is the LHC revolution frequency.

Work in progress

2.2.7 Phenomenology of proton-proton collisions

During LHC Run-2 data taking period, the protons were colliding at a center-of-mass energy of $\sqrt{s} = 13$ TeV. The pp total cross-section at this energy is measured to be $\sigma_{tot} = (110.6 \pm 3.4)$ mb [144]. The luminosity-independent method used to measure σ_{tot} allows to split the cross-section into elastic and inelastic cross-sections, $\sigma_{el} = (31.9 \pm 1.7)$ mb and $\sigma_{inel} = (79.5 \pm 1.8)$ mb respectively. However, only inelastic scattering generates particles with an sufficient angle with respect to the beam axis so that these particles enter into the geometrical acceptance of the detector. Figure 2.11 shows the cross-section (elastic, inelastic and total) for pp collisions

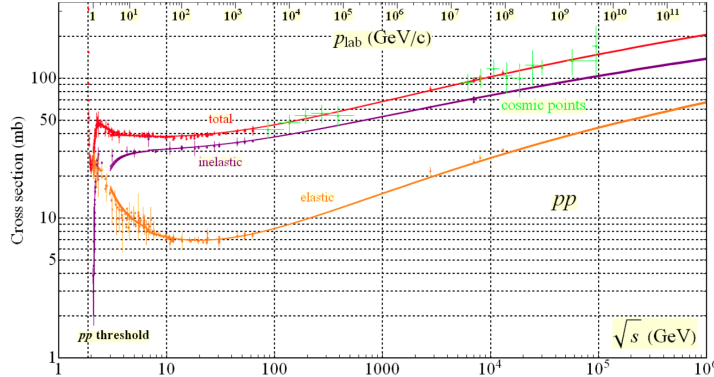


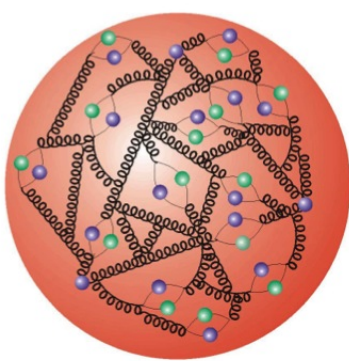
Figure 2.11: Total and elastic cross-section for pp collisions as a function of the laboratory momentum and the \sqrt{s} [145].

1658 depending on \sqrt{s} ([Why the values of the Figure 2.11 do not match the: \$\sigma_{tot} = \(110.6 \pm 3.4\)\$, \$\sigma_{el} = \(31.9 \pm 1.7\)\$ and \$\sigma_{inel} = \(79.5 \pm 1.8\$ \)](#)).
1659 The shown cross-section can be computed as the convolution of parton
1660 density functions (PDF) with the parton scattering matrix element \mathcal{M} .
1661

1662 Unlike leptons, protons are composite objects since they are made of
1663 quarks and gluons. Therefore and specially at LHC energy regime, the pp
1664 collisions cannot be described as a point-like interactions, here is where the
1665 PDFs come into play. The PDFs are functions containing the long distance
1666 structure of the hadron in terms of valence and sea quarks and gluons.
1667 This description is known as “parton model”.

1668 2.2.7.1 Proton structure and parton model for collisions

1669



The parton model for hadrons describes these non-fundamental particles as a composite of a number of point-like constituents named partons. The proton is not only simply made of three quarks (uud , the so called “valence” quarks) but also, there is a “sea” of gluons and short-lived quark and anti-quark pairs. The partons in the sea are continuously interacting with each other and can have any flavour.

1670 The PDFs describe the distribution of the hadron’s momentum among
1671 its constituents. The PDFs are essential to describe the pp interactions be-
1672 cause these collisions cannot be understood as point-like particles crashing.
1673 Instead, all the constituents of the protons are taken into account [68].

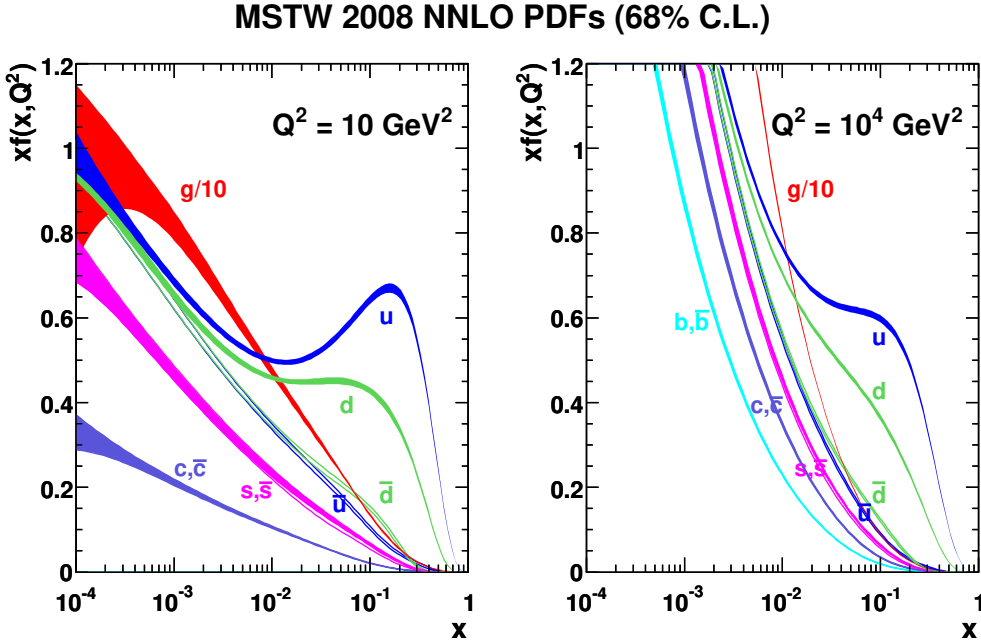


Figure 2.12: Parton distribution functions $xf(x, q^2)$ plotted against x for gluons different quark flavours at $Q^2 = 10 \text{ GeV}^2$ and $Q^2 = 10^4 \text{ GeV}^2$ using MSTW 2008 NNLO [69].

1674 Due to the fact that inside of hadrons the quarks are continuously interacting
 1675 with each other via the exchange of gluons, it is not possible to calculate PDFs using non-perturbative QCD. Instead, the momentum distribution function of the partons within the proton is obtained by a fit on
 1676 a large number of cross-section data points over a grid of x and Q^2 values
 1677 obtained from many experiments (deep inelastic scattering, Drell-Yan and jet measurements). There are various global fitting collaborations (ABM,
 1678 CT, MMHT, NNPDF, MSTW, CTEQ), each taking different approaches
 1679 to this fitting procedure. These fits are later extrapolated to new energy
 1680 scales.

1684 Formally, the PDF $f_{a/A}(x, Q^2)$ is defined as the probability of finding
 1685 a parton a within the hadron A carrying a fraction $x = p_a/p_A$ of its momentum
 1686 at Q^2 energy scale. The energy scale Q characterises the hard scattering and typically corresponds to the momentum transfer in the given process. As an example, several PDFs at two different scale energies are presented in Figure 2.12 as a function of x .

1690 The momentum of the proton is distributed among its constituents and,
 1691 while at lower energies ($Q \sim 1 \text{ GeV}$) it is shared mainly between the valence quarks, at higher energies ($1 < Q \lesssim 1 \text{ GeV}$) the emission of gluons carrying a some of the initial momentum of the quark is more probable. Within the

1694 QCD theory, these interactions can be classified in two main groups: “hard”
 1695 and “soft”. The hard processes are those involving large momentum trans-
 1696 fer. This type of processes are well understood and their cross-section can
 1697 be predicted with good precision using perturbation theory. In contrast,
 1698 the low momentum transfer of soft interactions leads to a much more dom-
 1699 inant impact of non-perturbative QCD, which makes much more difficult to
 1700 calculate the cross-section.

1701 When two protons (A and B) collide, what actually happens is that the
 1702 partons of one proton can interact with partons of the other via a hard
 1703 scattering process. Each of the interactions between the partons pairs (let a
 1704 be a parton from A interacting with b , a parton from B) is independent from
 1705 the interactions of other partons. The remaining partons also contribute to
 1706 the final state as “underlaying events”.

In a pp or, more generally, in a hadron-hadron (A and B) hard scattering process, the total cross section is given by:

$$\sigma_{AB \rightarrow X} = \sum_{a,b} \iint dx_a dx_b f_a(x_a, Q^2) f_b(x_b, Q^2) \times \hat{\sigma}_{ab \rightarrow X} \quad (2.12)$$

1707 where a and b denote the parton constituents of the hadrons A and B
 1708 respectively and $f_i(x_i, Q^2)$ their PDF. Here, the Q is chosen to be the fac-
 1709 torisation scale (μ_F). The contributions of the individual partons a and b is
 1710 denoted by $\hat{\sigma}_{ab \rightarrow X}$. With this equation, all process in pp collisions can can
 1711 be computed.

Depending on the order achieved in perturbation theory (LO, NLO, NNLO, ...), the cross-section of the individual partons to give the final state of instest ($ab \rightarrow X$) is calculated as

$$\begin{aligned} \hat{\sigma}_{ab \rightarrow X} &= \sum_{i=0}^{\infty} \alpha_s^i(\mu_R) \sigma_n(x_a, x_b, \mu_F^2) \\ &= [\sigma_{LO}(x_a, x_b, \mu_F^2) + \alpha_s(\mu_R) \sigma_{NLO}(x_a, x_b, \mu_F^2) \\ &\quad + \alpha_s(\mu_R)^2 \sigma_{NNLO}(x_a, x_b, \mu_F^2) + \dots]_{ab \rightarrow X} \end{aligned}$$

1712 where $\alpha_s^i(\mu_R)$ is the coupling constant derived for a specific renormalization
 1713 scale (μ_R).

1714 **Work in progress**

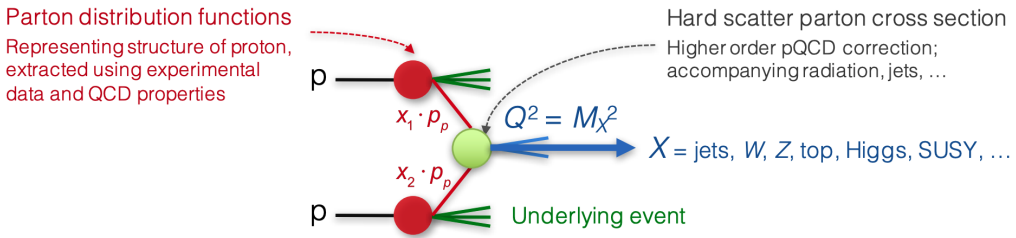


Figure 2.13: Simplified view of a pp collision [140].

1715 **2.2.7.2 Underlaying event**

1716 **2.3 ATLAS**

1717 Installed in its experimental cavern at point 1, ATLAS is the largest de-
1718 tector ever constructed for a particle collider with its 46 m long and 25 m in
1719 diameter. It is designed to record events of high-energy colliding particles
1720 at high luminosities. The thousands of millions of interactions that take
1721 place at the centre of the ATLAS detector are recorded and processed by
1722 the different sub-detectors, which are composed by more than 100 million
1723 sensitive electronic channels. Each ATLAS sub-detector is sensible to a dif-
1724 ferent type of particle and to different properties. Therefore, the layered
1725 structure allows for effective particle identification, as well as enables accu-
1726 rate measurements of energy and momentum. Figure 2.14 shows an overall
1727 layout of the ATLAS detector and identifies its different sub-detectors. In
1728 the picture can be appreciated that the cylindrical shape of ATLAS is di-
1729 vided into two parts: the “barrel” (curved parts) and the two “end-caps”
1730 (bases). In the barrel region, the sub-detectors are built as coaxial layers
1731 around the beam pipe (see memo 2.15). As one moves away from the axis,
1732 it finds the Inner Detector (ID), the solenoid magnet, the Electromagnetic
1733 (ECAL) and Hadronic (HCAL) Calorimeters, and the Muon Spectrometer
1734 (MS) in the outermost layer. The technical details of these sub-detectors
1735 are presented in the coming sections.

1736 ATLAS is able to explore a wide range of phenomena with high pre-
1737 cision, including new physics events. Even though it is a general-purpose
1738 experiment, it was designed taking into account the Higgs searches that
1739 were carried out at LHC. This is why, since the mass of the Higgs was not
1740 known at that time, its performance requirements cover a large mass range
1741 for the Higgs decay products.

1742 The stone for the foundations of ATLAS was laid in March 1992 at
1743 the critical ‘Towards the LHC Experimental Programme’ meeting, where
1744 physicists proposed several possible experiments for the LHC [147]. Two

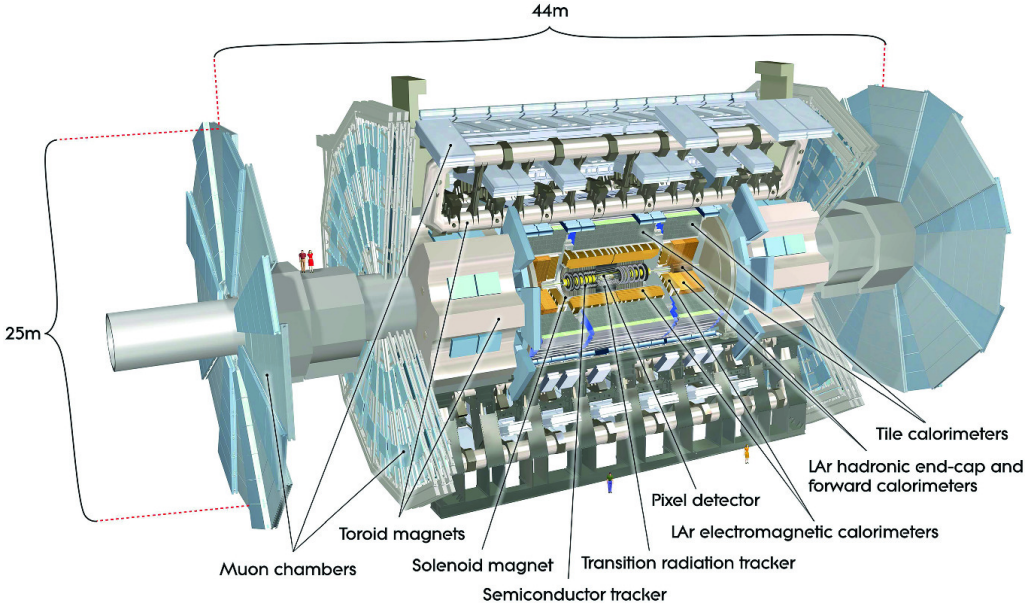


Figure 2.14: Simulated schematic view of the ATLAS detector.

1745 projects based on large toroidal magnet systems were proposed EAGLE
 1746 and ASCOT. By the summer of that year, both experiments merged into
 1747 ATLAS. In October 1992, the letter of intent of the ATLAS Collaboration
 1748 was sent to the LHC Experiments committee and, in 1994, the technical
 1749 proposal [148]. In 1997 the formal approval of the ATLAS experiment
 1750 arrived and one year later the excavation on the cavern began. The cavern
 1751 was inaugurated five years later and the construction of the ATLAS detector
 1752 ended in 2008. Later, in 2009, at $\sqrt{s} = 2.36$ TeV, ATLAS records its first
 1753 collisions [149].

1754 One of the most important milestones for ATLAS (and for all science in
 1755 the last decades) was the observation of a particle consistent with the Higgs
 1756 boson in July 2012 (see 1.3.1). In 2016, the combination of ATLAS and
 1757 CMS measurements for Higgs boson production on decay rates with Run-
 1758 1 data was published [150]. After that, the physics programme at 13 TeV
 1759 allowed precision studies of the Higgs boson and other SM particles, as well
 1760 as the search for new particles with higher masses.

1761 Other relevant items in ATLAS timeline are the observation and rate
 1762 measurement of $t\bar{t}$ events [151] or the evidence for rare electroweak $W^\pm W^\pm$
 1763 production [152]. The first evidence of light-by-light scattering at high
 1764 energy was also found with ATLAS [153]. The first $t\bar{t}H$ associate production
 1765 [154] and $H \rightarrow b\bar{b}$ decays [155] were observed for first time by ATLAS too.

1766 The physics programme of ATLAS include precise measurements of the
 1767 SM [156], super-symmetry studies [157], sources of \mathcal{CP} -violation [158], large



Figure 2.15: Due to its coaxial-layered structure ATLAS can be understood as cylindric onion: “*ATLAS have layers, onions have layers*” [146].

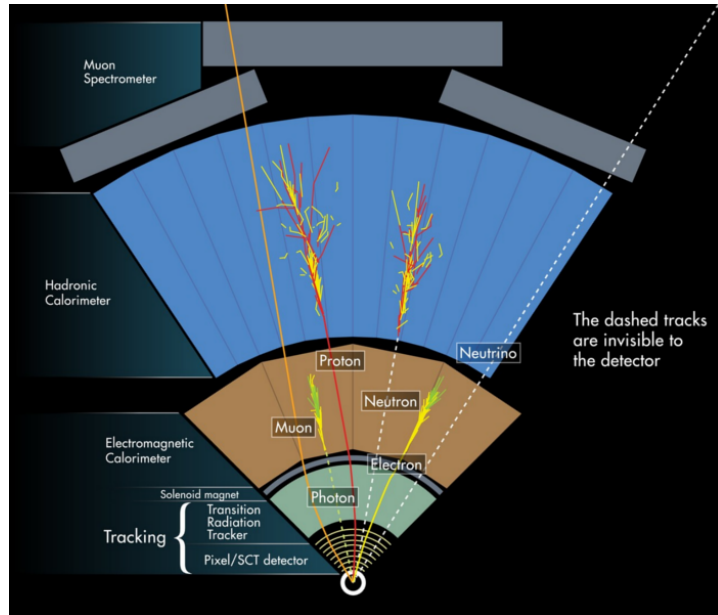


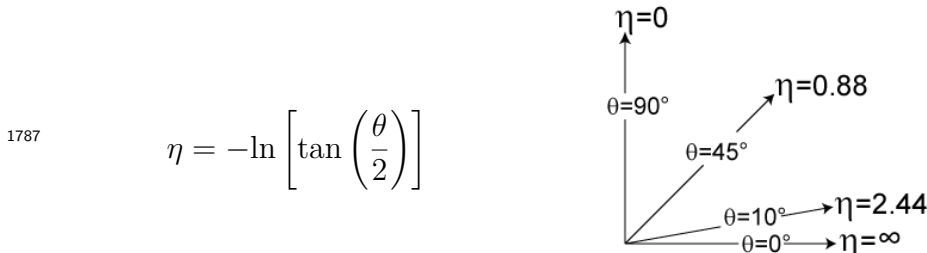
Figure 2.16: Fraction of the transversal plane of ATLAS. Each particle leaves a different signature in each layer. By signature is meant the particular distribution of energy deposition. This scheme is fundamental to understand the object reconstruction in the next chapter.

¹⁷⁶⁸ E_T^{miss} dark matter searches [159], astroparticle physics [160], extra dimensions [161] and others.

¹⁷⁷⁰ ATLAS is not only a detector but also a collaboration of people composed of more than 5000 members including physicists, engineers, technicians, doctoral students and support staff. Working at CERN or at any ¹⁷⁷¹ of the 181 institutions that constitute ATLAS, the different teams work ¹⁷⁷² collaboratively to achieve success. Any output by any of the teams comprising ¹⁷⁷³ ATLAS is shared with the rest of the collaboration and subjected to a strict review process before making the results public, ensuring high- ¹⁷⁷⁴ quality standards. ¹⁷⁷⁵

¹⁷⁷⁸ 2.3.1 Coordinate system

¹⁷⁷⁹ Due to its cylindrical structure, ATLAS uses a right-handed system with ¹⁷⁸⁰ its origin at the IP where the collisions take place. On one side, there are the ¹⁷⁸¹ ($x, y, z,$) Cartesian coordinates. The x -axis is pointing towards the centre ¹⁷⁸² of the ring circumference, the y -axis is perpendicular to the plane defined ¹⁷⁸³ by the LHC ring and it points to the surface, and the z -axis is defined by ¹⁷⁸⁴ the direction of the beam. On the other side, it is more frequent to employ ¹⁷⁸⁵ the cylindrical coordinates (r, ϕ, z) or the system defined by the azimuthal ¹⁷⁸⁶ angle (ϕ) and the pseudorapidity (η) :



where θ is the polar angle⁴. As the polar angle approaches zero, pseudorapidity tends towards infinity. The change in pseudorapidity $\Delta\eta$ is Lorentz invariant under boosts along the beam axis. The use of η is preferred over θ because the distribution of events typically looks flat with respect to η . In terms of the momentum, the above equation can be expressed as:

$$\eta = -\ln \left(\frac{|\vec{p}| + p_z}{|\vec{p}| - p_z} \right)$$

¹⁷⁸⁸ being p_z the momentum along the beam direction. The rapidity is used ¹⁷⁸⁹ when dealing with massive particles and it can be expressed as $y = \frac{1}{2}\log[(E+$

⁴Defined as the angle between the particle three-momentum, \vec{p} and the positive direction of the beam axis.

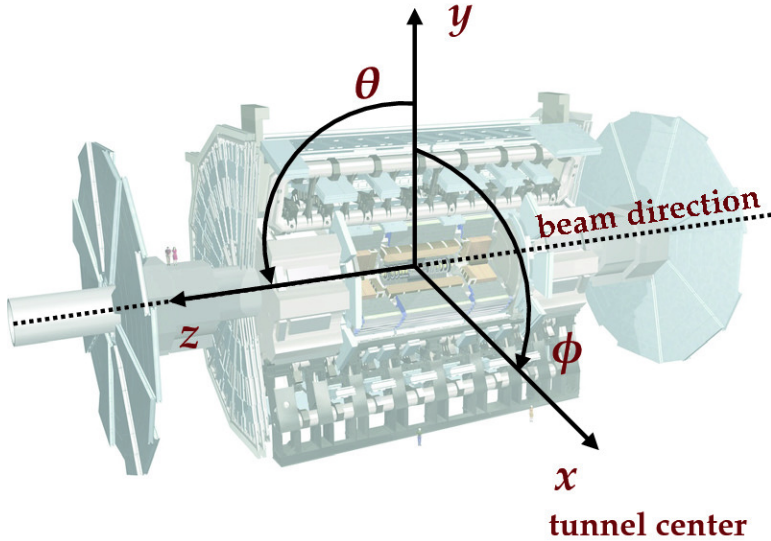


Figure 2.17: Coordinate system of the ATLAS detector.

1790 $p_z)(E - p_z)]$, being E the energy projection of the momentum in the z -axis.
 1791 Note that when the particles approach the speed of light, they are in the
 1792 limit $E \approx |\vec{p}|$ and the values for rapidity and pseudorapidity converge. The
 1793 angular distance is measured in units of $\Delta R = \sqrt{(\Delta\eta)^2 + (\Delta\phi)^2}$, which is
 1794 invariant under a boost along the z -axis⁵. Figure 2.17 shows the coordinate
 1795 system of ATLAS for both Cartesian and cylindrical coordinates.

The transverse magnitudes such as the transverse momentum (p_T) and transverse energy (E_T) are defined in the x - y plane. Knowing the p_T , and the η and ϕ angles, the cartesian momentum (p_x, p_y, p_z) can be derived from:

$$\begin{aligned} p_x &= p_T \cos(\phi) & p_y &= p_T \sin(\phi) \\ p_z &= p_T \sinh(\phi) & |\vec{p}| &= p_T \cosh(\phi) \end{aligned}$$

1796 2.3.2 Inner Detector

1797 The ATLAS ID [162][163][122] is the closest sub-detector to the beam
 1798 pipe. Its layout is shown in Figures 2.18 and 2.19. The charged particles
 1799 follow a curved trajectory inside the ID due to the magnetic field of the AT-
 1800 LAS bending magnet (see 2.3.5). The different pieces that comprise the ID
 1801 can reconstruct the traces of these particles with great accuracy allowing,
 1802 thus, to measure its momentum (this is done using the sagitta method de-
 1803 scribed in Section 3.3.1.1). For particles coming from the IP, the geometric
 1804 acceptance of the ID is $|\eta| < 2.5$ for pseudorapidity and full ϕ coverage in

⁵ $\Delta\eta = \eta_2 - \eta_1$ and $\Delta\phi = \phi_2 - \phi_1$.

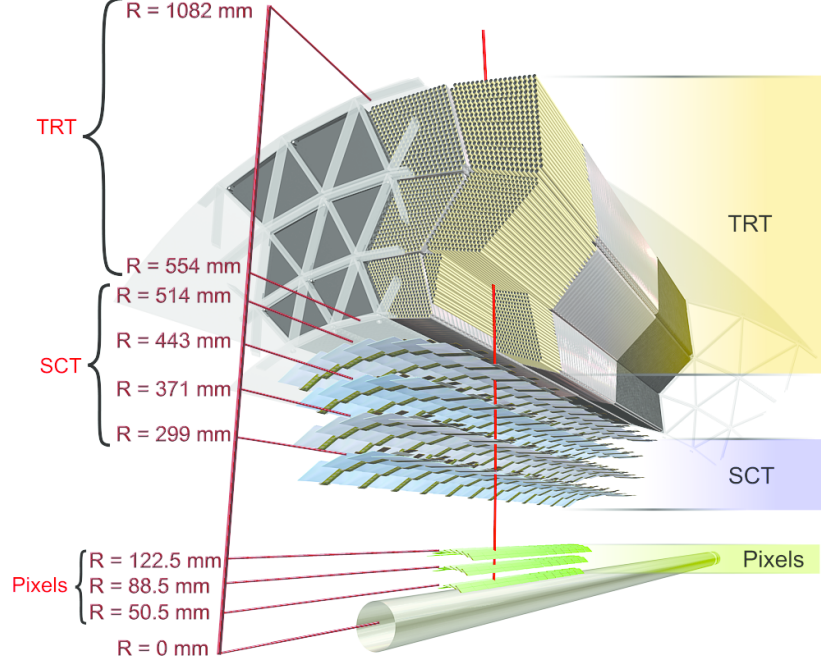


Figure 2.18: Barrel part of ID of the ATLAS experiment with the Pixel, SCT and TRT sub-detectors. The IBL is not shown here.

1805 the azimuthal angle. The ID provides p_T resolution of $\sigma_{p_T}/p_T = 0.05\%$ GeV
 1806 $\oplus 1\%$ and a transverse impact parameter resolution⁶ of $10 \mu\text{m}$ for particles
 1807 in the central η region. It is designed to provide excellent momentum resolu-
 1808 tion, pattern recognition and measurements of both primary and secondary
 1809 vertex for charged particles above the p_T threshold (nominally 0.5 GeV).

1810 The ID is composed of four complementary sub-detectors: The Insert-
 1811 able B-Layer (IBL), the Pixel Detector, the Semiconductor Tracker (SCT)
 1812 and the Transition Radiation Tracker (TRT). In the sections that follow, a
 1813 description of each sub-system is provided.

1814 Depending on the η that a particle has, it will interact with some ele-
 1815 ments of the detector. Figure 2.19 shows the end-cap elements transversed
 1816 by two charged particles with $\eta = 2.2$ and 1.4 . The track with $\eta = 1.4$
 1817 traverses first the beryllium beam-pipe, then the three cylindrical silicon
 1818 pixels and the four disks with double layers of the SCT. Finally, this particle
 1819 travels across approximately 40 tubes in the TRT wheels. In contrast, the
 1820 particle with $\eta = 2.2$ encounter the first of the cylindrical silicon-pixel layers
 1821 after leaving the beryllium pipe. Then, the two end-cap pixel disks and the
 1822 four last disks of the end-cap SCT.

⁶The impact parameter determine the distance of a reconstructed track from a charged particle to the perigee (the closest point of the track to the global z -axis)

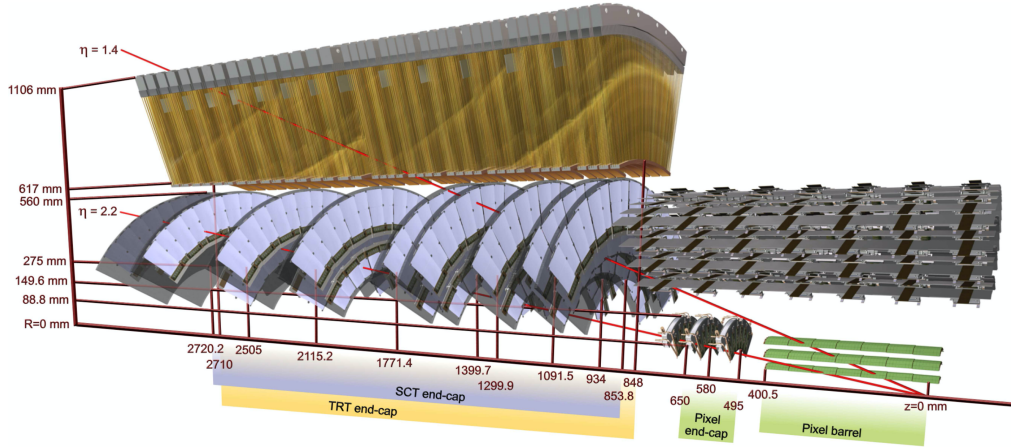


Figure 2.19: End-cap of the ID.

1823 Silicon semiconductors

1824 When a charged particle traverses a doped silicon semiconductor, it creates
 1825 a pair electron-hole by ionisation. An electric field is applied to the active
 1826 part of the detector module so that the electron drifts in oposite direction
 1827 of the electric field and the hole in the field direction. Then, both charges
 1828 are collected by the p-n junctions. The silicon sensors can be shaped either
 1829 as pixels, providing precies 2D space point, or as strips, giving a single
 1830 dimension positioning. On the order of 10^5 electron-hole pairs are liberated
 1831 when a particle crosses the silicon wafer and, with appropriate electronics,
 1832 a clear signal is obtained in the pixel or strip in which the charged was
 1833 collected.

1834 2.3.2.1 Insertable B-Layer

1835 The IBL [164] is the innermost component of the ID. It is located
 1836 between the beam pipe and the pixel detector. Added after Run-1, it
 1837 provides the closest-to-IP measurements. This improves the robustness and
 1838 performance of the ATLAS tracking system. It plays a fundamental role
 1839 for b -tagging efficiency because this tagging relies on precise vertex recon-
 1840 struction. The IBL provides redundancy in the measurements of tracks in
 1841 order to control the fake rate arising from random combinations of clusters
 1842 in events with a high pile-up background.

1843 With a hit resolution of $8 \mu\text{m}$ in $r\text{-}\phi$ and $40 \mu\text{m}$ along z , the IBL covers
 1844 the $|\eta| < 2.7$ and the entire ϕ range.

1845 The barrel structure if the IBL has a radius of 3.2 cm and is composed
 1846 by 14 carbon fibre staves as it is shown in Figure 2.20. Each stave has

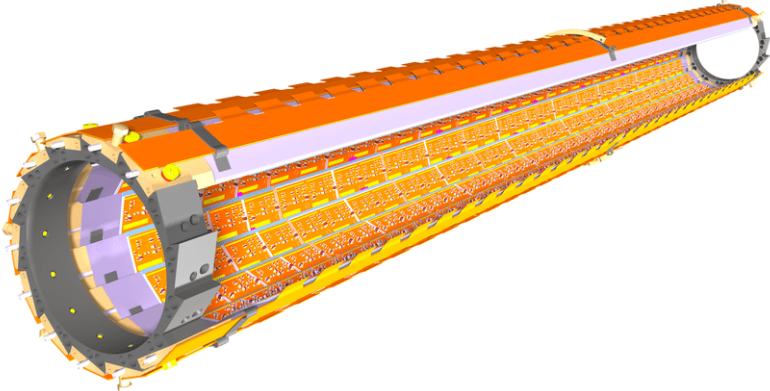


Figure 2.20: Schematic drawing of the ATLAS IBL Detector [164].

1847 incorporated cooling CO₂ circuits, has 32 or 16 modules and uses two types
1848 of photodetectors: ATLAS pixel planar sensors and 3D pixel sensors. The
1849 used pixels have a size of $50 \times 400 \mu\text{m}^2$. Due to the high luminosity of the
1850 LHC, the IBL is built with radiation-tolerant sensors.

1851 2.3.2.2 Pixel Detector

1852 The ATLAS Pixel Detector [165] consists of a strip detector in the out-
1853 ermost layers and a pixel detector in the region which is closer to the IBL.
1854 Along with the IBL, it aims to reconstruct the trajectories of the particles
1855 traversing it. It provides a full coverage of the azimuthal angle ϕ and a
1856 pseudorapidity range of $|\eta| < 2.5$ as well as a resolution of $10 \mu\text{m}$ in $r\text{-}\phi$ and
1857 $115 \mu\text{m}$ in the z .

1858 The Pixel Detector and the IBL combined contain 92×10^6 pixels with its
1859 respective electronic channels, which cover an area of approximately 1.9 m^2
1860 of silicon consuming 15 kW. The barrel region consists of four concentric
1861 layers equipped with 1736 sensor modules and each of the two end-caps
1862 has three disks with 2888 modules [166]. Figure 2.22 shows the assembly
1863 view and cross section of a module of the ATLAS ID Pixel Detector. Each
1864 of these modules consists on a silicon pixel sensor bonded to the front-end
1865 electronic chips.

1866 Hits in a pixel are read out if the signal exceeds a tunable threshold. The
1867 pulse height is measured using the Time-over-Threshold (ToT) technique.

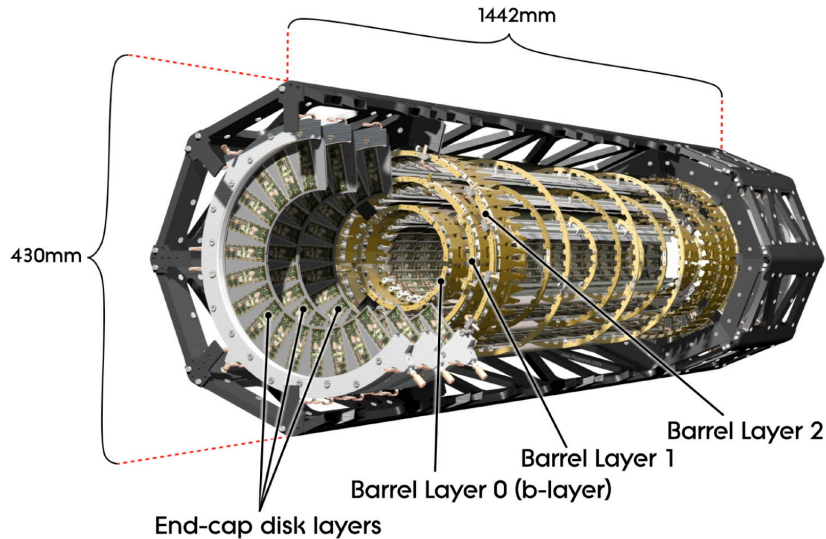


Figure 2.21: Schematic view of the ATLAS pixel detector consisting of individual barrel and end-cap layers [122].

1868 2.3.2.3 Semiconductor Tracker

1869 The SCT consists of 4088 modules tiling four coaxial cylindrical layers
 1870 in the barrel region and two end-caps each containing nine disk layers, all
 1871 of this surrounding the Pixel Detector and providing additional precision
 1872 tracking. The main difference with the Pixel Detector is that the SCT uses
 1873 microstrip sensor technology, which is very similar to that of a pixel but
 1874 being much larger (6 cm). The reason to use microstrips instead of pixels
 1875 is that the strips are more cost-effective than traditional pixels and a good
 1876 spatial resolution can be obtained as well if the strips are arranged with an
 1877 angular offset. Therefore, each SCT detector unit consists on two back-to-
 1878 back silicon-microstrip planes with a relative angle of 40 mrad. Eight strip
 1879 layers (i.e. four space points) are crossed by each track in the SCT providing
 1880 valuable tracking information with resolution of $17 \mu\text{m}$ in $r\phi$ and $580 \mu\text{m}$
 1881 in the z coordinate. The SCT covers the entire ϕ range and up to 2.5 in η .

1882 Figure 2.23 shows an exploded view of the different components of an
 1883 SCT module, including the high thermal conductivity spine, the polyimide
 1884 hybrids and readout chips.

1885 2.3.2.4 Transition Radiation Tracker

1886 The TRT is used in conjunction with the Pixel Detector and silicon micro
 1887 strip (SCT) to extend the η range in which the tracks can be reconstructed to
 1888 $|\eta| = 2$. This part of the ID is formed by a large number of 4 mm straw tubes

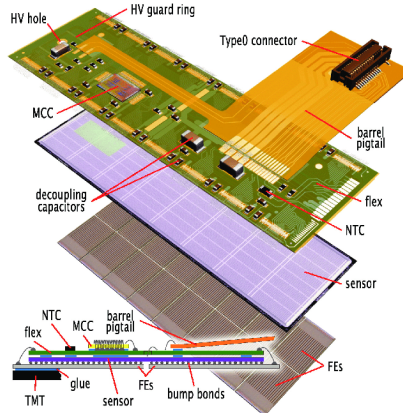


Figure 2.22: Pixel Detector module [165].

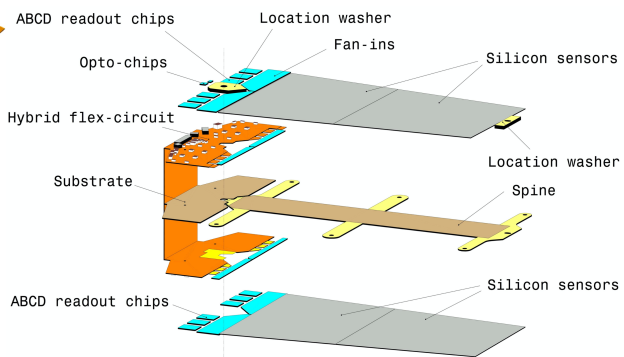


Figure 2.23: SCT detector module [122].

1889 filled with gas. This part of the ID relies both on the collection of primary
 1890 ionisation charge and the collection of secondary ionisation charge arising
 1891 from the transition radiation to measure the the track of charged particles.
 1892 The tube surface functions as a cathode while the wire in the center as
 1893 a cathode. When a charged particle pases through the gas in the tube, it
 1894 ionises the gas and the freed electrons drift towards the anode, generating an
 1895 electrical current. This detector provides a single hit resolution of $170\ \mu\text{m}$ in
 1896 $r\text{-}\phi$ but does not have sensitivity in z . The TRT also provides discrimination
 1897 between electrons and pions since the later generate a much smaller signal
 1898 than the former. When the electrons pass, they produce x-ray photons that
 1899 lead to strong avalanches within the tubes and, thus, a great signal.

1900 2.3.3 Calorimeters

1901 After the ID, the next layer of detectors in ATLAS correspond to the
 1902 calorimeters (Figure 2.24) [167]. Their purpose is to measure the energy
 1903 of the particles (neutral or charged), as well as to help to reconstruct the
 1904 path followed by them. Most particles initiate a shower (Section 2.3.3.1)
 1905 when they enter into the calorimeter. Part of the energy of these particles is
 1906 deposited in the device, then collected and measured by it. Most of calorim-
 1907 eters in particle physics are segmented transversely to provide information
 1908 about the direction of the particles. Based on how the particle shower devel-
 1909 ops, the longitudinal segmentation can provide information for identifying
 1910 the particle (a more detailed discussion of how particles are reconstructed
 1911 within the ATLAS detector is presented in Section 3.3).

1912 In general, calorimeters can be classified as sampling, when are made of
 1913 two types of materials, or homogeneous, built with just one type of material.

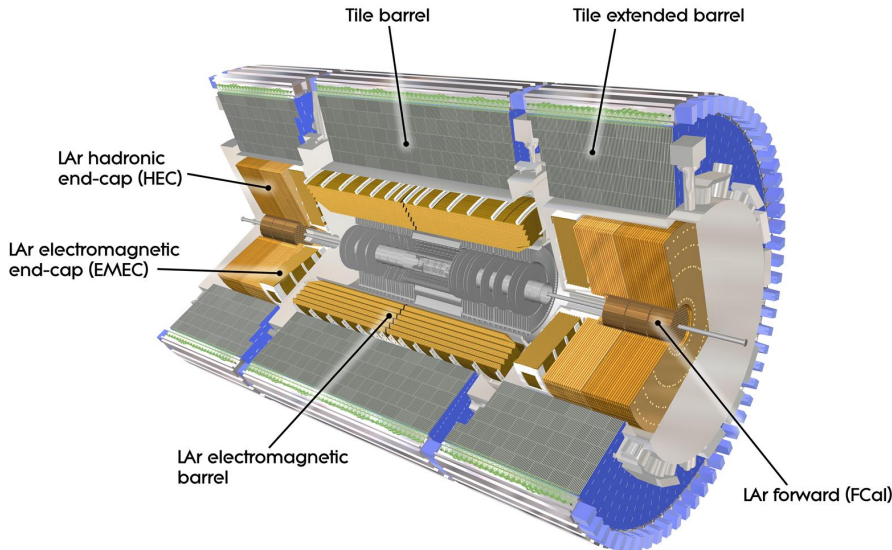


Figure 2.24: Computer generated image of the ATLAS calorimeter [166].

1914 ATLAS uses sampling calorimeters, which consist of alternating layers of
 1915 different materials:

- 1916 • **Passive material:** Also known as absorber, it is a denser material to
 1917 full stop the traversing particles. When a particle interacts with the
 1918 passive material it produces the shower (Figures 2.25 and 2.26). For
 1919 the absorber layers in ATLAS, lead is used for the ECAL and steel
 1920 for the HCAL.
- 1921 • **Active material:** This material detects the particles from the shower
 1922 originated in the absorber. The liquid Argon (LAr) is used as active
 1923 material for ECAL and plastic scintillator for HCAL.

1924 In the homogeneous calorimeters, the material used combines the features
 1925 of an absorber and a detector, performing both tasks.

1926 Since each type of particle interacts differently, there are two main types
 1927 of calorimeters: the electromagnetic calorimeter (ECAL), which measures
 1928 the energy of electrons/positrons and photons, and the hadronic calorim-
 1929 eters (HCAL), which registers the energy of the strongly-interacting particles.
 1930 Both classes are covered in the next sections.

1931 **Scintillator**

1932 The particles from the shower leave some of the molecules of the plastic

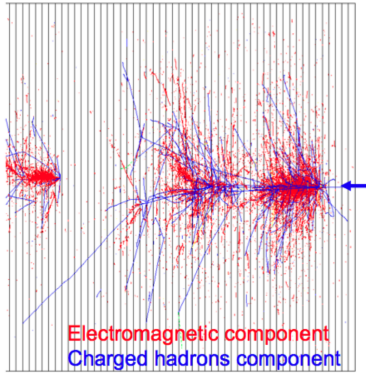


Figure 2.25: EM and hadronic cascades.

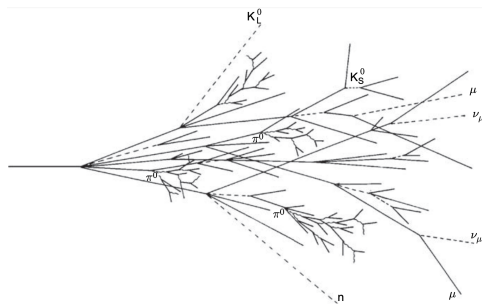


Figure 2.26: Sketch of a hadronic cascade [168].

1933 scintillator in an excited state. The subsequent decay of these molecules
1934 produces the emission of photons in the ultraviolet energy region. This
1935 light is collected by photomultiplier tubes at the edge of the tiles
1936 and converted into a current pulse whose amplitude is proportional to the
1937 energy deposited by transversing particle.

1938 **2.3.3.1 Particle showering**

1939 A particle shower is a cascade of secondary particles produced when
1940 a high-energy particle interacts with matter. The first particle interacts
1941 with the passive material producing a secondary particle with less energy
1942 than the first one. The second particle does the same and, in each step,
1943 the particles produced are less and less energetic. For a single incoming
1944 particle, this iterative process can continue for thousands of periods [168].
1945 An illustration of the EM and hadronic particle cascades is shown in Figure
1946 [2.25](#).

1947 **Electromagnetic shower**

1948 The electromagnetic (EM) shower is initiated by a e^- , e^+ or γ , these
1949 three particles are the sole components of this type of shower. At energies
1950 higher than 100 MeV, the EM showering is based on two main processes:
1951 Bremsstrahlung and pair creation. The electrons lose their energy almost
1952 exclusively by bremsstrahlung radiation, a process in which the lepton ra-
1953 diates thousands of soft photons because of its interaction with another
1954 charged particle. The photons lose their energy by the production of an
1955 $e^- - e^+$ pair. At lower energy scales, other processes contribute. In the MeV

range, the Compton scattering⁷ and photoelectric effect⁸ are the dominant interactions for energy loss for photons, while the ionisation and excitation are for the charged particles (e^- and e^+).

Hadronic shower

When a hadron interacts with the passive material, this shower is initialised. Both strong and EM interactions are involved in the development of this type of shower and they present a larger variety of particle components. Therefore, the hadronic showers are significantly more complex than the EM. Figure 2.26 shows the processes leading to a hadronic cascade.

The production of neutral pions represents about a third of the energy loss of hadronic interactions. These pions decay 98.8% of times to two photons [169] that are starting the EM showers. The rest of hadronic interactions consist of the production of charged mesons, nuclear fragments and protons, soft neutrons and photons or unpredictable loss through undetectable processes.

2.3.3.2 Electromagnetic calorimeter

The ECAL [167] absorbs the energy of the e^- , e^+ or a γ covering a pseudorapidity range of $|\eta| < 1.475$ in the barrel. It is made of a lead absorber and LAr detector following an accordion shape, as can be seen in Figure 2.27a, where the different layers are clearly visible. The shower originated at the absorber layer ionise the LAr producing a measurable current proportional to the energy of the original particle. The LAr layer operates at 87 K.

The barrel part is split into two identical half-barrels separated by a small gap at $z = 0$. Each end-cap calorimeter is composed of two coaxial wheels that cover $|\eta| < 1.475$.

The total amount of material in the ECAL corresponds to 25-35 radiation lengths, X_0 , and 2-4 nuclear interaction lengths, λ , over the entire η range. Characteristic of each material, the ration length is the mean distance over which a high-energy electron lose all but $1/e$ of its energy by bremsstrahlung. The radiation length is the mean free path between interactions required to reduce the number of relativistic charged particles by the factor $1/e = 0.37$ as they pass through matter.

⁷Scattering of a photon after interacting with a charged particle, usually an electron.

⁸Emission of photoelectrons when the EM radiation interacts with matter.

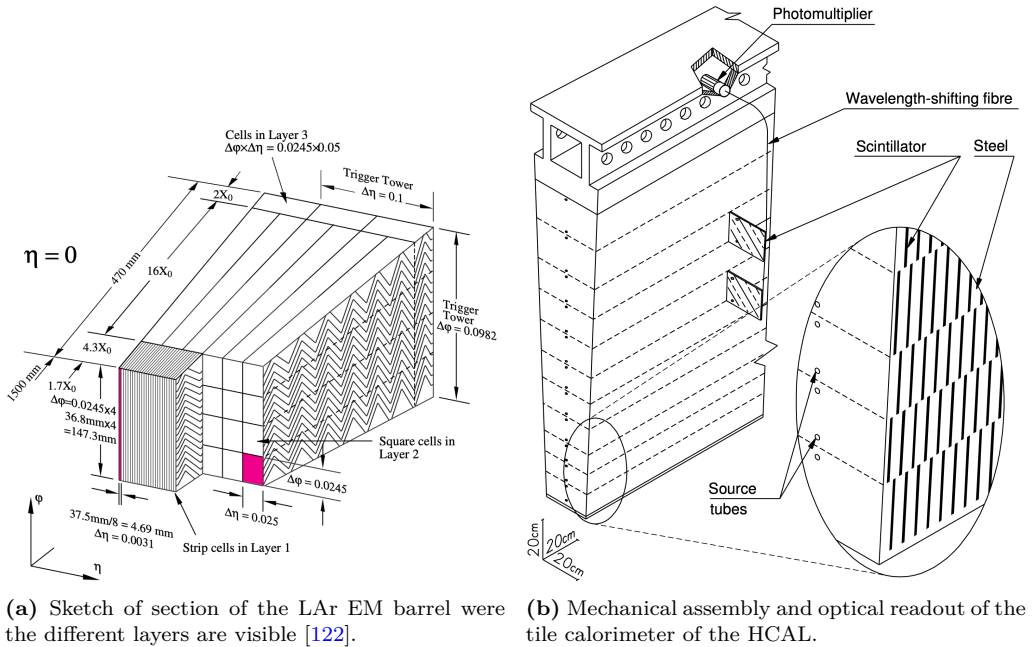


Figure 2.27: Sketch of a section of the ATLAS (a) ECAL and (b) HCAL [122].

The energy resolution of a calorimeter can be parametrised as:

$$\frac{\sigma_E}{E} = \frac{a}{\sqrt{e}} \oplus \frac{b}{E} \oplus c = \frac{10\%}{\sqrt{e}} \oplus \frac{170 \text{ MeV}}{E} \oplus 0.7\%$$

1989 Where a is the stochastic term, b the electronic noise and c a constant that
1990 includes detector instabilities and increases with E [170].

1991 **2.3.3.3 Hadronic calorimeter**

1992 The ATLAS HCAL [167] is made of a sampling calorimeter of steel and
1993 plastic scintillator tiles covering the pseudorapidity region of $|\eta| < 1.7$ in
1994 the barrels. The end-caps are made of copper and LAr, covering $1.5 < |\eta| <$
1995 3.2, and are emended in the end-caps of the ECAL. This calorimeter uses
1996 9800 electronic channels in the barrel and 5600 in the end-cap. With 2900
1997 tones, the HCAL is the heaviest part of the ATLAS detector. It has 420000
1998 scintillator tiles and 9500 photomultiplier tubes [166]. All these elements are
1999 shown in Figure 2.27b, where the tiles, the fibres and the photomultipliers
2000 are visible.

The contribution of the electronic noise is negligible, therefore, the energy resolution for the tile calorimeter is [167]:

$$\frac{\sigma_E}{E} = \frac{5.9\%}{\sqrt{e}} \oplus 5.7\%$$

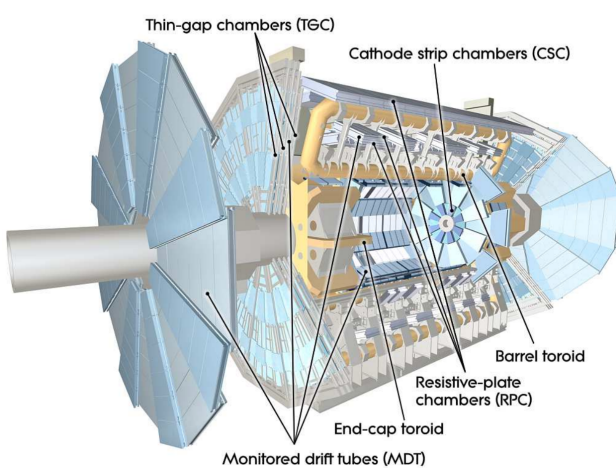


Figure 2.28: Conceptual layout of the MS (blue). The magnet system (yellow) is also shown [122].

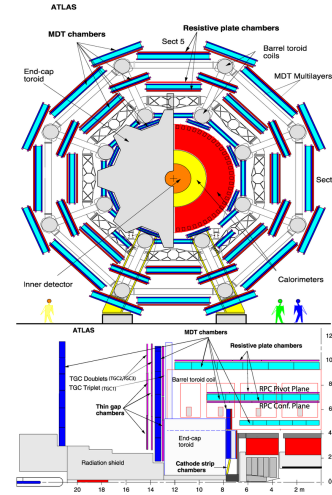


Figure 2.29: ATLAS Muon detectors.

2.3.3.4 Forward calorimeter

In addition to the ECAL and HCAL, a smaller calorimeter is placed in the end-caps surrounding the beam pipe in order to cover the forward region ($3.1 < |\eta| < 4.9$), the forward calorimeter (FCAL). This coverage is required for many physics tasks such as the reconstruction of the E_T^{miss} of the forward-jet tagging.

This calorimeter is a sampling calorimeter based on LAr as active medium and copper as absorber. The thickness of the FCAL is optimised to achieve high absorption, approximately, $10 X_0$ [170].

This detector has a resolution of:

$$\frac{\sigma_E}{E} = \frac{100\%}{\sqrt{e}} \oplus 10\%$$

2.3.4 Muon Spectrometer

The muons can penetrate through calorimeters and reach the last layer of the ATLAS detector, the MS [171]. Figure 2.28 shows a schematic cutaway view of the ATLAS muon system.

The MS surrounds the calorimeters and its aim is to measure the trajectories of muons to determine their direction and momentum with excellent tracking precision as well as their electric charge in a pseudorapidity coverage of $|\eta| < 2.7$. To bend the particle tracks after they exit the HCAL, the MS uses eight large superconducting air-core toroid magnets in $|\eta| < 1.4$

Type	Purpose	Location	Coverage
MDT	Tracking	Barrel + end-cap	$0.0 < \eta < 2.7$
CSC	Tracking	End-cap layer 1	$2.0 < \eta < 2.7$
RPC	Trigger	Barrel	$0.0 < \eta < 1.0$
TGC	Trigger	End-cap	$1.0 < \eta < 2.4$

Table 2.3: ATLAS MS sub-detectors [172].

region. For the $1.6 < |\eta| < 2.7$, the tracks are bent by magnets inserted in the end-caps. In the transition region, $1.4 < |\eta| < 1.6$, the magnetic field responsible of bending the particles is provided by both the air-core toroid magnets and the smaller end-cap magnets. These fields are perpendicular to the trajectory of the muons originated in the IP. More details about the magnet systems of the MS can be found in Section 2.3.5.

The MS instrumentation is based, on one hand, on precision chambers for the coordinate measurements in the bending plane: Monitored Drift Tube chambers (MDT) and Cathode-Strip Chambers (CSC), and, on the other hand, on trigger chambers: Resistive Plate Chambers (RPC) and Thin Gap Chambers (TGC). Table 2.3 gives a summary of the MS detector components. In Figure 2.29 the distribution of the MS detectors is described.

- **Monitored Drift Tube chambers (MDTs)** [173]: The MDT chambers provide precise momentum measurements by determining with high accuracy the curve of the tracks. This part of the MS cover a pseudorapidity range of $|\eta| < 2$. The MDTs are designed to have stand-alone measurement capability in order to safeguard against any unanticipated background and to ensure good discovery potential in the scenario of unexpected topologies. In the barrel region, the MDTs are arranged in three cylindrical stations coaxial to the beam axis and in the end-cal, the MDTs are vertically installed in three layers. An MTD chamber consists of six layers of drift tubes (as depicted in Figure 2.30), each of them with 3 cm of diameter, filled with gas. A tube can achieve a single wire resolution of $80 \mu\text{m}$ [172]. In the entire MDT system, there are 1 171 chambers with a total of 354 240 tubes.
- **Cathode-Strip Chambers (CSC)**: It is the innermost tracking layer of the MS. Due to its higher rate capability and time resolution, it is located close to the beam axis, where the particle fluxes are higher. This component of the muon detector system covers the η range $2.0 < |\eta| < 2.7$. It measures with precision the coordinates at

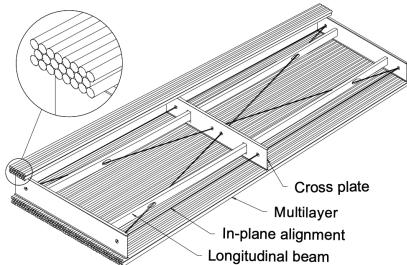


Figure 2.30: Schematic view of an MDT chamber.

the ends of the detector. With its 70 000 electric channel, provides a resolution around $60 \mu\text{m}$.

- **Resistive Plate Chambers (RPC)** [174]: This is the barrel element of the trigger system. These chambers are located on both sides of the central CSC and inside the outermost CSC station. The RPCs are gaseous detectors used for triggering and for measuring the second coordinate in the barrel region. RCPs provide a time-space resolution of $1\text{ cm} \times 1\text{ ns}$. The gas gap is of the order of 2 mm and the plate external surfaces are coated by thin layers of graphite painting. This part of the MS is composed of 3 800 electric channels.
- **Thin Gap Chambers (TGC)** [175]: As a first-level trigger, they have to provide high efficiency and excellent time resolution for bunch-crossing tagging in a high-background environment. The particle flux received by the TCG is higher than that of the RPC. The three TGCs are located near the middle end-cap MDT station, in the forward regions. TGCs measure the second coordinate in the non-bending direction with its circa 440 000 electrical channels.

2.3.5 Magnet system

The curvature in the track of the particles is fundamental to measure the transverse momentum and the charge of the particles. To bend the path of charged particles, these are immersed in a homogeneous magnetic field which is produced by the both the toroidal and solenoid magnets. The bending power is proportional to $\int B dl$, where B is the magnetic field component orthogonal to the charged direction.

ATLAS magnetic system is divided into three subsystems: the central solenoid magnet, the barrel toroids (BT) and the end-cap toroid (ECT).

2076 **2.3.5.1 Central solenoid magnet**

2077 The ATLAS solenoid surrounds the ID providing a 2 T magnetic field at
2078 the centre of the tracking volume. This magnet is very thin, having only
2079 4.5 cm thickness, which minimises the interaction of the particles with the
2080 magnet material. It is important to not use a lot of material here because,
2081 otherwise, the interaction of the particles with the solenoid magnet would
2082 impact negatively in the performance of the calorimeters. To achieve such
2083 a field within a small thickness, 9 km of niobium-titanium superconductor
2084 wires into strengthened, pure aluminium strips and cooled down to 4.5 K are
2085 used. The central solenoid magnet has a cylindrical shape with a diameter
2086 of 5.6 m and a length of 2.56 m, and it weights 5 tonnes.

2087 **2.3.5.2 Toroid magnets**

2088 Three large air-core toroids (one barrel and two end-caps) generate the
2089 magnetic field in the MS. Each toroid consists of eight coils assembled with
2090 cylindrical symmetry (see the yellow elements in Figure 2.28). The coils are
2091 based on an aluminium stabilised Niobium-Titanium alloy (Al/NbTi/Cu)
2092 superconductor operating at 4.5 K. The main difference between the barrel
2093 and end-cap toroids for the cold mass is that the latter has a higher critical
2094 current and less aluminium than the former [176].

2095 **Barrel Toroid**

2096 The Barrel Toroid magnet is the largest component of the ATLAS magnet
2097 system. It generates a toroidal magnetic field which, as introduced in Sec-
2098 tion 2.3.4, is almost completely perpendicular to the track of the particles.
2099 In order to minimise the impact (i.e. reduce any interaction apart from
2100 applying magnetic field) of the magnet system with the particles, the barrel
2101 toroid is designed as an open and light structure. The barrel toroid coils
2102 are housed in eight individual cryostats, with the linking elements between
2103 them providing the overall mechanical stability. A view of the coils of the
2104 barrel toroid in their cryostats is in Figure 2.31.

2105 The magnetic flux density delivered by this magnet is 3.9 T on the su-
2106 perconductor. For the toroid barrel, the bending power ($\int B dl$) is in the
2107 interval 1.5 Tm to 5.5 Tm in $0 < |\eta| < 1.4$. It is the largest toroidal magnet
2108 ever built (25.3 m in length), being probably the most iconic and character-
2109 istic element of ATLAS. It weights 830 tonnes and uses more than 56 km of
2110 superconducting wire [166].

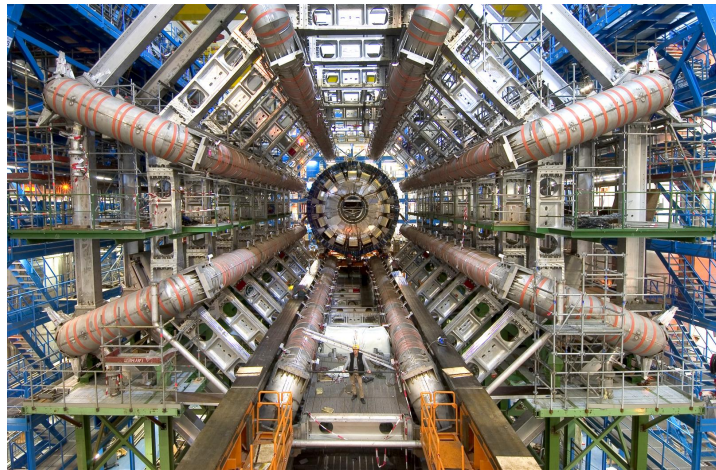


Figure 2.31: Very cool picture of the installation ATLAS calorimeters. The eight coils that compose the ATLAS barrel toroid magnets are already installed in the cryostats. Thus view is one of the most iconic of the ATLAS detector.

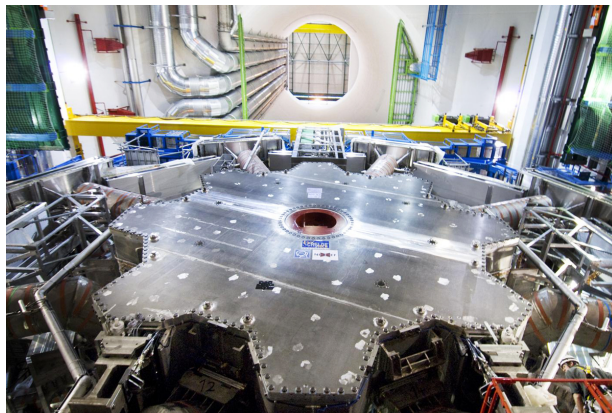


Figure 2.32: One of the two end-cap toroidal magnets. Each is made by eight superconducting coils with a magnetic field peaking at 4.1 T.

2111 **End-cap Toroid**

2112 The end-caps extend the magnetic field of the barrel toroid to the beam pipe.
 2113 These magnets are constrained by the inner radius of the barrel toroid and
 2114 the axial length of the experiment.

2115 As well as in the barrel toroid, it has a 4.1 T magnetic field on the
 2116 superconductor. For the end-cap toroid, the $\int B dl \in [4, 8]$ Tm in the
 2117 pseudorapidity range $1.6 < |\eta| < 2.7$ [176]. In the transition region where
 2118 the end-cap and barrel toroids overlap ($1.4 < |\eta| < 1.6$), the bending power
 2119 is lower. Each end-cap magnet (Figure 2.32) has a diameter 10.7 m and
 2120 weights 240 tonnes [166].

2121 **2.3.6 Trigger and Data Acquisition System**

2122 The proton bunches cross at the center of the ATLAS detector 40 million
2123 times per second, resulting in approximately (using Run-2 mean pile-up
2124 $\langle\mu\rangle = 33.7$) 1 200 million proton collisions per second. Reading out and
2125 storing all the information from this interactions is not feasible since it has a
2126 combined data volume of more than 60 million megabytes per second. Only
2127 some of these events are of interest to physics studies and, consequently,
2128 only this subset need to be saved into permanent storage for later analysis.
2129 In order to select only interesting data, ATLAS uses a complex and highly
2130 distributed Trigger and Data Acquisition System (TDAQ) [177] that reduces
2131 the rate of recorded data from the initial 1 200 MHz of interactions to just
2132 an average of 1 kHz. The reduction through the trigger is carried in two
2133 steps: The electronic performs an initial selection and, afterwards, a large
2134 computer farm analyses the data that pass the initial filter.

2135 The TDAQ system is an essential component of ATLAS in charge of
2136 processing the events online, selecting the relevant ones and storing them.
2137 To do so, the TDAQ verifies for each bunch crossing if at least one among the
2138 hundred conditions is satisfied. These conditions, also known as “triggers”,
2139 are based on identifying both combinations of candidate physics objects
2140 (“signatures”) and global properties of the events [178]. Figure 2.33 shows
2141 a diagram of the TDAQ system, in this figure can be seen the different
2142 components as well as the detector read-out and data flow.

2143 The first-level trigger (LVL1) is a hardware-based filter performed by
2144 ATLAS sub-detectors. The LVL1 uses the information of the Calorimeters
2145 and the MS to select events up to the maximum-readout rate of the detector
2146 (100 kHz) within a latency of $2.5 \mu\text{s}$. Additionally, the LVL1 identify the
2147 regions of interest (RoI), which includes the position and the p_T of the
2148 candidate objects.

2149 For each event accepted by the LVL1, the Front-End (FE) detector elec-
2150 tronics read the detectors data and pass it to the ReadOut Drivers (ROD).
2151 The ROD performs the initial processing and formatting and the ReadOut
2152 Systems (ROS) buffers this data.

2153 The data from the different sub-detectors is sent from the ROS to the
2154 software-based trigger, the so called “High Level Trigger” (HLT), when is
2155 requested by the HLT. This system is comprised by the second-level trig-
2156 ger (LVL2) and the Event Filter (EF or third-level), both made of several
2157 farms of computers (about 40 000 CPU cores) interconnected by Ethernet
2158 networks. Using modest computing power, LVL2 provides high rejection
2159 power with fast and limited precision algorithms. With higher computing
2160 power, the EF features lower rejection power with slower but higher preci-

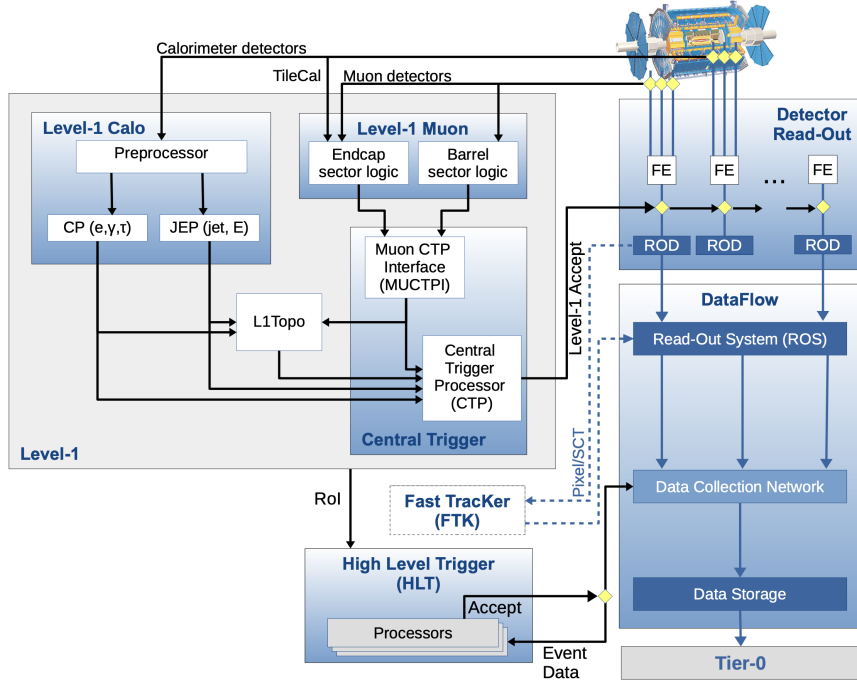


Figure 2.33: The ATLAS TDAQ system in Run-2.

sion algorithms [177]. This combination is a cost-effective and flexible way of implementing the HLT. The ID, which was not used by the LVL1, is of key importance for the HLT because on, one hand, the LVL2 reconstruction algorithms are specifically designed to meet strict timing requirements and, on the other hand, the track reconstruction on the EF is less time constrained. This is done by the ID's Fast TracKer (FTK) as the Figure 2.33 shows.

An average 1.2 kHz output rare for Run-2 pass the HLT (with a latency of just $200\ \mu\text{s}$) and is sent by the Sub-Farm Output (SFO) to the Tier-0 facilities for permanent storage and later offline physics analysis. It is important to highlight that the decisions performed by trigger about whether or not to store an event are irrevocable. If an event does not pass the trigger requirements, it is lost forever.

2.3.7 ATLAS upgrade towards HL-LHC

The LHC Run-3 started on April of this year ([esto está escrito en marzo, así que habrá que ver si es verdad](#)). This is the las data-taking period of the of the collider as it was initially designed. CERN has embarked on a very ambitious project, the High Luminosity Large Hadron Collider (HL-LHC), that will dominate the accelerator-based particle physics scen-



Figure 2.34: Timeline for the LHC and LHC HL projects. The periods of data taking are named Runs and, between runs, there are the Long Shutdowns (LS) in which the different facilities are upgraded.

2180 ario in the years to come. The HL-LHC consists on a luminosity-enhanced
2181 version of the LHC.

2182 Adding more particles to the bunches and focusing more the beam, would
2183 result on a grater collision rate (of about a factor 10). This provides the
2184 different analyses with better statistics, which eventually results in more
2185 precise searches and measurements. A peak instantaneous luminosity of
2186 $\mathcal{L} = 7.5 \times 10^{34} \text{ cm}^2 \text{ s}^{-1}$ is expected, this corresponds to between 140 and
2187 200 inelastic pp collisions per bunch crossing, in contrast to the current 36.1
2188 recorded during last year of Run-2 (Figure 2.10 shows the $\langle\mu\rangle$ for each year
2189 of Run-2).

2190 In contrast to the timeline in Figure 2.34, the latest update of the sched-
2191 ule dates the Long Shutdown 3 (LS3) start in 2026 and the Run-4 start in
2192 2029. All dates are subject to change as the unexpected events may occur
2193 or technical/scientific reasons may lead to re-schedules.

2194 Some technologies developed to upgrade the LHC to HL-LHC are:

- 2195 • Shorter bending dipole magnets are going to be installed. The current
2196 ones have a length of 15 m while the new are only 5.5 m, allowing
2197 the insertion of the colliamtors of Figure 2.35. The new niobium-tin
2198 dipole magnets will generate an 11 T magnetic field compared with
2199 the current 8.3 T.

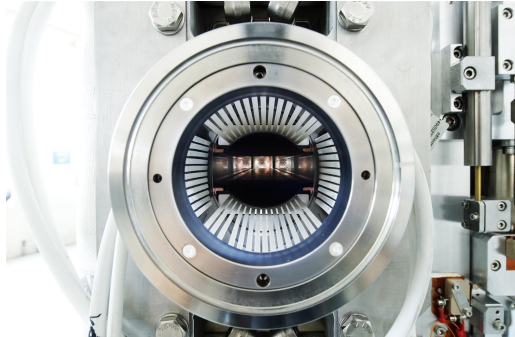


Figure 2.35: HL-LHC Collimator.

- 2200 • Brand new and more powerful superconducting quadrupole magnets
- 2201 (up to 12 T) made of niobium and tin will substitute the current ones
- 2202 (8 T). These magnets will be located at the sides of the ATLAS and
- 2203 CMS detectors
- 2204 • New Beam optics. At present, as bunches cross, the protons collide
- 2205 and disappear and, hence, the luminosity decreases. For the Run-4,
- 2206 in order to keep the luminosity at the same level, the beam focusing
- 2207 is designed to keep the collision rate constant.
- 2208 • Superconducting crab cavities for giving the bunches additional trans-
- 2209 verse momentum in order to increase the probability of collisions.
- 2210 • New collimator sand injection magnets will also improve the perfor-
- 2211 mance of the machine.
- 2212 • Thanks to the new high-temperature superconductors, currents up to
- 2213 10^5 Amperes will be carried over long distances.
- 2214 • New collimators that produce less electromagnetic interference with
- 2215 the beam are being installed. Collimators (Figure 2.35) are important
- 2216 because the machine protection is based on them. This elements of
- 2217 the accelerator absorb particles that stray from the beam trajectory
- 2218 and can harm the devices.
- 2219 • The accelerator chain is improved as well with the use of the linear
- 2220 accelerator LINAC4 and with upgrades in the PSB, PS and PSP.

2221 Although increasing the collision rate of the beams is a crucial goal for
 2222 CERN, improving the accelerator is not enough. The current detectors have
 2223 not been designed for HL-LHC but for the LHC and, thus, cannot handle
 2224 the increased luminosity. By increasing the luminosity while keeping the
 2225 same bunch spacing, a much higher rate of collisions per bunch crossing is

2226 achieved and this implies a higher pile-up. For Run-2, the pile up peaked
2227 around $\mu_{max} \approx 70$ and that was already quite taxing for the system in terms
2228 of tracking and reconstruction, and for Run-4 it may start around 140 and
2229 increase to 200 interactions per bunch crossing.

2230 Next, the main upgrades of the ATLAS detector towards the HL-LHC
2231 project are presented.

2232 **Inner Tracker** The elements in the ID receive a lot of radiation damage
2233 due to the huge rate of particles hitting the detector. This radiation environment
2234 will be even more daunting in the HL project. Therefore, the design
2235 of ATLAS (as well as all other main detectors of LHC) has to be reviewed,
2236 especially for the most central parts of the detector.

2237 To deal with this, ATLAS needs much more capable trackers, therefore,
2238 the entire ID is going to be replaced with a new “inner tracker” (ITk).
2239 This new detector consists of cylinder and end-caps equipped with silicon
2240 detectors covering a geometrical acceptance of $|\eta| < 4$. This expanded
2241 pseudorapidity range introduces many advantages in terms of object recon-
2242 struction and pile-up mitigation by linking objects to the primary vertex
2243 corresponding to the hard-scatter of interest. The new pixel sensors will
2244 be placed very close to the interaction region, where the high fluencies
2245 ($2 \times 10^{16} n_{eq} \text{cm}^{-2}$ in the HL vs the current $10^{15} n_{eq} \text{cm}^{-2}$) have to be tolerated
2246 while maintaining a 96% efficiency of particle detection [165].

2247 As well as the ID, the ITk is divided in two subsystems mounted in
2248 the pixel support tube: the pixel detectors and the strip detectors that
2249 surrounds the pixels. For the strips, there are four barrel layers and six
2250 end-cap petals and for the pixels, five layers are used.

2251 **Calorimeters** Due to radiation tolerance limits, the electronics for the
2252 ECAL and HCAL have to be updated. The on-detector FE electronics
2253 cannot operate with the trigger rates and latencies required for the HL-
2254 LHC luminosities. The FCAL will remain the same as in Run-2.

2255 **Muon Spectrometer** The MS upgrades for the HL-LHC are focused on
2256 the muon trigger chambers. The Level-0 trigger electronics of the RPC and
2257 TCG will be upgraded and for the RPC the pseudorapidity coverage will be
2258 significantly increased. The front-end of the MDT is going to be replaced
2259 as well to address the trigger rate and latency requirements.

2260 **Trigger and Data Acquisition**
 2261 **system** To reconstruct the events
 2262 offline, they have to be recorded in
 2263 the first place, otherwise, it makes
 2264 no sense to have that huge pp col-
 2265 lision rate. This is why while the
 2266 detector hardware is being heavily
 2267 upgraded, a lot of effort is being put
 2268 into the trigger systems. The new
 2269 trigger system is a multistage sys-
 2270 tem that progressively takes more
 2271 and more detailed information and
 2272 each step has more time to make
 2273 this decision. It starts with 40 MHz
 2274 input rate (40^6 input events per
 2275 second). The triggering process
 2276 starts by the Level-0 (Figure 2.36
 2277 in purple) and makes very quick
 2278 decisions ($10\mu s$ latency), reducing
 2279 the rate from 40 to 1 MHz. Af-
 2280 terwards it passes to the event fil-
 2281 ter (Figure 2.36 in orange) which
 2282 takes the 1 MHz down to 10 kHz
 2283 that sends to permanent storage.
 2284 The key part is that these 10 kHz
 2285 are really the most useful 10 kHz
 2286 [179]. For doing so, the perfor-
 2287 mance of the tracking is fundamen-
 2288 tal for things like particle flow identi-
 2289 fication, E_T^{miss} measurements, jet tag-
 2290 ging or tau identification.

2291

2292 **From ATLAS Digest: weekly news – 11 February 2022** "Con-
 2293 cerning the High Luminosity LHC, with the new schedule, LS3 will start in
 2294 2026 and the Run 4 would start in 2029. A new HL-LHC running param-
 2295 eters baseline is under discussion, which leads to new projections foreseeing
 2296 715/fb of pp data collected in Run 4. The beam energy for HL-LHC has
 2297 also been discussed and several scenarios to reach 7 TeV per beam have been
 2298 discussed. The high risk of warm-ups is a main concern and the decision
 2299 will likely be postponed to the end of Run 3. Options to stay at 6.8 TeV or
 2300 even backing off to 6.5 TeV to further avoid warm-ups are still on the table.

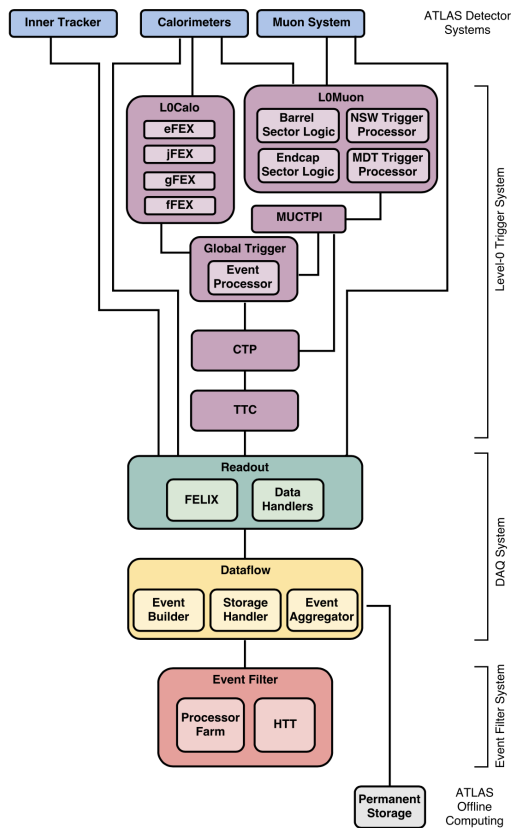


Figure 2.36: Design of the TDAQ Phase-II upgrade architecture, highlighting the organisation of the Upgrade Project in three main systems [179]. Direct connections between each Level-0 trigger component and the Readout system are suppressed for simplicity.

2301 Concerning the Nb3Sn inner triplets, full scale preseries prototypes are in
2302 production."

2303 **2.4 Alignment of the inner detector**

2304 **2.4.1 Alignment requirements**

2305 **2.4.1.1 Local coordinate frame**

2306 **2.4.1.2 Track parameters**

2307 **2.4.1.3 Residuals**

2308 **2.4.2 Track based alignment**

2309 **2.4.2.1 Global χ^2 algorithm**

2310 **2.4.2.2 Weak modes**

2311 **2.4.2.3 Alignment levels and degrees of freedom**

2312 **2.4.3 Alignment results during Run-2**

2313 **Preguntar a Paolo sobre esto**

2314 **2.4.4 Alignment towards Run-3**

2315 **Preguntar a Paolo sobre esto**

2316 **2.4.4.1 Pseudo-real-time-online monitoring**

2317 **Chapter 3**

2318 **Data and simulated events and
2319 object reconstruction**

2320 [180]

2321 **3.1 Data**

2322 Datasets

2323 **3.2 Monte Carlo**

2324 <https://inspirehep.net/literature/856179> In this section I
2325 should describe the generalities of the MC generators and in the
2326 Section4 the specifics for this analysis

2327 From ATLAS Digest: weekly news – 11 March 2022 (use
2328 to write some comments) Reducing negative weights in Sherpa
2329 (Frank Siegert) With the expected very large increase in size of samples
2330 in future runs, Monte Carlo samples will not be able to scale with the accu-
2331 mulated data, as needed for physics performance, without strong develop-
2332 ments in several areas of the simulation. The event generation is projected
2333 to take approximately 20% of the CPU resources and is the single largest
2334 component in CPU consumption of the simulation. It is therefore extremely
2335 important that strategies, that are not just to produce more since it is not
2336 a computationally viable solution to improve on the statistical uncertainty
2337 of the samples, be pursued. Frank discussed the importance of reducing the

2338 fraction of negative weights to improve the effective statistical uncertainty
2339 of weighted samples in Sherpa.

2340 He described a three-fold solution he has proposed in collaboration with
2341 Sherpa co-authors (available here) to reduce the fraction of negative weights.
2342 The three proposed methods correspond to approximations done for (i) the
2343 generation of events with soft emissions (S), (ii) the generation of events
2344 with hard emissions (H) and (iii) the use of a differential K-factor for leading
2345 order Matrix Elements with large numbers of emissions. Reducing negative
2346 weights necessarily leads to approximations and possible biases. Frank de-
2347 scribed in detail a comparison of the three methods. Differences are within
2348 the systematic uncertainties of the produced samples. These methods show
2349 that an improvement in equivalent statistics of a factor of approximately
2350 two can be achieved. **end of ATLAS Digest**

2351 **3.2.1 MC simulations**

2352 The generation of the simulated event samples includes the effect of
2353 multiple pp interactions per bunch crossing, as well as the effect on the
2354 detector response due to interactions from bunch crossings before or after
2355 the one containing the hard interaction.

2356 **3.2.1.1 Parton shower simulation**

2357 **3.2.1.2 Hadronisation simulation**

2358 **3.2.1.3 Underlying decay simulation**

2359 **3.2.1.4 Hadron decay simulation**

2360 **3.2.1.5 Pile-up simulation**

2361 **3.2.2 MC generators**

2362 **3.3 Object reconstruction and identification**

2363 To reconstruct the physical objects, the information of all the sub-
2364 detectors and systems of ATLAS is employed. A detailed description of
2365 all of them is presented in Section 2.3. After passing the trigger preselec-
2366 tion, the raw data is analysed to build the physics objects that constitute

2367 the subject of the physical analyses. The process of constructing this ele-
2368 ments is known as reconstruction. Figure 2.16 illustrates how each particle
2369 interacts with the different layers of the ATLAS detector. The reconstruc-
2370 tion objects are the particles tracks and vertices, the leptons, the photons,
2371 jets (and their flavour tag) and the missing transverse momentum.

2372 **3.3.1 Tracking**

2373 The detection and measurement od charged particles moment is an es-
2374 sential aspect of any large particle physics experiment. Regardless of the
2375 medium through which a charged particle travels, it always leaves a trails
2376 of ionised atoms and liberated electrons. By detecting this it is possible to
2377 reconstruct the trajectory of a charged particle. ATLAS does this trough
2378 its silicon detectors.

2379 The trajectories followed by particles are referred as “tracks”. For
2380 charged particles, the tracks are reconstructed using, mainly, the inform-
2381 ation of the ID and, in the case of muons, the MS. A charged particle
2382 passing thought the ID will interact with its active sensors, the pixel detector
2383 and SCT (Figures 2.22 and 2.23 respectively) providing a three-dimensional
2384 measurement of space-points. While each hit in the pixel detector is directly
2385 translated into a space-point, for the SCT two hits are needed to reconstruct
2386 one space-point. These space-points can be given by a single pixel activa-
2387 tion or by several neighbouring pixels activated simultaneously. Since the
2388 ID is submerged in a solenoidal magnetic field, the charged particles have
2389 their trajectories curved by the Lorentz force, this allows to calculate its p_T
2390 using the sagitta method. The track reconstruction is performed in two s

2391 **Highlight the importance of the alignment for the object defin-
2392 ition and its reconstruction. Link this section with 2.4**

2393 **3.3.1.1 Sagitta method**

2394 **3.3.2 Vertices**

2395 **3.3.3 Electrons and photons**

2396 **3.3.4 Muons**

2397 **3.3.5 Jets**

2398 At accelerator based detectors, quarks and gluons are detected by the
2399 jets of hadronic particles that they produce in the detector soon after they
2400 are created (remember that, as stated in Section 1.1.4, free quarks are sup-
2401 pressed due to color confinement). An exception to this rule are the top
2402 quarks, whose lifetime is smaller than the hadronisation time by two orders
2403 of magnitude and, hence, they are detected by its decay products. For the
2404 gluons and the rest of quarks, hadronisation showers (Section 2.3.3.1) take
2405 place and jet clustering algorithms merge the clusters and tracks produced
2406 by these jets to reconstruct them. In the majority of ATLAS analyses, the
2407 “Anti- k_t ” algorithm is used [181] to analyse the data from hadronic col-
2408 lisions. Modelling the jet as a cone, the algorithm uses a specific choice
2409 of radius parameter (R) defining the radial size of the jet. The distance
2410 between all pairs of objects i and j (d_{ij}) and the distance between the
2411 objects and beam pipe (d_{iB}) are used in:

$$d_{ij} = \min(k_{ti}^{2p}, k_{tj}^{2p}) \frac{\Delta_{ij}^2}{R^2}$$
$$d_{iB} = k_{ti}^{2p}$$

where

$$\Delta_{ij}^2 = (y_i - y_j)^2 - (\phi_i - \phi_j)^2$$

2412 and k_{ti} , y_i and ϕ_i are respectively the transverse momentum, the rapidity
2413 and the azimuthal angle of object i . The parameter p accounts for the
2414 relative power of the energy versus geometrical (Δ_{ij}) scales. For the Anti-
2415 k_t , p is set to -1 . Other clustering algorithms use different choices of p such
2416 as $p = 0$ (Cambridge/Aachen algorithm) or $p = 1$ (inclusive k_t algorithm).

2417 The algorithm iterates over the topological-cluster (or, simply, top-
2418 clusters) objects of the calorimeter as it follows: First it proceeds to identify
2419 the smallest distances with among all the combinations of d_{ij} and d_{iB} . If
2420 the distance is a d_{iB} , the entity i is labeled as “jet” and removed from the

2421 list of entities. If, on the contrary, it is a d_{ij} , the objects i and j are merged
 2422 together. This way, before clustering among themselves, soft components
 2423 (low- p_T) tend to be merged to the hard ones (high- p_T). Then the distances
 2424 are recalculated and the process repeated. This is done iteratively until all
 2425 entities are assigned to a particular jet.

2426 If a hard particle has no hard neighbours within a $2R$ distance, all soft
 2427 particles will be assigned to it, resulting in a perfectly conical jet. But if
 2428 another hard particle is present in that $2R$ distance, then there will be two
 2429 hard jets and it will be impossible for both to be perfectly conical.

2430 **Work in progress**

2431 Typically, the cone size R is selected to be 0.4 or 0.6, though the most
 2432 standard used in ATLAS is 0.4. If $R = 1$, the jet is labeled a Large- R and
 2433 if $R = 0.4$ then as Small- R jet.

2434 **3.3.5.1 Jet energy calibration and resolution**

2435 **3.3.5.2 Bottom quark induced jets**

2436 In general, it is impossible to determine which quark flavour was pro-
 2437 duced or even or whether the jet was originated by a quark or a gluon.
 2438 However, if a b quark is created, the hadronisation will produce a jet of
 2439 hadrons, one of which will be a b -type hadron (B hadron). The B hadrons
 2440 turn out to be relatively-long-lived particles (1.5×10^{-12} s). If this larger
 2441 longevity is combined with the Lorentz time-dilation that particles exper-
 2442 ience when produced in high energy collisions, it results in the B hadron
 2443 traveling on average a few mm before disintegrating.

2444 As a result, the experimental signature of a b quark is a jet of particles
 2445 emerging from the point of collision (primary vertex) and a secondary vertex
 2446 resulting from b -quark decay that is several mm away from the primary
 2447 vertex. Therefore, the capacity to resolve secondary vertices from the parent
 2448 vertex is crucial for identifying b -quark jets.

2449 **3.3.6 Missing transverse energy**

2450 **3.3.7 Overlap removal**

2451 Chapter 4

2452 **Probing the top-quark 2453 polarisation in the single-top 2454 *t*-channel production**

2455 The polarisation paper: [https://atlas-glance.cern.ch/atlas/
2456 analysis/papers/details.php?id=13286](https://atlas-glance.cern.ch/atlas/analysis/papers/details.php?id=13286)

2457 4.1 Introduction

2458 Apart from the studies of the associated production of a top quark and
2459 a Higgs boson, in this thesis is also presented a simultaneous measurement
2460 of the three components of the top-quark and top-antiquark polarisation
2461 vectors in *t*-channel single-top-quark production.

2462 The single-top-quark production and decay via the Wtb vertex, provides
2463 a unique way to study the coupling between the top-quark, the W boson
2464 and the b quarks. This vertex is studied through the measurement of the
2465 polarisation observables for events produced in pp collisions.

2466 Importance of signal selection: In the polarisation analysis we look at an-
2467 gular distributions. The use of a BDT or NN as it is done on the tHq studies
2468 can introduce bias on this angular distribution. This studies are extremely
2469 sensible to any bias introduced on the angular distributions, therefore a
2470 count and cut method for the signal selection is the safest option.

²⁴⁷¹ **4.2 Top quark polarisation observables**

²⁴⁷² **4.3 Simulated event samples**

²⁴⁷³ **4.4 Object reconstruction**

²⁴⁷⁴ **4.5 Trigger requirements and event preselection**

²⁴⁷⁵

²⁴⁷⁶ Chapter 5

²⁴⁷⁷ Search for rare associate tHq ²⁴⁷⁸ production

²⁴⁷⁹ 5.1 Introduction

²⁴⁸⁰ Describe the strategy for the $2\ell + 1\tau_{\text{had}}$ analysis

²⁴⁸¹ The study of the tHq production can be classified attending to the
²⁴⁸² the number of light-flavour leptons (ℓ), i.e. electrons or muons, and
²⁴⁸³ hadronically-decaying tau leptons (τ_{had}). According to this criteria, the
²⁴⁸⁴ channels presented in Table 5.1 have been defined. As can be seen in the
²⁴⁸⁵ table, the study of the 1ℓ channel uses only the $H \rightarrow t\bar{t}$, which is the most
²⁴⁸⁶ dominant decay mode for the Higgs boson with a 58% BR as is reported in
²⁴⁸⁷ Section 1.3.3. However, for the multileptonic channels the $H \rightarrow W^+W^-$,
²⁴⁸⁸ $\rightarrow \tau^-\tau^+$ and $\rightarrow ZZ$ are considered. These three Higgs decay channels
²⁴⁸⁹ combined account for a total 21% BR.

#	0 τ_{had}	1 τ_{had}	2 τ_{had}
$1l (e/\mu)$	$tHq (b\bar{b})$ 1ℓ		$tHq (WW/ZZ/\tau\tau)$ $1\ell + 2\tau_{\text{had}}$
$2l (e/\mu)$	$tHq (WW/ZZ/\tau\tau)$ $2\ell \text{ SS}$	$tHq (WW/ZZ/\tau\tau)$ $2\ell + 1\tau_{\text{had}}$	
$3l (e/\mu)$	$tHq (WW/ZZ/\tau\tau)$ 3ℓ		

Table 5.1: Different channels for tHq production according to the presence of light-flavoured leptons and hadronically-decaying taus in the final state.

Moreover, depending on the relative charge between the light charged leptons, the $2\ell + 1\tau_{\text{had}}$ channel is further subdivided in two sub-channels. The so-called $2\ell \text{SS} + 1\tau_{\text{had}}$ channel is defined by the events in which the two light leptons have the same electric charge. In contrast, the one in which they have opposite electric charge is known as $2\ell \text{OS} + 1\tau_{\text{had}}$ channel. For simplicity, through this document, these two sub-channels are usually referred just as SS and OS respectively.

The work of this thesis is focused in the $2\ell + 1\tau_{\text{had}}$ channels. To do so, the $2\ell \text{SS} + 1\tau_{\text{had}}$ and $2\ell \text{OS} + 1\tau_{\text{had}}$ are treated separately since they have completely different background compositions, being the $2\ell \text{SS} + 1\tau_{\text{had}}$ the one with the lower background contribution.

- different MVAs trained for each channel

When assuming that one of the light-flavoured leptons is originated from the Higgs-boson decay and the other one from the top-quark decay, the determination of which lepton comes from which particle is direct for the $2\ell \text{OS} + 1\tau_{\text{had}}$ but not for the $2\ell \text{SS} + 1\tau_{\text{had}}$. Since knowing the origin of the light-flavoured leptons can be very useful to define variables with the power to discriminate the tHq signal from the background, tools are developed to associate these leptons to its parent particles.

- The fake estimates are being checked to see if there is anything that has to be treated differently for the two sub-channels.

5.2 Data and simulated events

the tH samples were done with MadGraph5_aMC @ NLO++Pythia8+EvtGen

The underlying event is generally done with Pythia8 in ATLAS. In the tHq samples we used MadGraph5_aMC@ NLO for the calculation of the matrix element and Pythia8 for the hadronisation and parton showering. We are also working on alternative samples with Herwig7 as parton shower generator. **While in section 3 I describe how the events and samples are generally generated and simulated, in this section I should describe what is specifically used in this analysis**

2521 5.3 Object definition and reconstruction

2522 5.4 Signal

2523 In this section, it is discussed how it is find what we know as signal.
 2524 In a particular study, the “signal” is the set of events in the dataset that
 2525 correspond to the process of interest. Therefore, in this case, the signal
 2526 is composed by tHq production events with a $2\ell + 1\tau_{\text{had}}$ final state. In
 2527 contrast, the background processes are those which, a priori, look like the
 2528 signal process but it is not.

2529 5.4.1 Signal generation and validation

2530 **rivet**

2531 5.4.2 Parton-level truth validation

2532 > Describe what are truth level and reconstruction level.
 2533 > The truth information is whatever comes from the generator, the
 2534 physics without taking into account the effects of the detector. The truth
 2535 level does not include the effects of the interaction with matter. The truth
 2536 also includes the parton shower and hadronisation information.
 2537 > $\text{truth} = \text{generator} + \text{parton shower} + \text{hadronisation}$
 2538 > The studies I did were done at generator level
 2539 > Particle level is part of truth information
 2540 > Detector level = reconstruction level + calibration +
 2541 > Creo que esto se explica bien en la tesis de florencia
 2542 **(maybe write the calculations of BR_tHq in the Section 5.4.2**
 2543 **)**

2544 5.4.3 Lepton assignment

2545 The two light leptons in the final state of the $2\ell + 1\tau_{\text{had}}$ channel can
 2546 originate either from the Higgs boson or the top quark. The ambiguities
 2547 regarding the origin of these light-flavoured leptons, make the reconstruction
 2548 of the top quark and Higgs boson systems extremely difficult. Nevertheless,

2549 the electric charge of these leptons could provide us useful information to
 2550 probe their origins.

2551 To have knowledge of whether the light-flavoured leptons in the final
 2552 state are originated from the Higgs boson or the top quark is very beneficial
 2553 in order to both reconstruct the event and design variables at reconstruction
 2554 level with high discriminant power. As is show in Sections 5.6.3 and 5.6.4,
 2555 the variables using the lepton assignment information play a relevant role
 2556 not only in the definition of the signal-enriched section but also the in
 2557 the determination of the control regions to constrain the most important
 2558 background processes.

2559 According to the calculations performed by combining the BR of the
 2560 Higgs boson, the top quark and all its decay products (see Section 5.4.2),
 2561 in the $2\ell + 1\tau_{\text{had}}$ channel of tHq production, the τ_{had} is produced 83.7% of
 2562 times as a product of the Higgs-boson decay in opposition to the 16% in
 2563 which it comes from the top-quark disintegration.

2564 **Opposite-sign Leptons**

2565 In the dominant scenario (τ_{had} from Higgs) the association of which light-
 2566 flavoured lepton comes from the top-quark decay and which one comes
 2567 from the Higgs-boson decay can be done directly if these two leptons have
 2568 opposite electric charge, i.e. in the $2\ell \text{OS} + 1\tau_{\text{had}}$ channel. Since in Higgs
 2569 boson is neutrally charged, the sum of the charge of its decay products
 2570 should be zero. Therefore, in the OS channel, while the light lepton with
 2571 opposite charge to that of the τ_{had} is the one coming from the Higgs, the
 2572 other lepton, i.e. the one with the same charge as τ_{had} , is the one originated
 2573 from the top-quark decay.

2574 **Same-sign Leptons**

2575 In contrast to the the $2\ell \text{OS} + 1\tau_{\text{had}}$ channel, in the case of τ_{had} from Higgs,
 2576 when the two light leptons have the same electric charge (the so called
 2577 $2\ell \text{SS} + 1\tau_{\text{had}}$) it is not possible to know, a priori, which of the leptons
 2578 comes from the top-quark system and which from the Higgs-boson decay.

2579 In order to perform this association for the $2\ell \text{SS} + 1\tau_{\text{had}}$ several methods
 2580 relying in the truth-level information have been tested. **Describir superficialmente los métodos listados en el ítemize**

- 2582 • First method (Cyrus): Assume that the leading lepton was originated
 2583 from the top
- 2584 • Second method (Mathias): Cut in two variables

- 2585 – Cut 1: $m_{vis,H}(lep(t)) - m_{vis,H}(lep(H)) > 57.0 \text{ GeV}$
 2586 – Cut 2: $m_{pred,t}(lep(H)) - m_{pred,t}(lep(t)) > 0.0 \text{ GeV}$
- 2587 • BDT based method presented in this work

2588 **5.4.3.1 Labelling the $2\ell \text{ SS} + 1\tau_{\text{had}}$ with the reconstruction-level
 2589 and truth-level matching**

2590 Even though at reconstruction level it is not known which are the par-
 2591 ents of the particles in the final state, at parton level this informations is
 2592 accesible, in other words, the origin¹ of the light leptons is known. For a
 2593 given event, it is possible to access to both the particle-level and parton-level
 2594 information simultaneously. Having the parton-level leptons, whose parents
 2595 are known, and the reconstruction level leptons, whose parents need to be
 2596 identified, it is possible to compare them to create an association. Specific-
 2597 ally, identify which parton-level lepton correspond to which reconstructed
 2598 lepton. The aim of this relation is to assign the leading (ℓ_1) and sub-leading
 2599 (ℓ_2) light leptons at reconstruction level to the the “lepton from top-quark-
 2600 decay chain” (ℓ_{top}) and “lepton from Higgs-boson-decay chain” (ℓ_{Higgs}) at
 2601 truth level.

2602 In order to link the reconstruction-level light leptons to the parton-level
 2603 light leptons, a $\Delta R < 0.01$ cone around each of the reconstructed leptons
 2604 is built. When inside that cone there one and only one truth-level light
 2605 lepton, there is what is called “a match”. Figure 5.1 presents the possibles
 2606 scenarios of the association. In order to identify properly determine the
 2607 lepton origin in an event, it is required that both leptons at reconstruction
 2608 level have a match. There are two different cases for this. The first situation
 2609 is that in which the leading-light lepton is ℓ_{top} and the sub-leading is ℓ_{Higgs} .
 2610 For the sake of simplicity, this configuration is named Type 1 and it is
 2611 represented in Figure 5.1a. The second double-matching combination is the
 2612 other way around, the leading-light lepton is ℓ_{Higgs} and the sub-leading is
 2613 ℓ_{top} . Pictured in Figure 5.1b, this type of events are called Type 2. On
 2614 the contrary, if only one of the two reconstructed light leptons is matched
 2615 (Figure 5.1c), none of the leptons are classified. If a less strict criteria was
 2616 used, it would be possible requiere only one of the two leptons matching in
 2617 order to classify the event (the unmatched reconstruction-level lepton would
 2618 be assigned to the unmatched parton-level lepton). The problem of the lax
 2619 strategy is that while in cases like that on Figure 5.1c it seems clear that
 2620 unmatched parton correspond to the unmatched reconstructed lepton, for

¹By origin of a light lepton is meant whether it comes from the Higgs-boson-decay chain or the top-quark-decay chain.

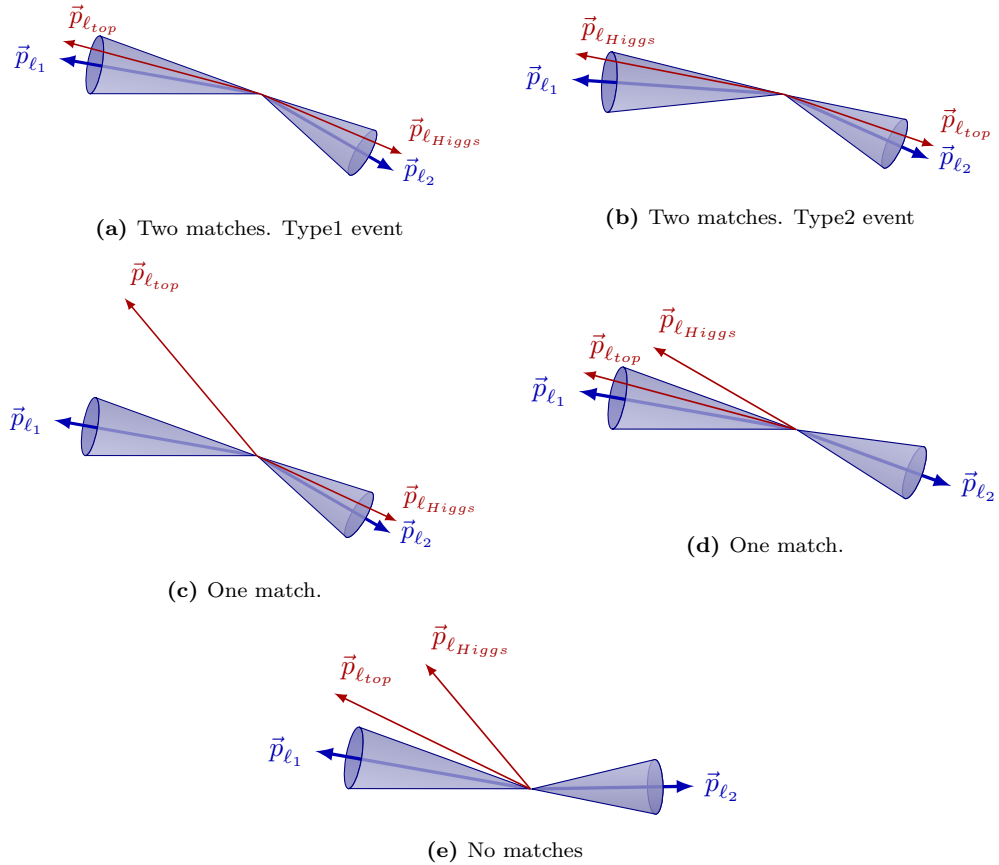


Figure 5.1: Association between reconstruction-level (blue) and parton-level (red) light leptons. Note that the labels ℓ_{top} and ℓ_{Higgs} are only available for the parton-level particles.

events such as the illustrated in Figure 5.1d the unmatched particle does not necessarily belong to the ℓ_2 cone. For this reason, it is mandatory that both reconstructed light leptons have a match. Finally, in the scenario in which none of the parton-level leptons fall into the cones (Figure 5.1e), no assignation takes place.

To perform this labelling, it has been required that the τ_{had} is originated in from the Higgs-boson system. This is imposed in order to guarantee that there are both a ℓ_{top} and a ℓ_{Higgs} . The Higgs-decay channels used for these studies are the $H \rightarrow \tau\tau$ (one τ decaying leptonically and the other hadronically) and the $H \rightarrow WW$. The $H \rightarrow ZZ$ channel has not been included since its impact in the on the $2\ell + 1\tau_{had}$ production when the τ_{had} comes from the Higgs is very tiny. If the τ_{had} is originated in the Higgs system, only a 2.0% of the events correspond to the $H \rightarrow ZZ$ decay channel, contrasting with the 76.5% of the $H \rightarrow \tau\tau$ and the 21.5% of the $H \rightarrow WW$.

2635 Should add the fraction of events that are labeled from a) the
2636 total $2\ell + 1\tau_{\text{had}}$ sample and b) from the total $2\ell \text{ SS} + 1\tau_{\text{had}}$.

2637 **5.4.3.2 BDT-based method for lepton association**

2638 **5.4.4 Top quark and Higgs boson reconstruction**

2639 En aras de que esto es extremadamente complicado y no se
2640 logró hacer ¿tiene sentido redactar una sección?

2641 **5.5 Background estimation**

2642 The background can be defined as everything in a subset of the data that
2643 simulates the signal processes without truly being a signal event. In other
2644 words, in this studies, everything that is not signal, is background. In this
2645 case, whatever that mimics the signature of an associated tHq production
2646 with $2\ell + 1\tau_{\text{had}}$ final state is re referred as background.

2647 Signal (aka needle). -> Several needels Background (aka haystack) ->
2648 Several types of haystacks

2649 The main source of background in the $2\ell + 1\tau_{\text{had}}$ channel is due to jets
2650 faking τ_{had} **poner las figuras de oleh**

2651 **5.5.1 Fakes estimation**

2652 tau fakes are more important than light lepton fakes

2653 **This is taken from the intNote. I have to reorganise and rephrase this information** The requirements for the objets defined in section
2654 (ref ref) provide significant suppression of events with jets wrongly selec-
2655 ted as leptons is achieved by asking electrons and muons to pass the tight
2656 requirement that combines `tightLH` ID for leptons and `medium` for muons
2657 and `PLImprovedTight` isolation working points

2659 Similarly, the hadronic taus are required to pass the `medium` require-
2660 ment of the RNN-based discriminator. Even so, the selected data sample
2661 is expected to be contaminated with such type of reducible background. It
2662 is also expected that the simulation of jets faking leptons (electron, muon,
2663 hadronic tau) in ATLAS detector is imprecise or unreliable. Therefore, an
2664 important step of the analysis is to estimate this background in data.

2665 **Light lepton fakes** Particles in the Feynman diagram are referred as
 2666 ‘prompt’ or ‘real’. Acceptance, quality and isolation requirements are ap-
 2667 plied to select these leptons Non-prompt leptons and non-leptonic particles
 2668 may satisfy these selection criteria, giving rise to so called ‘non-prompt and
 2669 fake’ lepton backgrounds. Fake electrons/muons will not be explicitly dis-
 2670 tinguished and are referred as fake leptons. The mis-identified lepton back-
 2671 ground arises from heavy-flavour (HF) decay leptons and electrons from
 2672 γ -conversions. These leptons are mainly produced in $t\bar{t}$, $Z + \text{jets}$ and tW
 2673 events.

2674 The estimation of the fake/non-prompt lepton background is done with
 2675 the template fit method or via the matrix method

2676 The fake and real lepton efficiencies (fake/real rates) are defined as the
 2677 probabilities of a fake or real electron or muon to pass the nominal elec-
 2678 tron/muon requirements. They are given by the tight over loose ratio

2679 - Get some ideas from here: [https://cds.cern.ch/record/1951336/
 2680 files/ATLAS-CONF-2014-058.pdf](https://cds.cern.ch/record/1951336/files/ATLAS-CONF-2014-058.pdf)

2681 **Tau fakes** In the analysis channels involving hadronic taus, all meth-
 2682 ods used for fake background estimation rely on MC-based templates.
 2683 These are splits of simulation according to a type of object mimicking the
 2684 lepton of interest. Construction of MC templates related to the electron
 2685 and muon fakes is based on **IFFTruthClassifier** tool. **Describe the**
 2686 **IFFTruthClassifier**

- 2687 • counting method
- 2688 • template fit method

2689 The extracted SFs are then applied to the simulated background com-
 2690 ponent in the region with taus passing I

2691 5.5.2 Prompt backgrounds

2692 All the processes whose signature is the same as the process of interest
 2693 are known as prompt backgrounds as in contrast to the fake or non-prompt
 2694 backgrounds described in Section 5.5.1.

Process	SS	OS	SS + OS
tHq	0.9	1.2	2.1
tZq	6.2	32.9	39.1
$t\bar{t}$	47.9	2965.0	3012.9
tW	2.3	118.9	121.2
$W + \text{jets}$	1.9	0.5	2.4
$Z + \text{jets}$	6.7	1956.2	1962.9
diboson	8.9	121.6	130.5
$t\bar{t}W$	21.0	43.4	64.4
$t\bar{t}Z$	17.5	101.2	118.7
$t\bar{t}H$	17.8	43.2	61.0
tWZ	3.1	16.4	19.5
tWH	0.6	1.5	2.1
Other	1.9	9.3	11.2
Total	136.7	5411.3	5548.0
S/B (%)	0.6627	0.0222	0.0379
Significance	0.0771	0.0163	0.0282

Table 5.2: Event yields at preselection level for SS, OS and SS+OS combination.

2695 **5.6 Event selection**

2696 **5.6.1 Preselection**

2697 Preselection requirements

2698 **5.6.2 BDT**

2699 Since a BDT is going to be used for both the lepton assign-
 2700 ment al region definition, it may be interesting to describe the
 2701 technicalities of the BDT in an appendix

2702 Maybe, it can also be a good idea to explain the generalities of
 2703 the BDT for region definition here and then put the BDT results
 2704 into "Signal Region" and "Control Regions" section.

2705 **5.6.2.1 Performance**

2706 **5.6.2.2 Ranking of variables**

2707 **5.6.2.3 Hyperparameter optimisation**

2708 **Grid search**

2709 **Genetic algorithm**

2710 **5.6.2.4 Negative-weights strategy**

2711 **5.6.2.5 k-Folding**

2712 **5.6.3 Signal Region**

2713 **5.6.3.1 Same Sign channel**

2714 **5.6.3.2 Oposite Sign channel**

2715 **5.6.4 Control Regions**

2716 **5.6.4.1 Same Sign channel**

2717 $t\bar{t}$

2718 $t\bar{t}W$

2719 $t\bar{t}Z$

2720 $t\bar{t}H$

2721 **5.6.4.2 Oposite Sign channel**

2722 $t\bar{t}$

2723 $Z +\text{jets}$

2724 **Diboson**

2725 **tW**

2726 **5.7 Systematic uncertainties**

2727 Alternative samples are produced to evaluate the systematics: - Herwig7
2728 -> parton shower
2729 - asdfas. -> modelling

2730

²⁷³¹ **5.7.1 Theoretical uncertainties**

²⁷³² **5.7.2 Modelling uncertainties**

²⁷³³ **5.7.3 Experimental uncertainties**

²⁷³⁴ **5.8 Fit results**

²⁷³⁵ **5.8.1 Strategy**

²⁷³⁶ **5.8.2 Fit with Asimov data**

²⁷³⁷ **5.8.2.1 Post-fit**

²⁷³⁸ **5.8.2.2 Pruning**

²⁷³⁹ **5.8.2.3 Nuisance Parameters**

²⁷⁴⁰ **5.8.2.4 Correlation matrix**

²⁷⁴¹ **5.8.2.5 Ranking**

²⁷⁴² **5.8.3 Fit to data**

²⁷⁴³ **5.8.3.1 Post-fit**

²⁷⁴⁴ **5.8.3.2 Pruning**

²⁷⁴⁵ **5.8.3.3 Nuisance Parameters**

²⁷⁴⁶ **5.8.3.4 Correlation matrix**

²⁷⁴⁷ **5.8.3.5 Ranking**

²⁷⁴⁸ **5.8.4 Results**

²⁷⁴⁹ **5.8.5 Data fit**

²⁷⁵⁰ **5.9 Combination results**

²⁷⁵¹ **Discuss results, compare them with CMS, future perspectives**

²⁷⁵² ...

₂₇₅₃ **5.10 Conclusions**

²⁷⁵⁴ Chapter 6

²⁷⁵⁵ Conclusion

2756 **Abbreviations**

2757

Acronym	Meaning
AD	Antiproton Decelerator
ALICE	A Large Ion Collider Experiment
ATLAS	A Toroidal LArge AparatuS
AWAKE	Advanced Proton Driven Plasma Wakefield Acceleration Experiment
CERN	European Organization for Nuclear Research
CMS	Compact Muon Solenoid
CP	Charge conjugation Parity
CSC	Cathode-Strip Chambers
DAQ	Data Acquisition
ECAL	Electromagnetic Calorimeter
EF	Event Filter
EM	Electromagnetic
EW	Electro Weak
EWSB	Electroweak Symmetry Breaking
FASER	ForwArd Search ExpeRiment
FCAL	Forward calorimeter
FTK	Fast TracKer
GR	General Relativity
HCAL	Hadronic Calorimeter
HLT	High Level Trigger
IBL	Insertable B-Layer
IP	Interaction Point

Acronym	Meaning
IR	Insertion Regions
ISOLDE	On-Line Isotope Mass Separator
ITk	Inner Tracker
LAr	Liquid Argon
LCG	LHC Computing Grid
LEIR	Low Energy Ion Ring
LEP	Large Electron-Positron
LHC	Large Hadron Collider
LHCb	The Large Hadron Collider Beauty
LHCf	Large Hadron Collider forward
LINAC2	Linear Accelerator 2
LINAC3	Linear Accelerator 3
LINAC4	Linear Accelerator 4
2758	LO
	Leading Order
	LVL1
	Level-1 Trigger
	LVL2
MATHUSLA	Massive Timing Hodoscope for Ultra Stable neutrAL pArticles
MDT	Monitored Drift Tube
MoEDAL	Monopole and exotic particle detector at the LHC
MS	Muon Spectrometer
NLO	Next-to-Leading Order
NNLO	Next-to-Next-to-Leading Order
PDF	Parton Distribution Function
PS	Proton Synchrotron
PSB	Proton Synchrotron Booster
QCD	Quantum Chromodynamics
QED	Quantum Electrodynamics
QFT	Quantum Field Theory

2759

Acronym	Meaning
RF	Radio Frequency
ROD	ReadOut Drivers
RoI	Regions of interest
ROS	ReadOut Systems
RPC	Resistive Plate Chambers
SCT	Semiconductor Tracker
SFO	Sub-Farm Output
SM	Standar Model
SPS	Super Proton Synchrotron
SSB	Spontaneus Symmetry Breakin
SSC	Superconducting Super Collider
SUSY	Supersimmetry
TGC	Thin Gap Chambers
TI	Transfer Injection

²⁷⁶⁰

Bibliography

- ²⁷⁶¹ ¹Particle Data Group Web Page, *top-quark Mass (Direct Measurements)*,
²⁷⁶² (2022) <https://pdglive.lbl.gov/DataBlock.action?node=Q007TP>
²⁷⁶³ (visited on 22/01/2022) (cit. on pp. v, 33).
- ²⁷⁶⁴ ²Particle Data Group Web Page, *Higgs-boson Mass*, (2022)
<https://pdglive.lbl.gov/DataBlock.action?node=S126M> (visited
²⁷⁶⁵ on 22/01/2022) (cit. on pp. v, 45).
- ²⁷⁶⁶ ³Online Etymology Dictionary, "Physics", (2022)
<https://www.etymonline.com/word/physics> (visited on 20/01/2022)
²⁷⁶⁷ (cit. on p. 1).
- ²⁷⁶⁸ ⁴Perseus Digital Library, "fusiko", (2022)
<https://www.perseus.tufts.edu/hopper/text?doc=Perseus:text:1999.04.0057:entry=fusiko/s> (visited on 20/01/2022) (cit. on p. 1).
- ²⁷⁶⁹ ⁵C Singer, *A Short History of Science to the Nineteenth Century*, p. 35.
(Streeter Press, 2008) (cit. on p. 1).
- ²⁷⁷⁰ ⁶C. C. W. Taylor et al., *The atomists, leucippus and democritus: fragments: a text and translation with a commentary*, Vol. 5
(University of Toronto Press, 2010) (cit. on p. 1).
- ²⁷⁷¹ ⁷O. Leaman, *Key concepts in eastern philosophy* (Routledge, 2002)
(cit. on p. 1).
- ²⁷⁷² ⁸A. Einstein, *The Foundation of the General Theory of Relativity*,
Annalen Phys. **49** (1916) 769–822, edited by J.-P. Hsu and D. Fine
(1916) (cit. on p. 2).
- ²⁷⁷³ ⁹P. A. M. Dirac, *On the theory of quantum mechanics*,
Proceedings of the Royal Society of London. Series A, Containing
Papers of a Mathematical and Physical Character **112** (1926) 661–677
(1926) (cit. on p. 3).
- ²⁷⁷⁴ ¹⁰R. Aaij et al., *Observation of a narrow pentaquark state, $P_c(4312)^+$, and
of two-peak structure of the $P_c(4450)^+$* ,
Phys. Rev. Lett. **122** (2019) 222001 (2019) (cit. on p. 4).

- ²⁷⁹⁰ ¹¹A. Pich, ‘The Standard model of electroweak interactions’,
²⁷⁹¹ 2006 European School of High-Energy Physics (2007) 1
²⁷⁹² (cit. on pp. 4, 16).
- ²⁷⁹³ ¹²E. Noether, *Invariante variationsprobleme*, ger,
²⁷⁹⁴ Nachrichten von der Gesellschaft der Wissenschaften zu Göttingen,
²⁷⁹⁵ Mathematisch-Physikalische Klasse **1918** (1918) 235–257 (1918)
²⁷⁹⁶ (cit. on p. 6).
- ²⁷⁹⁷ ¹³C. A. Moura and F. Rossi-Torres, *Searches for Violation of CPT Symmetry and Lorentz Invariance with Astrophysical Neutrinos*,
²⁷⁹⁸ *Universe* **8** (2022) 42 (2022) (cit. on p. 9).
- ²⁸⁰⁰ ¹⁴J. S. Bell, *Time reversal in field theory*,
²⁸⁰¹ *Proc. Roy. Soc. Lond. A* **231** (1955) 479–495 (1955) (cit. on p. 9).
- ²⁸⁰² ¹⁵R. F. Streater and A. S. Wightman,
²⁸⁰³ *PCT, spin and statistics, and all that* (1989) (cit. on p. 9).
- ²⁸⁰⁴ ¹⁶T. D. Lee and C.-N. Yang,
²⁸⁰⁵ *Question of Parity Conservation in Weak Interactions*,
²⁸⁰⁶ *Phys. Rev.* **104** (1956) 254–258 (1956) (cit. on p. 9).
- ²⁸⁰⁷ ¹⁷C. S. Wu, E. Ambler, R. W. Hayward, D. D. Hoppes and R. P. Hudson,
²⁸⁰⁸ *Experimental Test of Parity Conservation in β Decay*,
²⁸⁰⁹ *Phys. Rev.* **105** (1957) 1413–1414 (1957) (cit. on p. 9).
- ²⁸¹⁰ ¹⁸R. L. Garwin, L. M. Lederman and M. Weinrich,
²⁸¹¹ *Observations of the failure of conservation of parity and charge conjugation in meson decays: the magnetic moment of the free muon*,
²⁸¹² *Phys. Rev.* **105** (4 1957) 1415–1417 (1957) (cit. on p. 10).
- ²⁸¹⁴ ¹⁹J. H. Christenson, J. W. Cronin, V. L. Fitch and R. Turlay,
²⁸¹⁵ *Evidence for the 2π Decay of the K_2^0 Meson*,
²⁸¹⁶ *Phys. Rev. Lett.* **13** (1964) 138–140 (1964) (cit. on p. 10).
- ²⁸¹⁷ ²⁰L.-L. Chau and W.-Y. Keung,
²⁸¹⁸ *Comments on the Parametrization of the Kobayashi-Maskawa Matrix*,
²⁸¹⁹ *Phys. Rev. Lett.* **53** (1984) 1802 (1984) (cit. on p. 11).
- ²⁸²⁰ ²¹J. Hardy and I. Towner, $|V_{ud}|$ from nuclear β decays,
²⁸²¹ *PoS CKM2016* (2017) 028 (2017) (cit. on p. 12).
- ²⁸²² ²²D. Pocanic et al.,
²⁸²³ *Precise measurement of the $\pi^+ \rightarrow \pi^0 e^+ \nu$ branching ratio*,
²⁸²⁴ *Phys. Rev. Lett.* **93** (2004) 181803 (2004) (cit. on p. 12).
- ²⁸²⁵ ²³R. E. Shrock and L.-L. Wang,
²⁸²⁶ *New, generalized cabibbo fit and application to quark mixing angles in the sequential weinberg-salam model*,
²⁸²⁷ *Phys. Rev. Lett.* **41** (25 1978) 1692–1695 (1978) (cit. on p. 12).

- ²⁸²⁹²⁴N. Cabibbo, E. C. Swallow and R. Winston,
²⁸³⁰*Semileptonic hyperon decays and CKM unitarity,*
²⁸³¹*Phys. Rev. Lett.* **92** (2004) 251803 (2004) (cit. on p. 12).
- ²⁸³²²⁵S. Aoki et al.,
²⁸³³*FLAG Review 2019: Flavour Lattice Averaging Group (FLAG),*
²⁸³⁴*Eur. Phys. J. C* **80** (2020) 113 (2020) (cit. on p. 12).
- ²⁸³⁵²⁶J. P. Lees et al.,
²⁸³⁶*Measurement of the $D^0 \rightarrow \pi^- e^+ \nu_e$ differential decay branching fraction*
²⁸³⁷*as a function of q^2 and study of form factor parameterizations,*
²⁸³⁸*Phys. Rev. D* **91** (2015) 052022 (2015) (cit. on p. 12).
- ²⁸³⁹²⁷D. Besson et al., *Improved measurements of D meson semileptonic*
²⁸⁴⁰*decays to π and K mesons*, *Phys. Rev. D* **80** (2009) 032005 (2009)
(cit. on p. 12).
- ²⁸⁴²²⁸A. Kayis-Topaksu et al.,
²⁸⁴³*Measurement of topological muonic branching ratios of charmed hadrons*
²⁸⁴⁴*produced in neutrino-induced charged-current interactions,*
²⁸⁴⁵*Phys. Lett. B* **626** (2005) 24–34 (2005) (cit. on p. 12).
- ²⁸⁴⁶²⁹P. del Amo Sanchez et al., *Measurement of the Absolute Branching*
²⁸⁴⁷*Fractions for $D_s^- \rightarrow \ell^- \bar{\nu}_\ell$ and Extraction of the Decay Constant f_{D_s} ,*
²⁸⁴⁸*Phys. Rev. D* **82** (2010) 091103, [Erratum: *Phys. Rev. D* 91, 019901
(2015)] (2010) (cit. on p. 12).
- ²⁸⁵⁰³⁰L. Widhalm et al., *Measurement of $D0 \rightarrow \pi l \nu$ ($Kl \nu$) Form*
²⁸⁵¹*Factors and Absolute Branching Fractions,*
²⁸⁵²*Phys. Rev. Lett.* **97** (2006) 061804 (2006) (cit. on p. 12).
- ²⁸⁵³³¹Y. S. Amhis et al.,
²⁸⁵⁴*Averages of b -hadron, c -hadron, and τ -lepton properties as of 2018,*
²⁸⁵⁵*Eur. Phys. J. C* **81** (2021) 226 (2021) (cit. on p. 12).
- ²⁸⁵⁶³²A. Abdesselam et al., *Precise determination of the CKM matrix element*
²⁸⁵⁷ *$|V_{cb}|$ with $\bar{B}^0 \rightarrow D^{*+} \ell^- \bar{\nu}_\ell$ decays with hadronic tagging at Belle*, (2017)
²⁸⁵⁸ (2017) (cit. on p. 12).
- ²⁸⁵⁹³³J. P. Lees et al., *Study of $\bar{B} \rightarrow X_u \ell \bar{\nu}$ decays in $B\bar{B}$ events tagged by a*
²⁸⁶⁰*fully reconstructed B -meson decay and determination of $\|V_{ub}\|$,*
²⁸⁶¹*Phys. Rev. D* **86** (2012) 032004 (2012) (cit. on p. 12).
- ²⁸⁶²³⁴B. Colquhoun, R. J. Dowdall, J. Koponen, C. T. H. Davies and
²⁸⁶³G. P. Lepage,
²⁸⁶⁴ *$B \rightarrow \pi \ell \nu$ at zero recoil from lattice QCD with physical u/d quarks,*
²⁸⁶⁵*Phys. Rev. D* **93** (2016) 034502 (2016) (cit. on p. 12).
- ²⁸⁶⁶³⁵C. W. Bauer, Z. Ligeti and M. E. Luke,
²⁸⁶⁷*A Model independent determination of $|V(ub)|$,*
²⁸⁶⁸*Phys. Lett. B* **479** (2000) 395–401 (2000) (cit. on p. 12).

- ²⁸⁶⁹³⁶R Aaij et al., *Precision measurement of the B_s^0 - \bar{B}_s^0 oscillation frequency*
²⁸⁷⁰*with the decay $B_s^0 \rightarrow D_s^- \pi^+$* , *New J. Phys.* **15** (2013) 053021 (2013)
²⁸⁷¹(cit. on p. 12).
- ²⁸⁷²³⁷M. Misiak et al.,
²⁸⁷³*Updated NNLO QCD predictions for the weak radiative B -meson decays*,
²⁸⁷⁴*Phys. Rev. Lett.* **114** (2015) 221801 (2015) (cit. on p. 12).
- ²⁸⁷⁵³⁸T. A. Aaltonen et al., *Tevatron Combination of Single-Top-Quark Cross*
²⁸⁷⁶*Sections and Determination of the Magnitude of the*
²⁸⁷⁷*Cabibbo-Kobayashi-Maskawa Matrix Element \mathbf{V}_{tb}* ,
²⁸⁷⁸*Phys. Rev. Lett.* **115** (2015) 152003 (2015) (cit. on p. 12).
- ²⁸⁷⁹³⁹V. Khachatryan et al., *Search for the associated production of a Higgs*
²⁸⁸⁰*boson with a single top quark in proton-proton collisions at $\sqrt{s} = 8$ TeV*,
²⁸⁸¹*JHEP* **06** (2016) 177 (2016) (cit. on pp. 12, 53).
- ²⁸⁸²⁴⁰V. M. Abazov et al., *Precision measurement of the ratio*
²⁸⁸³ *$B(t \rightarrow Wb)/B(t \rightarrow Wq)$ and Extraction of V_{tb}* ,
²⁸⁸⁴*Phys. Rev. Lett.* **107** (2011) 121802 (2011) (cit. on p. 12).
- ²⁸⁸⁵⁴¹P. A. Zyla et al., *Review of Particle Physics*,
²⁸⁸⁶*PTEP* **2020** (2020) 083C01 (2020) (cit. on p. 12).
- ²⁸⁸⁷⁴²P. Q. Hung, *The Weak Eightfold Way: $SU(3)_W$ unification of the*
²⁸⁸⁸*electroweak interactions*, (2021) (2021) (cit. on p. 11).
- ²⁸⁸⁹⁴³A. M. Sirunyan et al.,
²⁸⁹⁰*Measurement of the weak mixing angle using the forward-backward*
²⁸⁹¹*asymmetry of Drell-Yan events in pp collisions at 8 TeV*,
²⁸⁹²*Eur. Phys. J. C* **78** (2018) 701 (2018) (cit. on p. 14).
- ²⁸⁹³⁴⁴O. W. Greenberg, *Spin and Unitary Spin Independence in a Paraquark*
²⁸⁹⁴*Model of Baryons and Mesons*, *Phys. Rev. Lett.* **13** (1964) 598–602
²⁸⁹⁵(1964) (cit. on p. 15).
- ²⁸⁹⁶⁴⁵D. D. Ryutov, *Using Plasma Physics to Weigh the Photon*,
²⁸⁹⁷*Plasma Phys. Control. Fusion* **49** (2007) B429 (2007) (cit. on p. 19).
- ²⁸⁹⁸⁴⁶F. J. Yndurain, *Limits on the mass of the gluon*,
²⁸⁹⁹*Phys. Lett. B* **345** (1995) 524–526 (1995) (cit. on p. 19).
- ²⁹⁰⁰⁴⁷M. Aaboud et al., *Measurement of the W -boson mass in pp collisions at*
²⁹⁰¹ *$\sqrt{s} = 7$ TeV with the ATLAS detector*,
²⁹⁰²*Eur. Phys. J. C* **78** (2018) 110, [Erratum: *Eur.Phys.J.C* 78, 898 (2018)]
²⁹⁰³(2018) (cit. on p. 20).
- ²⁹⁰⁴⁴⁸G. Abbiendi et al., *Precise determination of the Z resonance parameters*
²⁹⁰⁵*at LEP: 'Zedometry'*, *Eur. Phys. J. C* **19** (2001) 587–651 (2001)
²⁹⁰⁶(cit. on p. 20).

- 2907 ⁴⁹J. Goldstone, A. Salam and S. Weinberg, *Broken Symmetries*,
2908 Phys. Rev. **127** (1962) 965–970 (1962) (cit. on p. 21).
- 2909 ⁵⁰D. M. Webber et al., *Measurement of the Positive Muon Lifetime and*
2910 *Determination of the Fermi Constant to Part-per-Million Precision*,
2911 Phys. Rev. Lett. **106** (2011) 041803 (2011) (cit. on p. 26).
- 2912 ⁵¹M. Aker et al.,
2913 *Direct neutrino-mass measurement with sub-electronvolt sensitivity*,
2914 Nature Phys. **18** (2022) 160–166 (2022) (cit. on p. 27).
- 2915 ⁵²N. Aghanim et al., *Planck 2018 results. VI. Cosmological parameters*,
2916 Astron. Astrophys. **641** (2020) A6, [Erratum: Astron.Astrophys. 652,
2917 C4 (2021)] (2020) (cit. on p. 29).
- 2918 ⁵³V. C. Rubin and W. K. Ford Jr., *Rotation of the Andromeda Nebula*
2919 *from a Spectroscopic Survey of Emission Regions*,
2920 Astrophys. J. **159** (1970) 379–403 (1970) (cit. on p. 30).
- 2921 ⁵⁴A. N. Taylor, S. Dye, T. J. Broadhurst, N. Benitez and E. van Kampen,
2922 *Gravitational lens magnification and the mass of abell 1689*,
2923 Astrophys. J. **501** (1998) 539 (1998) (cit. on pp. 30, 33).
- 2924 ⁵⁵P. A. R. Ade et al., *Planck 2015 results. XIII. Cosmological parameters*,
2925 Astron. Astrophys. **594** (2016) A13 (2016) (cit. on p. 30).
- 2926 ⁵⁶M. Aaboud et al.,
2927 *Measurement of the top quark mass in the $t\bar{t} \rightarrow \text{lepton+jets}$ channel*
2928 *from $\sqrt{s} = 8$ TeV ATLAS data and combination with previous results*,
2929 Eur. Phys. J. C **79** (2019) 290 (2019) (cit. on p. 33).
- 2930 ⁵⁷A. M. Sirunyan et al.,
2931 *Measurement of the Jet Mass Distribution and Top Quark Mass in*
2932 *Hadronic Decays of Boosted Top Quarks in pp Collisions at $\sqrt{s} = \text{TeV}$* ,
2933 Phys. Rev. Lett. **124** (2020) 202001 (2020) (cit. on p. 33).
- 2934 ⁵⁸Combination of CDF and D0 results on the mass of the top quark using
2935 up 9.7 fb^{-1} at the Tevatron, (2016) (2016) (cit. on p. 33).
- 2936 ⁵⁹M. Kobayashi and T. Maskawa,
2937 *CP Violation in the Renormalizable Theory of Weak Interaction*,
2938 Prog. Theor. Phys. **49** (1973) 652–657 (1973) (cit. on p. 34).
- 2939 ⁶⁰J. E. Augustin et al.,
2940 *Discovery of a Narrow Resonance in e^+e^- Annihilation*,
2941 Phys. Rev. Lett. **33** (1974) 1406–1408 (1974) (cit. on p. 34).
- 2942 ⁶¹S. W. Herb et al., *Observation of a Dimuon Resonance at 9.5-GeV in*
2943 *400-GeV Proton-Nucleus Collisions*,
2944 Phys. Rev. Lett. **39** (1977) 252–255 (1977) (cit. on p. 34).

- ²⁹⁴⁵⁶²F. Abe et al., *Observation of top quark production in $\bar{p}p$ collisions*,
²⁹⁴⁶*Phys. Rev. Lett.* **74** (1995) 2626–2631 (1995) (cit. on p. 34).
- ²⁹⁴⁷⁶³S. Abachi et al., *Observation of the top quark*,
²⁹⁴⁸*Phys. Rev. Lett.* **74** (1995) 2632–2637 (1995) (cit. on p. 34).
- ²⁹⁴⁹⁶⁴M. Czakon and A. Ferroglio, *Chinese Physics C* () 083104
²⁹⁵⁰(cit. on p. 35).
- ²⁹⁵¹⁶⁵P. Kant et al., *HatHor for single top-quark production: Updated*
²⁹⁵²*predictions and uncertainty estimates for single top-quark production in*
²⁹⁵³*hadronic collisions*, *Comput. Phys. Commun.* **191** (2015) 74–89 (2015)
²⁹⁵⁴(cit. on p. 38).
- ²⁹⁵⁵⁶⁶M. Aliev et al.,
²⁹⁵⁶*HATHOR – HAdronic Top and Heavy quarks crOss section calculatoR*,
²⁹⁵⁷*Comput. Phys. Commun.* **182** (2011) 1034–1046 (2011) (cit. on p. 38).
- ²⁹⁵⁸⁶⁷J. A. Aguilar-Saavedra,
²⁹⁵⁹*Single top quark production at LHC with anomalous Wtb couplings*,
²⁹⁶⁰*Nucl. Phys. B* **804** (2008) 160–192 (2008) (cit. on p. 39).
- ²⁹⁶¹⁶⁸J. Butterworth et al., *PDF4LHC recommendations for LHC Run II*,
²⁹⁶²*J. Phys. G* **43** (2016) 023001 (2016) (cit. on pp. 40, 74).
- ²⁹⁶³⁶⁹A. D. Martin, W. J. Stirling, R. S. Thorne and G. Watt,
²⁹⁶⁴*Parton distributions for the LHC*, *Eur. Phys. J. C* **63** (2009) 189 (2009)
²⁹⁶⁵(cit. on pp. 40, 75).
- ²⁹⁶⁶⁷⁰A. D. Martin, W. J. Stirling, R. S. Thorne and G. Watt,
²⁹⁶⁷*Uncertainties on α_S in global PDF analyses and implications for*
²⁹⁶⁸*predicted hadronic cross sections*, *Eur. Phys. J. C* **64** (2009) 653–680
²⁹⁶⁹(2009) (cit. on p. 40).
- ²⁹⁷⁰⁷¹H.-L. Lai et al., *New parton distributions for collider physics*,
²⁹⁷¹*Phys. Rev. D* **82** (2010) 074024 (2010) (cit. on p. 40).
- ²⁹⁷²⁷²R. D. Ball et al., *Parton distributions with QED corrections*,
²⁹⁷³*Nucl. Phys. B* **877** (2013) 290–320 (2013) (cit. on p. 40).
- ²⁹⁷⁴⁷³M. Aaboud et al., *Measurement of the Higgs boson mass in the*
²⁹⁷⁵ *$H \rightarrow ZZ^* \rightarrow 4\ell$ and $H \rightarrow \gamma\gamma$ channels with $\sqrt{s} = 13$ TeV pp collisions*
²⁹⁷⁶*using the ATLAS detector*, *Phys. Lett. B* **784** (2018) 345–366 (2018)
²⁹⁷⁷(cit. on p. 45).
- ²⁹⁷⁸⁷⁴A. M. Sirunyan et al.,
²⁹⁷⁹*A measurement of the Higgs boson mass in the diphoton decay channel*,
²⁹⁸⁰*Phys. Lett. B* **805** (2020) 135425 (2020) (cit. on p. 45).
- ²⁹⁸¹⁷⁵F. Englert and R. Brout,
²⁹⁸²*Broken symmetry and the mass of gauge vector mesons*,
²⁹⁸³*Phys. Rev. Lett.* **13** (9 1964) 321–323 (1964) (cit. on p. 45).

- ⁷⁶P. W. Higgs, *Broken symmetries and the masses of gauge bosons*, Phys. Rev. Lett. **13** (16 1964) 508–509 (1964) (cit. on p. 45).
- ⁷⁷G. S. Guralnik, C. R. Hagen and T. W. B. Kibble, *Global conservation laws and massless particles*, Phys. Rev. Lett. **13** (20 1964) 585–587 (1964) (cit. on p. 45).
- ⁷⁸G. Aad et al., *Observation of a new particle in the search for the Standard Model Higgs boson with the ATLAS detector at the LHC*, Phys. Lett. B **716** (2012) 1–29 (2012) (cit. on pp. 45, 56).
- ⁷⁹S. Chatrchyan et al., *Observation of a New Boson at a Mass of 125 GeV with the CMS Experiment at the LHC*, Phys. Lett. B **716** (2012) 30–61 (2012) (cit. on pp. 45, 56).
- ⁸⁰T. Aaltonen et al., *Combined search for the standard model Higgs boson decaying to a bb pair using the full CDF data set*, Phys. Rev. Lett. **109** (2012) 111802 (2012) (cit. on p. 46).
- ⁸¹V. M. Abazov et al., *Combined Search for the Standard Model Higgs Boson Decaying to bb Using the D0 Run II Data Set*, Phys. Rev. Lett. **109** (2012) 121802 (2012) (cit. on p. 46).
- ⁸²D. de Florian et al., *Handbook of LHC Higgs Cross Sections: 4. Deciphering the Nature of the Higgs Sector*, **2/2017** (2016) (2016) (cit. on pp. 47, 48).
- ⁸³B. Mellado Garcia, P. Musella, M. Grazzini and R. Harlander, *CERN Report 4: Part I Standard Model Predictions*, (2016) (2016) (cit. on p. 48).
- ⁸⁴A. Pich, *Electroweak Symmetry Breaking and the Higgs Boson*, Acta Phys. Polon. B **47** (2016) 151, edited by M. Praszalowicz (2016) (cit. on p. 49).
- ⁸⁵M. Farina, C. Grojean, F. Maltoni, E. Salvioni and A. Thamm, *Lifting degeneracies in Higgs couplings using single top production in association with a Higgs boson*, JHEP **05** (2013) 022 (2013) (cit. on p. 50).
- ⁸⁶S. Biswas, E. Gabrielli and B. Mele, *Single top and Higgs associated production as a probe of the Htt coupling sign at the LHC*, JHEP **01** (2013) 088 (2013) (cit. on p. 50).
- ⁸⁷T. Appelquist and M. S. Chanowitz, *Unitarity Bound on the Scale of Fermion Mass Generation*, Phys. Rev. Lett. **59** (1987) 2405, [Erratum: Phys.Rev.Lett. 60, 1589 (1988)] (1987) (cit. on p. 50).
- ⁸⁸M. Aaboud et al., *Observation of Higgs boson production in association with a top quark pair at the LHC with the ATLAS detector*, Phys. Lett. B **784** (2018) 173–191 (2018) (cit. on p. 50).

- ⁸⁹K. Skovpen, ‘First observation of the $t\bar{t}H$ process at CMS’,
11th International Workshop on Top Quark Physics (2018)
(cit. on p. 50).
- ⁹⁰G. Aad et al.,
Search for $H \rightarrow \gamma\gamma$ produced in association with top quarks and constraints on the Yukawa coupling between the top quark and the Higgs boson using data taken at 7 TeV and 8 TeV with the ATLAS detector,
Phys. Lett. B **740** (2015) 222–242 (2015) (cit. on p. 51).
- ⁹¹V. Khachatryan et al., *Search for the associated production of the Higgs boson with a top-quark pair*,
JHEP **09** (2014) 087, [Erratum: *JHEP* 10, 106 (2014)] (2014)
(cit. on p. 51).
- ⁹²F. Demartin, F. Maltoni, K. Mawatari and M. Zaro,
Higgs production in association with a single top quark at the LHC,
Eur. Phys. J. C **75** (2015) 267 (2015) (cit. on pp. 51–53).
- ⁹³T. M. P. Tait and C. P. Yuan, *Single top quark production as a window to physics beyond the standard model*, *Phys. Rev. D* **63** (2000) 014018 (2000) (cit. on p. 53).
- ⁹⁴S. Biswas, E. Gabrielli, F. Margaroli and B. Mele,
Direct constraints on the top-Higgs coupling from the 8 TeV LHC data,
JHEP **07** (2013) 073 (2013) (cit. on p. 53).
- ⁹⁵CERN Web Page, *Our Member States*, (2022)
<https://home.web.cern.ch/about/who-we-are/our-governance/member-states> (visited on 11/01/2022) (cit. on p. 56).
- ⁹⁶T. Fazzini, G. Fidecaro, A. W. Merrison, H. Paul and A. V. Tollestrup,
Electron decay of the pion, *Phys. Rev. Lett.* **1** (7 1958) 247–249 (1958)
(cit. on p. 56).
- ⁹⁷F. J. Hasert et al., *Observation of Neutrino Like Interactions Without Muon Or Electron in the Gargamelle Neutrino Experiment*,
Phys. Lett. B **46** (1973) 138–140 (1973) (cit. on p. 56).
- ⁹⁸P. M. Watkins, *Discovery of the w and 2 bosons*,
Contemporary Physics **27** (1986) 291–324 (1986) (cit. on p. 56).
- ⁹⁹D. Decamp et al.,
Determination of the Number of Light Neutrino Species,
Phys. Lett. B **231** (1989) 519–529 (1989) (cit. on p. 56).
- ¹⁰⁰G. Baur et al., *Production of anti-hydrogen*,
Phys. Lett. B **368** (1996) 251–258 (1996) (cit. on p. 56).
- ¹⁰¹G. D. Barr et al.,
A New measurement of direct CP violation in the neutral kaon system,
Phys. Lett. B **317** (1993) 233–242 (1993) (cit. on p. 56).

- 3064 ¹⁰²V. Fanti et al., *A New measurement of direct CP violation in two pion*
3065 *decays of the neutral kaon*, Phys. Lett. B **465** (1999) 335–348 (1999)
3066 (cit. on p. 56).
- 3067 ¹⁰³R. Aaij et al., *Observation of J/ψ Resonances Consistent with*
3068 *Pentaquark States in $\Lambda_b^0 \rightarrow J/\psi K^- p$ Decays*,
3069 Phys. Rev. Lett. **115** (2015) 072001 (2015) (cit. on p. 56).
- 3070 ¹⁰⁴S. Maury, *The Antiproton Decelerator: AD*,
3071 Hyperfine Interact. **109** (1997) 43–52 (1997) (cit. on p. 56).
- 3072 ¹⁰⁵R. Alemany et al.,
3073 *Summary Report of Physics Beyond Colliders at CERN*,
3074 (2019), edited by J. Jaeckel, M. Lamont and C. Vallée (2019)
3075 (cit. on p. 56).
- 3076 ¹⁰⁶R. Catherall et al., *The ISOLDE facility*, J. Phys. G **44** (2017) 094002
3077 (2017) (cit. on p. 56).
- 3078 ¹⁰⁷E. Gschwendtner et al., *AWAKE, The Advanced Proton Driven Plasma*
3079 *Wakefield Acceleration Experiment at CERN*,
3080 Nucl. Instrum. Meth. A **829** (2016) 76–82, edited by U. Dorda et al.
3081 (2016) (cit. on p. 56).
- 3082 ¹⁰⁸M. Aguilar et al.,
3083 *The Alpha Magnetic Spectrometer (AMS) on the International Space*
3084 *Station. I: Results from the test flight on the space shuttle*, Phys. Rept.
3085 **366** (2002) 331–405, [Erratum: Phys.Rept. 380, 97–98 (2003)] (2002)
3086 (cit. on p. 57).
- 3087 ¹⁰⁹T. J. Berners-Lee and R. Cailliau,
3088 *WorldWideWeb: proposal for a HyperText Project*, tech. rep.,
3089 CERN, 1990 (cit. on p. 57).
- 3090 ¹¹⁰CERN Council holds special session on the Large Hadron Collider
3091 *project*, (1991) 3 p, Issued on 19 December 1991 (1991) (cit. on p. 57).
- 3092 ¹¹¹T. S. Pettersson and P Lefèvre,
3093 *The Large Hadron Collider: conceptual design*, tech. rep., 1995
3094 (cit. on pp. 57, 60).
- 3095 ¹¹²S. Myers,
3096 *The LEP Collider, from design to approval and commissioning*,
3097 John Adams' memorial lecture, Delivered at CERN, 26 Nov 1990
3098 (CERN, Geneva, 1991) (cit. on p. 57).
- 3099 ¹¹³B. Müller, J. Schukraft and B. Wysłouch,
3100 *First Results from Pb+Pb Collisions at the LHC*,
3101 Annual Review of Nuclear and Particle Science **62** (2012) 361–386
3102 (2012) (cit. on p. 59).

- 3103 ¹¹⁴CERN Web Page, *The Large Hadron Collider*, (2022)
3104 <https://home.cern/science/accelerators/large-hadron->
3105 *collider* (visited on 11/01/2022) (cit. on p. 59).
- 3106 ¹¹⁵R. Steerenberg et al., ‘Operation and performance of the cern large
3107 hadron collider during proton run 2’,
3108 *10th international particle accelerator conference* (2019) MOPMP031
3109 (cit. on p. 59).
- 3110 ¹¹⁶by Rende Steerenberg and A. Schaeffer, *LHC Report: The LHC is full!*,
3111 (*2018*) (2018) (cit. on p. 59).
- 3112 ¹¹⁷*8th International Conference on High-Energy Accelerators*,
3113 CERN (CERN, Geneva, 1971) (cit. on p. 59).
- 3114 ¹¹⁸*LHC Machine*,
3115 *JINST* **3** (2008) S08001, edited by L. Evans and P. Bryant (2008)
3116 (cit. on pp. 59, 62).
- 3117 ¹¹⁹*Radiofrequency cavities*, (*2012*) (2012) (cit. on p. 60).
- 3118 ¹²⁰K. Long et al., *Muon colliders to expand frontiers of particle physics*,
3119 *Nature Phys.* **17** (2021) 289–292 (2021) (cit. on p. 61).
- 3120 ¹²¹L Lari, H Gaillard and V Mertens,
3121 *Scheduling the installation of the LHC injection lines*, tech. rep.,
3122 CERN, 2004 (cit. on p. 62).
- 3123 ¹²²G. Aad et al.,
3124 *The ATLAS Experiment at the CERN Large Hadron Collider*,
3125 *JINST* **3** (2008) S08003 (2008) (cit. on pp. 62, 81, 85, 86, 90, 91).
- 3126 ¹²³S. Chatrchyan et al., *The CMS Experiment at the CERN LHC*,
3127 *JINST* **3** (2008) S08004 (2008) (cit. on p. 62).
- 3128 ¹²⁴A. A. Alves Jr. et al., *The LHCb Detector at the LHC*,
3129 *JINST* **3** (2008) S08005 (2008) (cit. on p. 63).
- 3130 ¹²⁵K. Aamodt et al., *The ALICE experiment at the CERN LHC*,
3131 *JINST* **3** (2008) S08002 (2008) (cit. on p. 63).
- 3132 ¹²⁶O. Adriani et al.,
3133 *The LHCf detector at the CERN Large Hadron Collider*,
3134 *JINST* **3** (2008) S08006 (2008) (cit. on p. 64).
- 3135 ¹²⁷O. Adriani et al.,
3136 *Technical design report of the LHCf experiment: Measurement of*
3137 *photons and neutral pions in the very forward region of LHC* (2006)
3138 (cit. on p. 64).
- 3139 ¹²⁸C. Alpigiani et al., *A Letter of Intent for MATHUSLA: A Dedicated*
3140 *Displaced Vertex Detector above ATLAS or CMS.*, (2018) (2018)
3141 (cit. on p. 65).

- 3142 ¹²⁹J. H. Yoo, *The milliQan Experiment: Search for milli-charged Particles*
3143 at the LHC, PoS ICHEP2018 (2018) 520. 4 p, proceeding for ICHEP
3144 2018 SEOUL, International Conference on High Energy Physics, 4-11
3145 July 2018, SEOUL, KOREA (2018) (cit. on p. 65).
- 3146 ¹³⁰A. Ball et al., *Search for millicharged particles in proton-proton*
3147 *collisions at $\sqrt{s} = 13$ TeV*, Phys. Rev. D **102** (2020) 032002 (2020)
3148 (cit. on p. 65).
- 3149 ¹³¹V. A. Mitsou, *The MoEDAL experiment at the LHC: status and results*,
3150 J. Phys. Conf. Ser. **873** (2017) 012010, edited by B. Grzadkowski,
3151 J. Kalinowski and M. Krawczyk (2017) (cit. on p. 65).
- 3152 ¹³²G. Anelli et al.,
3153 *The TOTEM experiment at the CERN Large Hadron Collider*,
3154 JINST **3** (2008) S08007 (2008) (cit. on p. 65).
- 3155 ¹³³A. Ariga et al., *Technical Proposal for FASER: ForwArd Search*
3156 *ExpeRiment at the LHC*, (2018) (2018) (cit. on p. 65).
- 3157 ¹³⁴A. Ariga et al.,
3158 *Letter of Intent for FASER: ForwArd Search ExpeRiment at the LHC*,
3159 (2018) (2018) (cit. on p. 65).
- 3160 ¹³⁵*LHC computing Grid. Technical design report*,
3161 (2005), edited by I. Bird et al. (2005) (cit. on p. 65).
- 3162 ¹³⁶WLCG Web Page, *Resources*, (2022)
3163 <https://wlcg-public.web.cern.ch/resources> (visited on
3164 31/01/2022) (cit. on p. 66).
- 3165 ¹³⁷*ATLAS computing: Technical design report*,
3166 (2005), edited by G. Duckeck et al. (2005) (cit. on p. 65).
- 3167 ¹³⁸WLCG Web Page, *Tier centres*, (2022)
3168 <https://wlcg-public.web.cern.ch/tier-centres> (visited on
3169 31/01/2022) (cit. on pp. 66, 67).
- 3170 ¹³⁹W. Herr and B Muratori, *Concept of luminosity*, (2006) (2006)
3171 (cit. on pp. 68, 69).
- 3172 ¹⁴⁰A. Hoecker, ‘Physics at the LHC Run-2 and Beyond’,
3173 2016 European School of High-Energy Physics (2016)
3174 (cit. on pp. 69, 70, 77).
- 3175 ¹⁴¹M. Aaboud et al., *Luminosity determination in pp collisions at $\sqrt{s} = 8$*
3176 *TeV using the ATLAS detector at the LHC*,
3177 Eur. Phys. J. C **76** (2016) 653 (2016) (cit. on p. 69).
- 3178 ¹⁴²G. Aad et al., *ATLAS data quality operations and performance for*
3179 *2015–2018 data-taking*, JINST **15** (2020) P04003 (2020) (cit. on p. 70).

- ³¹⁸⁰¹⁴³ *Luminosity determination in pp collisions at $\sqrt{s} = 13$ TeV using the*
³¹⁸¹ *ATLAS detector at the LHC*, tech. rep., CERN, 2019 (cit. on p. 70).
- ³¹⁸²¹⁴⁴ F. S. Cafagna, *Latest results for Proton-proton Cross Section*
³¹⁸³ *Measurements with the TOTEM experiment at LHC*,
³¹⁸⁴ PoS **ICRC2019** (2021) 207 (2021) (cit. on p. 73).
- ³¹⁸⁵¹⁴⁵ Particle Data Group Web Page,
³¹⁸⁶ *Data files and plots of cross-sections and related quantities for hadrons*,
³¹⁸⁷ (2022) <https://pdg.lbl.gov/2021/hadronic-xsections/> (visited on
³¹⁸⁸ 08/02/2022) (cit. on p. 74).
- ³¹⁸⁹¹⁴⁶ *Shrek*, 2001 (cit. on p. 79).
- ³¹⁹⁰¹⁴⁷ *CERN Council holds special session on the Large Hadron Collider*
³¹⁹¹ *project*, (1991) 3 p, Issued on 19 December 1991 (1991) (cit. on p. 77).
- ³¹⁹²¹⁴⁸ *ATLAS: technical proposal for a general-purpose pp experiment at the*
³¹⁹³ *Large Hadron Collider at CERN*, LHC technical proposal
³¹⁹⁴ (CERN, Geneva, 1994) (cit. on p. 78).
- ³¹⁹⁵¹⁴⁹ A. collaboration, ‘First 2.36 TeV Collision Events recorded by the
- ATLAS experiment, December 8th and 14th, 2009’, 2009 (cit. on p. 78).
- ³¹⁹⁷¹⁵⁰ G. Aad et al., *Measurements of the Higgs boson production and decay*
³¹⁹⁸ *rates and constraints on its couplings from a combined ATLAS and*
³¹⁹⁹ *CMS analysis of the LHC pp collision data at $\sqrt{s} = 7$ and 8 TeV*,
³²⁰⁰ JHEP **08** (2016) 045 (2016) (cit. on p. 78).
- ³²⁰¹¹⁵¹ G. Aad et al., *Measurement of the top quark-pair production cross*
³²⁰² *section with ATLAS in pp collisions at $\sqrt{s} = 7$ TeV*,
³²⁰³ Eur. Phys. J. C **71** (2011) 1577 (2011) (cit. on p. 78).
- ³²⁰⁴¹⁵² G. Aad et al., *Evidence for Electroweak Production of $W^\pm W^\pm jj$ in pp*
³²⁰⁵ *Collisions at $\sqrt{s} = 8$ TeV with the ATLAS Detector*,
³²⁰⁶ Phys. Rev. Lett. **113** (2014) 141803 (2014) (cit. on p. 78).
- ³²⁰⁷¹⁵³ M. Aaboud et al., *Evidence for light-by-light scattering in heavy-ion*
³²⁰⁸ *collisions with the ATLAS detector at the LHC*,
³²⁰⁹ Nature Phys. **13** (2017) 852–858 (2017) (cit. on p. 78).
- ³²¹⁰¹⁵⁴ M. Aaboud et al., *Search for the standard model Higgs boson produced*
³²¹¹ *in association with top quarks and decaying into a $b\bar{b}$ pair in pp*
³²¹² *collisions at $\sqrt{s} = 13$ TeV with the ATLAS detector*,
³²¹³ Phys. Rev. D **97** (2018) 072016 (2018) (cit. on p. 78).
- ³²¹⁴¹⁵⁵ M. Aaboud et al., *Observation of $H \rightarrow b\bar{b}$ decays and VH production*
³²¹⁵ *with the ATLAS detector*, Phys. Lett. B **786** (2018) 59–86 (2018)
³²¹⁶ (cit. on p. 78).
- ³²¹⁷¹⁵⁶ S. Amoroso, *Precision measurements at the LHC*, tech. rep.,
³²¹⁸ CERN, 2020 (cit. on p. 78).

- 3219 ¹⁵⁷H. Pacey, *EW SUSY Production at the LHC*, tech. rep., CERN, 2021
3220 (cit. on p. 78).
- 3221 ¹⁵⁸S. Das Bakshi, J. Chakrabortty, C. Englert, M. Spannowsky and
3222 P. Stylianou, *CP Violation at atlas in effective field theory*,
3223 *Phys. Rev. D* **103** (5 2021) 055008 (2021) (cit. on p. 78).
- 3224 ¹⁵⁹B. T. Carlson, *Dark Matter searches with the ATLAS detector*, (2020)
3225 (2020) (cit. on p. 80).
- 3226 ¹⁶⁰J. L. Pinfold, *ATLAS and astroparticle physics*, *Nucl. Phys. B Proc.*
3227 *Suppl.* **175-176** (2008) 25–32, edited by K. S. Cheng et al. (2008)
3228 (cit. on p. 80).
- 3229 ¹⁶¹N. D. Brett et al., *Discovery Reach for Black Hole Production*, (2009)
3230 (2009) (cit. on p. 80).
- 3231 ¹⁶²*ATLAS inner detector: Technical Design Report*, 1,
3232 Technical design report. ATLAS (CERN, Geneva, 1997) (cit. on p. 81).
- 3233 ¹⁶³G. Aad et al.,
3234 *The ATLAS Inner Detector commissioning and calibration*,
3235 *Eur. Phys. J. C* **70** (2010) 787–821 (2010) (cit. on p. 81).
- 3236 ¹⁶⁴M Capeans et al., *ATLAS Insertable B-Layer Technical Design Report*,
3237 tech. rep., 2010 (cit. on pp. 83, 84).
- 3238 ¹⁶⁵*Technical Design Report for the ATLAS Inner Tracker Pixel Detector*,
3239 tech. rep., CERN, 2017 (cit. on pp. 84, 86, 100).
- 3240 ¹⁶⁶ATLAS Experiment Web Page, *Detector and Technology*, (2022)
3241 <https://atlas.cern/discover/detector> (visited on 02/02/2022)
3242 (cit. on pp. 84, 87, 90, 94, 95).
- 3243 ¹⁶⁷F. Cavallari, *Performance of calorimeters at the LHC*,
3244 *Journal of Physics: Conference Series* **293** (2011) 012001 (2011)
3245 (cit. on pp. 86, 89, 90).
- 3246 ¹⁶⁸C. Grupen and B. Shwartz, ‘Calorimetry’, *Particle detectors*, 2nd ed.,
3247 Cambridge Monographs on Particle Physics, Nuclear Physics and
3248 Cosmology (Cambridge University Press, 2008) 230–272 (cit. on p. 88).
- 3249 ¹⁶⁹Particle Data Group Web Page, π^0 Decay Modes, (2022)
3250 <https://pdglive.lbl.gov/DataBlock.action?node=Q007TP> (visited
3251 on 02/02/2022) (cit. on p. 89).
- 3252 ¹⁷⁰A. Tarek Abouelfadl Mohamed, ‘The lhc and the atlas experiment’,
3253 *Measurement of higgs boson production cross sections in the diphoton*
3254 *channel: with the full atlas run-2 data and constraints on anomalous*
3255 *higgs boson interactions*
3256 (Springer International Publishing, Cham, 2020) 61 (cit. on pp. 90, 91).

- 3257 ¹⁷¹*ATLAS muon spectrometer: Technical design report*, (1997) (1997)
3258 (cit. on p. 91).
- 3259 ¹⁷²K. Ishii, *The ATLAS muon spectrometer*, PoS **HEP2001** (2001) 253,
3260 edited by D. o. Horváth, P. Lévai and A. Patkós (2001) (cit. on p. 92).
- 3261 ¹⁷³M Livan, *Monitored drift tubes in ATLAS*, tech. rep., CERN, 1996
3262 (cit. on p. 92).
- 3263 ¹⁷⁴G. Cattani, *The resistive plate chambers of the ATLAS experiment:*
3264 *performance studies*,
3265 *Journal of Physics: Conference Series* **280** (2011) 012001 (2011)
3266 (cit. on p. 93).
- 3267 ¹⁷⁵K. Nagai, *Thin gap chambers in ATLAS*, Nucl. Instrum. Meth. A **384**
3268 (1996) 219–221, edited by F. Ferroni and P. Schlein (1996)
3269 (cit. on p. 93).
- 3270 ¹⁷⁶*ATLAS magnet system: Technical Design Report*, 1,
3271 Technical design report. ATLAS (CERN, Geneva, 1997)
3272 (cit. on pp. 94, 95).
- 3273 ¹⁷⁷*ATLAS high-level trigger, data acquisition and controls: Technical*
3274 *design report*, (2003) (2003) (cit. on pp. 96, 97).
- 3275 ¹⁷⁸G. Aad et al., *Performance of the ATLAS Trigger System in 2010*,
3276 *Eur. Phys. J. C* **72** (2012) 1849 (2012) (cit. on p. 96).
- 3277 ¹⁷⁹*Technical Design Report for the Phase-II Upgrade of the ATLAS TDAQ*
3278 *System*, tech. rep., CERN, 2017 (cit. on p. 101).
- 3279 ¹⁸⁰G. Aad et al., *The ATLAS Simulation Infrastructure*,
3280 *Eur. Phys. J. C* **70** (2010) 823–874 (2010) (cit. on p. 103).
- 3281 ¹⁸¹P. Mato, *GAUDI-Architecture design document*, (1998) (1998)
3282 (cit. on p. 106).

³²⁸³ **Summary of the results**

3284 **Recerca de la producció
3285 associada de bosó de Higgs i
3286 un quark top amb dos leptons i
3287 tau hadrònic a l'estat final**

3288 **1 Marc teòric**

3289 **1.1 El Model Estàndard**

3290 Maybe, I could translate this for the SM summary:
3291 <https://www.quantamagazine.org/a-new-map-of-the-standard-model->
3292 [of-particle-physics-20201022/](https://www.quantamagazine.org/a-new-map-of-the-standard-model-of-particle-physics-20201022/)

3293 **1.2 La física del quark top**

3294 **1.3 La física del bosó de Higgs**

3295 **2 L'experiment ATLAS del LHC al CERN**

3296 **2.1 El gran col·lisionador d'hadrons**

3297 **2.2 El detector ATLAS**

3298 **3 Mesura de la polarització del quark top al
3299 canal-*t***

3300 Mesura d'observables sensibles a la polarització del quark top

3301 **3.1 Selecció d'esdeveniments**

3302 **3.2 Estimació del fons**

3303 **3.3 Fonts d'incertesa**

3304 **3.4 Resultats**

3305 **4 Recerca de processos tH amb un estat final $2\ell + 1\tau_{\text{had}}$**

3307 **4.1 Selecció d'esdeveniments**

3308 **4.2 Estimació del fons**

3309 **4.3 Fonts d'incertesa**

3310 **4.4 Resultats**

3311 **5 Conclusions**

3313 Contraportada

3314 The discovery of a Higgs boson by the ATLAS and CMS experiments
3315 in 2012 opened a new field for exploration in the realm of particle physics.
3316 In order to better understand the Standard Model (SM) of particle physics,
3317 it is imperative to study the Yukawa coupling between this new particle
3318 and the rest of the SM components. Among these, of prominent interest is
3319 the coupling of the Higgs boson to the top quark (y_t), which is the most
3320 massive fundamental particle and, consequently, the one with the strongest
3321 coupling to the Higgs

3322 The direct measurement of y_t is only possible at LHC via two associated
3323 Higgs productions; with a pair of top quarks ($t\bar{t}H$) and with single-top
3324 quark (tHq). While the $t\bar{t}H$ permits a model-independent determination of
3325 the magnitude of y_t , the only way of directly measuring its sign is through
3326 the tHq production. This is due to the fact that the two leading-order
3327 Feynman diagrams for tHq production interfere with each other depending
3328 on y_t sign. Current experimental constraints on y_t favour the SM predictions,
3329 even though an opposite sign with respect to the SM expectations is not
3330 completely excluded yet.

3331 In this work it is presented a search for the production of a Higgs boson in
3332 association with a single-top quark in a final state with two light-floavoured-
3333 charged leptons and one hadronically decaying tau lepton (named $2\ell + 1\tau_{\text{had}}$
3334 channel). This analysis uses an integrated luminosity of 139 fb^{-1} of proton-
3335 proton collision data at centre-of-mass energy of 13 TeV collected by ATLAS
3336 during LHC Run 2.

3337 This search is exceptionally challenging due to the extremely small cross
3338 section of the tHq process (70 fb^{-1}) in general and, more particularly, the
3339 the $2\ell + 1\tau_{\text{had}}$ final-state channel, which only accounts for a 3.5% of the
3340 total tHq production.

3341 Because of this, the separation of the tHq signal events from back-
3342 ground events is done by means of machine-learning (ML) techniques using
3343 boosted-decision trees (BDT) to define both signal and control regions. The
3344 most most relevant background processes are those related to top-pairs pro-

duction (such as $t\bar{t}$, $t\bar{t}H$, $t\bar{t}Z$ and $t\bar{t}W$), Z -boson plus jets and single-top processes.

Significant suppression of the background events with jets wrongly selected as leptons is achieved by demanding electrons and muons to pass strict isolation requirements. Simultaneously, hadronic-tau leptons are demanded to pass the requirement of the recurrent-neural-network-based discriminator to reduce misidentifications from jets.

The reconstruction of the events is also enhanced by similar ML methods since in the scenario in which the light-flavour leptons have the same sign, in principle, it is not possible to determine which lepton is originated from the Higgs boson and which from the top quark.

The possible observation of an excess of signal events with respect to the SM predictions, would be a clear evidence of new physics in terms of \mathcal{CP} -violating y_t coupling.

Additionally, the contribution to the single-top-quark polarisation first measurement is presented as well. In this other analysis the components of the full polarisation vector of the top quark are measured taking advantage of the peculiarities of the single-top-quark decay. Benefitting from the fact that the top quark lifetime is smaller than the depolarisation timescale, the decay products preserve the spin information of the top quark. Via angular distributions, it is measured in the top-quark rest frame.